

Exploiting Speckle to Image Deeper in Scattering Media

Thesis by
Eunice Michelle Chua Cua

In Partial Fulfillment of the Requirements for the
Degree of
Doctor of Philosophy

The logo for the California Institute of Technology (Caltech), featuring the word "Caltech" in a bold, orange, sans-serif font.

CALIFORNIA INSTITUTE OF TECHNOLOGY
Pasadena, California

2022
Defended June 17th, 2021

© 2022

Eunice Michelle Chua Cua
ORCID: 0000-0002-0394-757X

All rights reserved except where otherwise noted

ACKNOWLEDGEMENTS

I would not have been able to complete my PhD were it not for the numerous people who supported and assisted me along this journey. I am grateful to the following people:

To my advisor, Prof. Changhuei Yang, who saw potential in me and continually challenged me, which helped me grow and hopefully become a better researcher.

To my committee members, Prof. Lihong Wang, Prof. Azita Emami, and Prof. Yu-Chong Tai, for providing helpful suggestions and critiques, and for encouraging me to focus on the fundamentals while thinking more broadly.

To the members of the Biophotonics lab, both past and present. To Dr. Edward (Haojiang) Zhou, who mentored me, taught me how to build a DOPC setup, and provided many tips for how to more precisely align optical systems. To Dr. Hoawen Ruan, Daniel Martin, and Dr. Baptiste Blochet, for their technical assistance, support, and friendship. To Anne Sullivan – you are simply amazing. Thank you for keeping lab operations smooth and watching out and caring for us lab members. To Dr. Joshua Brake, Dr. Albert (Jaebum) Chung, Dr. Jian Xu, Ruizhi Cao, Cheng Shen, Dr. Antony Chan, for fruitful conversations.

To the Caltech staff, in particular Christine Garske, Ms. Tanya Owens, and Dr. Kate McAnulty, for their support and assistance, and for always lending an understanding ear and giving sound advice. To Dr. Erin Burkett at the Hixon Writing Center, for providing helpful tips and feedback for improving my writing. To Dr. Robyn Javier, for helping me improve my presentation. To Dr. Andres Collazo, for helping with optics and mounting biological samples. And to Ms. Liz Alaya and Prof. Justin Bois, who went above and beyond to provide support and assistance during my PhD.

To the members of the Caltech pickup volleyball group, Caltech ping pong club, the squash group, Two guys and a Canadian, and Yangji for the fun times, after-hours drinks, and good food. After a tough day at work, I could look forward to relaxing and de-stressing over sports and camaraderie.

To Prof. Marinko Sarunic, without whom I would not have discovered the joy in doing research. Your guidance and mentorship were invaluable in making me a better researcher and setting me on this path.

To the residents of 216 S. Chester and our COVID bubble – Cai Tong Ng, Emile

Oshima, Ubamanyu Kanthasamy, Conor Martin, and Keree McGuire – for keeping me sane and putting up with me during the last few years of my PhD and during COVID, and providing a home filled with laughter, support, food, exercise, bubble tea, and fun.

To my church family at Missio and ECBC, in particular Dr. Vivian Lam, Holly Swyers and the rest of the the Swyers clan, Ken and Liz Jenkins, Anna and Kurt Mar, and Dr. Bekah Silva, for their support and friendship, and for providing perspective, advice, cuteness, and good food when times got rough.

To my family, for supporting me in all that I do.

And lastly, to Kai Matsuka, for his constant support, encouragement, and never-ending optimism, which helped me stay sane and push on. I greatly benefited from his strength in math and cooking.

ABSTRACT

Optical methods for imaging and focusing are advantageous in many scenarios as optics can provide exquisite spatial resolution, has multiple sources of contrast, and does not impart ionizing radiation. However, optical scattering remains a fundamental challenge which limits the depth at which we can perform imaging with good spatial resolution. This challenge motivated our investigations into methods that could make use of the scattered light in order to extend the depth of imaging through or within scattering media. In particular, we focus on answering: (1) Can one ‘unscramble’ the scattered light in order to recover information about the otherwise hidden object?; and (2) Can we preferentially detect the more forward scattered photons in an efficient manner in order to allow deeper penetration with modest resolution? These two questions are explored in the first two projects of the thesis:

1. The development of an imaging system that detects the scattered light and exploits correlations within the scattering process to enable imaging through scattering media at diffraction-limited resolution.
2. The introduction of a novel method, termed Speckle-Resolved Optical Coherence Tomography, that sensitively and preferentially detects the more forward scattered photons in a coherent, speckle-resolved fashion to allow deeper imaging at moderate resolution.

Optical methods offer the benefit of visualizing samples that would otherwise appear transparent. Using light, one is able to visualize and measure the thickness of transparent films and coatings in a non-contact manner. The third project in my thesis focuses on using light to non-destructively visualize and characterize the evenness of the silicone oil layer that typically coats the inner surface of prefilled syringes. Characterizing the evenness of this silicone oil layer is important as it impacts the functionality of the prefilled syringe and may correlate with particle formation, which is undesirable as the number of particles in a syringe is regulated due to potential health concerns.

PUBLISHED CONTENT AND CONTRIBUTIONS

- **M. Cua**, B. Blochet, and C. Yang, "Speckle-Resolved Optical Coherence Tomography for Mesoscopic Imaging within Scattering Media," *In Preparation*
M.C. participated in conceiving the project and designed and constructed the optical system, experiments, and samples; analyzed the data; and wrote the manuscript.
- **M. Cua**[†], D. Martin[†], P. Meza, G. Toracca, T. Pearson, S. Cao, and C. Yang, "Method to determine syringe layer heterogeneity and investigation of its impact on product particle counts," *Optics Letters* 109(11):3292-3299 (2020) DOI: 10.1016/j.xphs.2020.07.012
M.C. participated in conceiving the project, designing and constructing the optical system and image processing pipeline, analyzing the data, drawing figures, and writing the manuscript.
- J. Xu, R. Cao, **M. Cua**, and C. Yang, "Single-shot surface 3D imaging by optical coherence factor," *Optics Letters* 45(7):1734-1737 (2020) DOI: 10.1364/OL.384551
M.C. helped with experiments and revising the figures and the manuscript.
- Y. Huang, **M. Cua**, J. Brake, Y. Liu, and C. Yang, "Investigating ultrasound-light interaction in scattering media," *Journal of Biomedical Optics* 25(2): 025002 (2020) DOI: 10.1117/1.JBO.25.2.025002
M.C. participated in designing and performing the simulation, designing and building the optical setup, and revising the figures and manuscript.
- J. Xu, **M. Cua**, E. Zhou, Y. Horie, A. Faraon, and C. Yang, "Wide-angular-range and high-resolution beam steering by a metasurface-coupled phased array," *Optics Letters* 43(21):5255-5258 (2018) DOI: 10.1364/OL.43.005255
M.C. participated in providing conceptual support and revising the figures and manuscript.
- **M. Cua**, E. Zhou, and C. Yang, "Imaging moving targets through scattering media," *Optics Express* 25(4): 3935-3945 (2017) DOI: 10.1364/OE.25.003935

M.C. designed and built the optical setup and experiments, performed the experiments, analyzed the data, and wrote the manuscript with help from E.Z.

Note: † denotes first co-authorship.

TABLE OF CONTENTS

Acknowledgements	iii
Abstract	v
Published Content and Contributions	vi
Table of Contents	vii
List of Illustrations	x
List of Tables	xii
Chapter I: Introduction	1
1.1 The Problem with Scattering	2
1.2 Methods to Deal with Scattering	4
1.3 Goals of this Thesis	13
1.4 Thesis Outline	16
Bibliography	17
Chapter II: Background Information	21
2.1 Light-Tissue Interactions	21
2.2 Absorption	23
2.3 Scattering	23
2.4 Speckle	30
2.5 Coherence	38
2.6 Interferometry	40
Bibliography	48
Chapter III: Imaging Moving Targets Through Scattering Media	50
3.1 Introduction	50
3.2 Principle	51
3.3 Results	57
3.4 Discussion	62
3.5 Conclusion	63
Bibliography	66
Chapter IV: Speckle-Resolved Optical Coherence Tomography	69
4.1 Introduction	70
4.2 Simulation	71
4.3 Experimental Results	74
4.4 Discussion	86
4.5 Conclusion	88
Bibliography	94
Chapter V: Method to Determine Syringe Silicone Oil Layer Heterogeneity and Investigation of its Impact on Product Particle Counts	96
5.1 Introduction	96
5.2 Materials and Methods	98
5.3 Results	103

5.4 Discussion 108
5.5 Conclusion 111
Bibliography 112

LIST OF ILLUSTRATIONS

<i>Number</i>	<i>Page</i>
1.1	2
1.2	3
1.3	3
1.4	4
1.5	5
1.6	6
1.7	8
1.8	9
1.9	10
1.10	11
1.11	12
1.12	13
1.13	13
1.14	14
2.1	22
2.2	26
2.3	28
2.4	29
2.5	31
2.6	33
2.7	34
2.8	35
2.9	36
2.10	37
2.11	39
2.12	41

2.13	Two common interferometers include Michelson interferometers and Mach-Zender interferometers.	41
2.14	Thin-film interference.	42
2.15	Schematic of phase-shifting and off-axis holography systems.	44
3.1	Principle behind non-invasive imaging of obscured moving objects.	52
3.2	Impact of object travel distance on the computed speckle autocorrelation (SAC).	55
3.3	Experimental setup for imaging hidden moving objects.	58
3.4	Experimental demonstration of imaging moving targets	59
3.5	Experimental results showing the impact of object travel distance on the speckle autocorrelation (SAC) and object reconstruction.	60
3.6	Experimental demonstration of imaging moving targets hidden within a scattering object.	61
4.1	Concept of Speckle-Resolved OCT (srOCT).	72
4.2	Impact of restricting spatial and angular range on improving resolution.	73
4.3	Principle of Speckle-Resolved OCT (srOCT).	75
4.4	Experimental setup for Speckle-Resolved OCT.	76
4.5	srOCT imaging through a scattering phantom.	79
4.6	Lateral and axial resolution of srOCT.	80
4.7	SNR advantage of speckle resolution	84
4.8	srOCT imaging through biological sample	85
4.9	Comparison of the exit position and the exit angle for different classes of photons.	90
4.10	Determination of speckle size constraint to prevent aliasing in off-axis holography	91
5.1	Overview of the multi-color interferometric imaging system	99
5.2	Automatic detection of dark spots in an interferogram	101
5.3	Impact of imaging at a lower percentage coverage	104
5.4	Comparison of manual and automatic spot counting.	104
5.5	Spatial distribution of heterogeneity	105
5.6	Comparison of particle counts in PFS-F and PFS-D syringes.	106
5.7	Sample interferograms from a PFS-F and PFS-D syringe.	106
5.8	Comparison of silicone oil distribution heterogeneity in PFS-F and PFS-D syringes.	107

LIST OF TABLES

<i>Number</i>	<i>Page</i>
5.1 Correlation results investigating association between cumulative particle counts and heterogeneity measures.	108

Chapter 1

INTRODUCTION

Optics and optical imaging, which involve the study of the behavior and manipulation of light, have been invaluable in helping us interact and understand the world around us. Optics is used in a wide range of engineering applications. For example, the optical microscope has helped us understand the microscopic world, while the telescope has helped us study the solar system and the origins of our universe. Aside from imaging, optics has been advantageous in applications such as fiber optics communication and remote sensing. Optics has found wide applicability in part due to its high spatial resolution, sensitivity to material composition, and complex nature.

Firstly, the exquisite spatial resolution enables us to focus on or manipulate objects with high spatial selectivity. The conventional limit of spatial resolution is given by the so-called ‘diffraction limit,’ which is half the wavelength. Since the wavelength of optical light spans from 400 nm to 1000 nm, optical imaging is able to resolve objects down to hundreds of nanometers. This is sufficient to visualize bacteria, cells, and even specific cellular components. A process called two-photon polymerization has also enabled 3D printing of nanoscale features and nano-architected metals using light 200 nm [1, 2]. This high spatial resolution has been instrumental in using light to understand and shape our world.

Secondly, the energy of optical wavelengths is well-matched to interact with molecules and atoms. This energy matching provides the basis for many sources of contrast and facilitates using light to probe for biochemical information. For example, in astronomy, spectroscopy is used to determine the properties and temperature of stars and planets [3]. The absorption of light also requires this energy matching. Absorption is a necessary component of fluorescence imaging, which involves staining or dyeing specific components for enhanced visualization. H&E staining highlights the cell nuclei, cytoplasm, and extracellular matrix, and is the standard in pathology for diagnosing diseases [4]. Absorption is also involved in myriad applications such as detecting our heart beat and blood oxygenation levels, ablating tissue in laser surgery, exciting neurons to control behavior, and performing cardiac pacemaking [5–7].

Thirdly, light has an amplitude and phase. Probing the phase of light can provide additional information and sources of contrast. Phase imaging methods are able to visualize otherwise transparent objects as the phase of light is sensitive to differences in the speed of light as it travels through different mediums. Using the phase of light, small displacements and surface topology can be measured up to picometer distances or even smaller.

Although optical imaging has many advantages, there are also challenges. Optical imaging works well in thin or transparent media, where non-scattered or singly-backscattered light is dominant. This non-scattered or singly-backscattered light is also often referred to as ‘ballistic’ light (Fig. 1.1) and is traditionally thought of as the component that retains the best resolution. Many imaging methods are dependent on controlling or detecting this ballistic light component. However, in scattering media, the scattered light can overwhelm the ballistic component and the various imaging methods may start to fail.

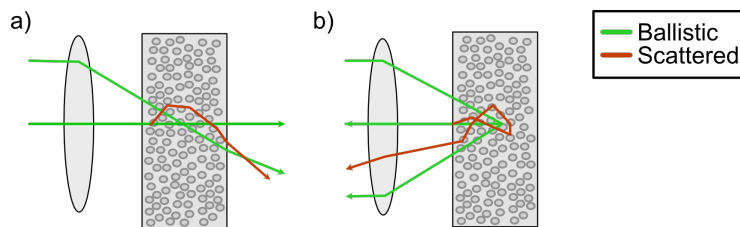


Figure 1.1: **Examples of ballistic light.** Ballistic light includes a) non-scattered light, for transmitted light, and b) singly-backscattered light, for back-reflected light.

The main focus of my thesis is extending the boundaries of performing optical imaging in scattering media. Two of the projects presented in this thesis explore methods to overcome or harness scattering. The third project introduces an imaging method for assessing the quality of syringe siliconization. For this reason, I will spend most of this chapter discussing the problem that scattering poses and some of the current methods of dealing with scattering. I will end this chapter with a discussion of the goals of this thesis and provide an outline for the remaining chapters in this thesis.

1.1 The Problem with Scattering

Scattering describes the deflection of light by small particles suspended in a medium with a different refractive index. In fog, the presence of small water particles and dust suspended in the air causes optical scattering, which limits our ability to see in

the distance. In tissue imaging, various cellular components and tissue types have different refractive indices and cause optical scattering.

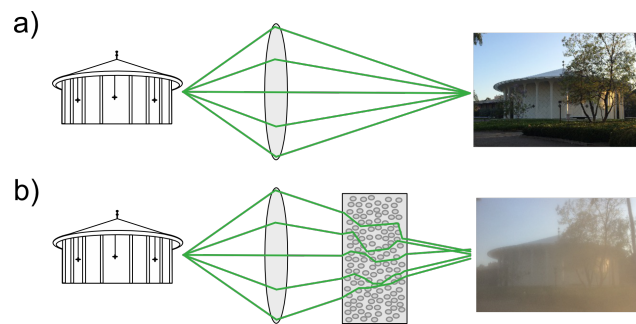


Figure 1.2: Scattering impedes the formation of a focus and degrades image quality.

Although scattering is a source of contrast in optical imaging, it can also act as a barrier. The scattered light may start to overwhelm the ballistic signal, which impedes the formation of a focus and causes a degradation in image quality or light delivery (Fig. 1.2). While the total light power is conserved in scattering, the power of the ballistic light component decreases exponentially with depth. Since the ballistic component contains the most direct information of the object, scattering poses a challenge that increases with depth (Fig. 1.3). In biological tissue, scattering is dominant and limits many microscopy techniques to only imaging the superficial tissue layers. In methods such as optogenetics and laser surgery, the exponential reduction in intensity with depth makes it difficult to deliver light deep into tissue. Therefore, considerable attention has been placed in devising ways to reduce, mitigate, or otherwise deal with optical scattering.

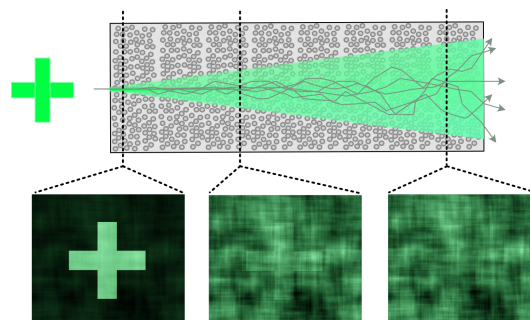


Figure 1.3: The impact of scattering increases with depth.

1.2 Methods to Deal with Scattering

There are many methods to reduce or deal with optical scattering. Since scattering is due to refractive index inhomogeneities in the medium, methods that reduce this refractive index mismatch reduce scattering. One such method is optical clearing, which reduces the refractive index mismatch by removing water and/or lipids from tissue and replacing the surrounding medium with a refractive-index-matching solution [8–11]. However, optical clearing modifies the sample and may not be feasible in all applications. Another method of reducing scattering is to increase the wavelength of light used for imaging, since particles much smaller than the wavelength tend to scatter light more strongly. More generally, a plethora of optical techniques have been developed to deal with scattering. These methods can be loosely categorized into two groups: (1) ballistic imaging methods that aim to only detect the non-scattered or singly-backscattered light components, and (2) scattered light imaging methods that detect and make use of the scattered light. In this section, we will briefly cover some of the various methods of dealing with scattered light.

Ballistic Imaging Methods

Ballistic imaging methods aim to reject the diffusely scattered light and only detect the ballistic component. These ballistic photons are what classically permits high-resolution imaging. In this section, we will cover various ‘gating’ techniques that ‘gate out’ the unwanted diffuse light component. We will also discuss the limitations of ballistic imaging methods, which forms the motivation for developing imaging methods that make use of the scattered light component.

Confocal and Angular Gating

Confocal and angular gating leverage the fact that the ballistic photons follow well-defined and predictable trajectories. Therefore, a spatial or angular filter can be used to reject photons that travel an altered pathway. Fig. 1.4 presents an example of confocal and angular gating.

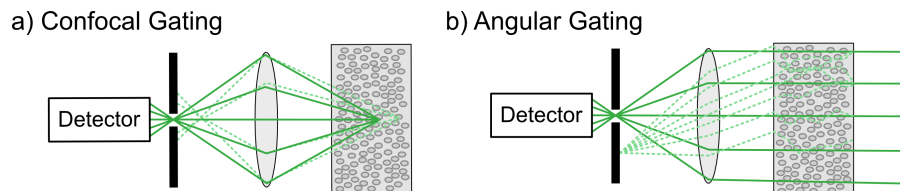


Figure 1.4: Confocal and angular gating reject non-ballistic light.

In confocal gating, only light stemming from the specific focus spot is accepted; contributions from scattered light or light from other focal planes is rejected. One method of achieving this is to use a confocal pinhole (Fig. 1.4a) as is done in confocal microscopy. It is called ‘confocal’ as both the illumination and detection are focused at the same point. Confocal microscopy is able to provide high-resolution, 3D imaging of a sample at deeper depths than conventional wide-field microscopy, which detects more of the back-scattered light and does not limit detection to only a single focal plane.

Multiphoton microscopy is another imaging method that utilizes longer wavelengths and confocal gating in order to reject scattered light [12]. In multi-photon microscopy, multiple photons must interact in order to excite the sample and generate fluorescence signal. Only light at the focus spot can appreciably generate fluorescence. Although the detected fluorescence has a shorter wavelength than the incident light and experiences more scattering, the fluorescence light all stems from the same location – the excitation focal spot. Therefore, the excitation acts as a virtual confocal gating that localizes the signal to a single spot in the sample.

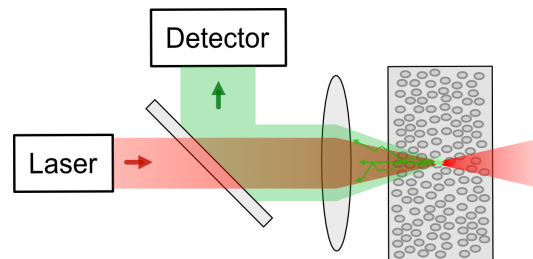


Figure 1.5: **Virtual pinhole in multiphoton microscopy.** Multiphoton microscopy restricts detected fluorescence signal to those coming from the focus of the excitation beam, which acts as a ‘virtual’ confocal pinhole.

In contrast to confocal gating, which restricts photons based on their position, angular gating restricts photons based on their orientation and rejects photons whose orientations have been perturbed [13, 14]. For example, in Fourier Space gating, a collimated beam is incident on the scattering media, and a physical pinhole at the output of a lens is used to reject all angles but the incident angle (Fig. 1.4b). The lateral position of the pinhole determines the angle that will be accepted. Angular gating requires the incident light to travel in a single direction and leverages the fact that the orientation of ballistic light is predictable.

Time and Coherence Gating

Another method to distinguish ballistic photons is by their time-of-flight in scattering media. When light propagates in scattering media, the ballistic photons travel shorter distances than the scattered light and will therefore exit the tissue earlier [15] (Fig. 1.6). The scattered light can be loosely separated into 2 categories: ‘snake’ photons, which are more predominantly forward scattered; and ‘diffuse’ photons, which are more strongly scattered. Time-gating methods are able to reject the diffuse photons by detecting only the early-arriving photons.

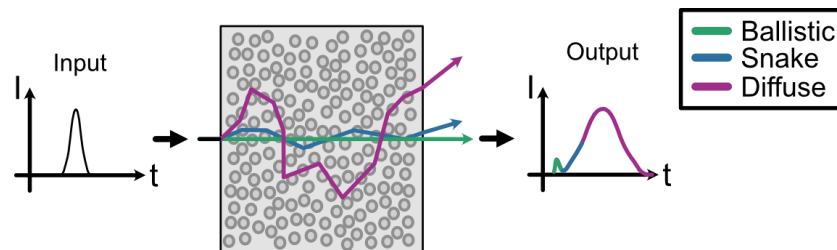


Figure 1.6: **Comparison of time-of-flight between ballistic and scattered light.** Ballistic photons travel the shortest distance in scattering media and exit the tissue the earlier compared to the scattered light.

Time gating employs a pulsed laser source and a fast switch to block out light that travels longer distances [13, 15–18]. The response times of the switches are on the order of $1 \text{ ps} = 10^{-12} \text{ s}$ [19]. Within this time frame, light can travel approximately $300 \mu\text{m}$. For a 1 mm -thick scattering medium, this means that only light that travelled more than 30% longer than the ballistic light, which travels 1 mm , will be rejected. Thus, the response time imposes a limitation to the degree by which scattered light can be rejected.

Coherence gating is a method that can distinguish photon time-of-flights with finer resolution than time gating [20, 21]. In coherence gating, only photons whose travel distances match that of a reference pathlength is detected and considered signal. In contrast to time gating, coherence gating depends on the coherence of the light source. One important parameter is the coherence length; this parameter defines the resolution at which one can distinguish travel distances. Low-coherence light sources can have coherence lengths on the order of $1 \mu\text{m}$ and are therefore able to separate photons based on a time-of-flight difference of $3 \text{ fs} = 3 \times 10^{-15} \text{ s}$.

Optical Coherence Tomography (OCT) is an imaging modality that combines both coherence and confocal gating to sensitively detect the back-scattered ballistic light

from the sample [22]. It can be considered an optical analogue of ultrasound in that it provides high-resolution cross-sectional images and 3D volumes of samples. OCT is commonly used by optometrists to image the various layers of the retina, which is helpful for visualizing the health of the retina and diagnosing diseases [23]. One advantage of OCT is that it is extremely sensitive to small back-reflections from the sample. As a rule-of-thumb, OCT is able to detect structures that reflect as little as 1 in 10^{11} to 10^{12} photons! This sensitivity makes OCT an attractive ballistic imaging method.

Limitation in Ballistic Imaging Methods

Ballistic imaging methods rely on the detection of ballistic photons to perform high-resolution imaging. In scattering media, however, the intensity of the ballistic light decreases exponentially with depth. This imposes a limitation on the depth at which these techniques can be reliably used. In the case of confocal microscopy, this depth limitation is typically a few hundred microns in tissue. In the case of OCT, which is able to sensitively detect sample reflectivities on the order of 10^{-11} to 10^{-12} , the depth limitation is still often on the order of 1 mm. This depth limit will be referred to as the ballistic limit in this chapter.

Scattered Light Imaging Methods

Although scattering is often considered a source of noise, if one is able to make sense of the scattering, then the scattered light can be leveraged to permit imaging deeper in tissue. This approach is attractive as the scattered light does not decay exponentially with depth, unlike the ballistic component. In this section, we discuss some existing methods that exploit scattered light to image or focus deeper in scattering media.

Optical Tomography

Optical tomography methods detect the scattered light and use computational methods to reconstruct the sample information. Here, I will cover two methods of optical tomography, namely Laminar Optical Tomography (LOT) and Diffuse Optical Tomography (DOT). These methods are not implemented in my thesis; they are included here for thoroughness.

Laminar Optical Tomography (LOT) is a method that detects both the ballistic and multiply-scattered light in order to perform depth-resolved imaging past the ballistic limit [24, 25]. In LOT, the incident light is scanned across the sample and the back-scattered light is detected at various distances from the incident light position

(Fig. 1.7). Since light that is detected further also tends to have travelled deeper, LOT can use the light detected at different distances to extract both lateral and depth information.

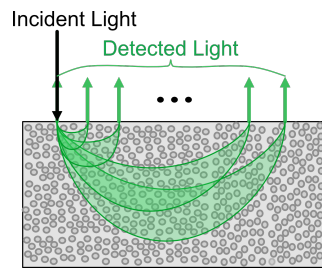


Figure 1.7: **Illumination and detection scheme for Laminar Optical Tomography (LOT).** In LOT, the scattered light is detected at multiple distances away from the incident light position.

Similarly, Diffuse Optical Tomography (DOT) systems also detect the scattered light from the object. However, in DOT, the back-scattered light from the sample is detected at various spatial locations throughout the sample [26, 27]. For example, for brain or breast imaging, it is not uncommon for sources and detectors to be placed along the entire circumference of the sample. In contrast to LOT, these systems are typically employed for larger depths, typically on the order of centimeters in tissue. At these depths, light is considered to be fully randomized, and the transport of light in tissue can be modeled using the diffusion approximation. The diffusion approximation assumes that the scattering process diffuses energy in all directions equally, and that absorption is dominated by scattering [19].

In order to make sense of the scattered light measurements in LOT and DOT, simulation and modelling methods such as Monte Carlo or the diffuse approximation (for DOT) are used to determine the sensitivity of the measurements to perturbations in the local scattering or absorption properties of the sample. These sensitivity functions are then used to iteratively undo the scattering and determine the target information [24, 28]. Through this process, LOT is capable of imaging to depths of > 2 mm in tissue and at resolutions on the order of 100-200 μm , and DOT is capable of imaging centimeters into tissue with resolutions on the order of 20% of the imaging depth [19].

Due to this reliance on simulation or modelling, LOT and DOT often assume that the scattering properties of the sample are homogeneous. They also require prior knowledge about the optical properties and geometry of the sample in order to

accurately model light transmission and computationally reconstruct the desired sample information.

Wavefront Shaping

LOT and DOT both detect the scattered light and computationally invert the scattering process to retrieve information about the sample. In contrast, Wavefront Shaping (WFS) methods aim to manipulate the behavior of the scattered light [29–31]. Although the scattering process appears to be random, it is in fact deterministic: for a static scattering media, a given input wavefront will scatter in the same manner and result in the same output wavefront. The goal of WFS techniques is to find the shape of the incident wavefront that causes the scattered light to create the desired target, such as a focused spot deep inside scattering media.

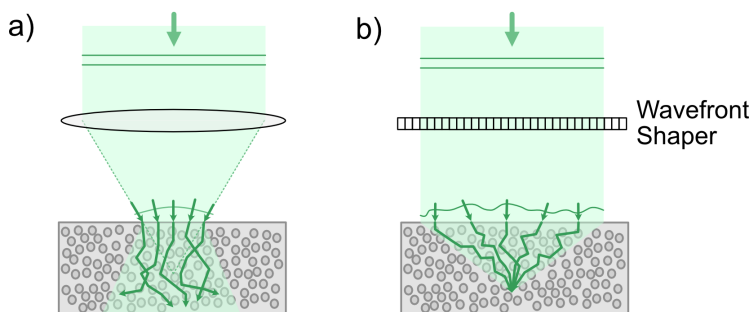


Figure 1.8: **Concept of wavefront shaping (WFS).** The goal of WFS is to shape the incident wavefront and control the scattered light behavior.

Three general classes of methods to achieve WFS have been shown in Fig. 1.9: Transmission Matrix (TM) approaches, Optical Phase Conjugation (OPC), and Feedback-based Wavefront Shaping (f-WFS).

A transmission matrix T_{ab} is a linear function that provides a relationship between a discretized input wavefront E_a and output wavefront (E_b). That is, $E_b = T_{ab}E_a = f(E_a)$. Here, I will only briefly mention transmission matrices; please refer to Section 2.4 for a more detailed discussion.

Knowledge of the transmission matrix provides the ability to manipulate the scattering process to yield any desired output wavefront $E_{b,out}$ by tailoring the incident light wavefront $E_{a,in}$ appropriately [32–34]. If $E_{a,in} = f^{-1}(E_{b,target})$, then

$$E_{b,out} = f(E_{a,in}) = f\left(f^{-1}(E_{b,target})\right) = E_{b,target}. \quad (1.1)$$

However, measurement of the transmission matrix can be a time-intensive process that requires access to both sides of the scattering media.

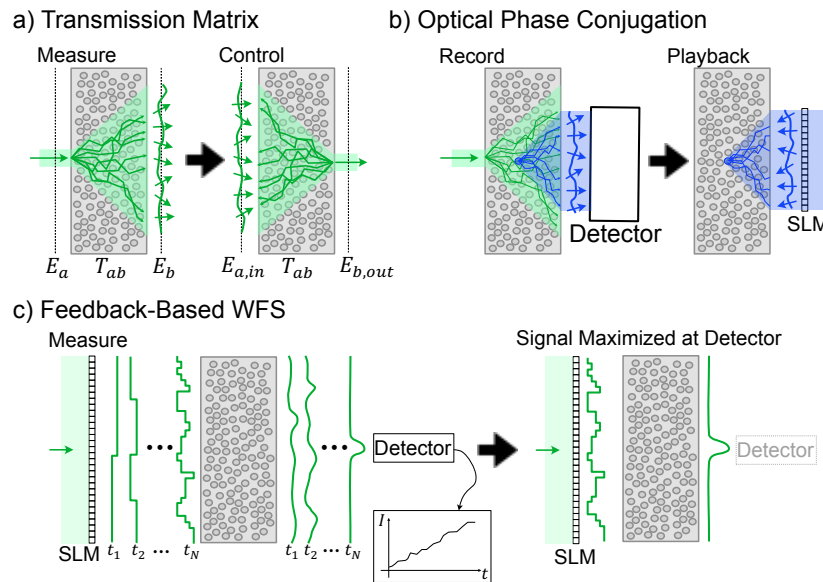


Figure 1.9: **Three methods for performing wavefront shaping (WFS).** The desired wavefront can be controlled by a) characterizing the transmission matrix, b) using optical phase conjugation, or c) using feedback-based methods. A spatial light modulator (SLM) can be used to control the amplitude and phase of the wavefront.

In contrast to TM methods, OPC methods do not require characterization of a matrix and can operate on faster time-scales [35, 36]. OPC methods involve a 2-step process: (1) recording the wavefront of the desired light pattern, and (2) playing back the wavefront [37–39]. Due to the deterministic nature of scattering, the replayed light will re-trace the same path and yield the original input. This property is known as ‘time-reversal.’

For imaging applications, OPC methods often require what is known as a ‘guidestar,’ which is something that localizes the signal [30]. One example of a guidestar is a fluorescent bead located only at the focus spot, such that the fluorescent light emanates from a single location. Another example of a guidestar is an ultrasound focus, which ‘tags’ some of the light that passes through the focus and causes the light to shift to a different wavelength [40]. For OPC, only the wavefront of the tagged light is recorded and played back. Due to the time-reversal property, the replayed, tagged light retraces its path and converges at the location of the guidestar.

Lastly, in feedback-based methods, the incident wavefront is iteratively updated to

increase the signal at the detector [29]. The result of this process is that the incident wavefront is tailored such that the scattered outgoing wavefront has a bright spot of maximum intensity at the location of the detector.

WFS methods are useful for controlling the scattered light behavior and can be used to manipulate the scattered light to focus deep inside scattering media. This process can increase light delivery or imaging depth inside scattering media. However, WFS methods require either (1) transmission matrix measurements, which is time-intensive and are most suitable for static scattering media; (2) the presence of a guidestar, which is not always present or feasible; or (3) some method of acquiring feedback inside the scattering medium. Some of the methods presented in this section also require access to both sides of the medium. For these reasons, WFS methods are not suitable for all applications.

Multiple-Scattering Low Coherence Interferometry

Multiple-scattering low-coherence interferometry (msLCI) systems are another class of systems that are capable of imaging past the ballistic regime while retaining moderate resolution [41–43]. In contrast to LOT and DOT, msLCI systems aim to detect only a subset of the scattered light from the sample, namely the weakly-scattered ‘snake’ photons that are more predominantly scattered in the forward direction (Fig. 1.6). These snake photons exist in higher proportion in scattering media where light has higher probability of forward scattering. One example of such a scattering media is biological tissue.

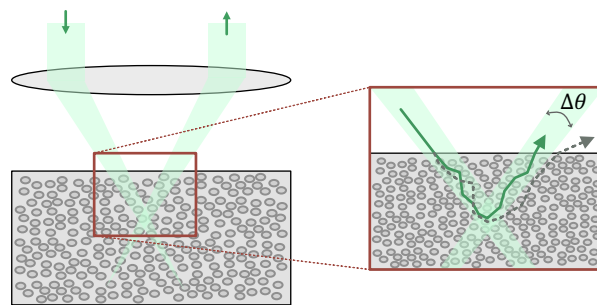


Figure 1.10: **Concept of multiple-scattering low-coherence interferometry (msLCI).** In multiple-scattering low coherence interferometry, light is detected within a narrow angular collection region, which helps preferentially detect more forward scattered light.

In order to preferentially detect these more weakly scattered snake photons, msLCI

systems employ illumination and detection schemes that have a narrow angular range such that more strongly scattered light, which scatter at larger angles, are rejected (Fig. 1.10). They couple this narrow angular collection with a technique called interferometry to increase the detection sensitivity.

msLCI systems work best in scattering media where light has a higher probability of forward scattering. With msLCI, the authors were able to image past the ballistic limit with resolutions of around 30% the imaging depth.

Speckle Correlation Imaging

The last diffuse imaging method we will cover is Speckle Correlation Imaging (SCI). SCI permits imaging of objects hidden behind scattering layers with diffraction-limited resolution (Fig. 1.11) [44]. In SCI, a light source illuminates the object, and light from the object propagates through a scattering medium. Due to optical scattering, the detected camera image is a randomized pattern that contains information about the object, even though no object is discernible. From this randomized pattern, it is possible to computationally recover an image of the object.

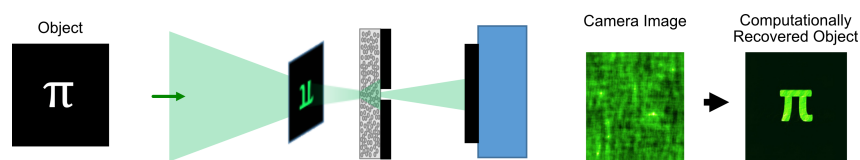


Figure 1.11: **Concept of Speckle Correlation Imaging (SCI).** SCI allows for imaging of an object hidden behind a thin, scattering layer.

In order to recover the hidden object, SCI leverages the angular correlations inherent in the scattering process (Fig. 1.12). Briefly, when light is scattered by the scattering media, the output wavefront appears as a fine-grained speckle pattern with randomized intensity and phase. Within a certain angular range, a tilt in the incident light beam can result in a tilt in the output wavefront [45–47]. Taken far away, a shift in the light beam results in a tilt of the incident light beam at the surface of the scattering media. This tilted light beam results in a tilt in the scattered wavefront at the output of the scattering layer, which, when propagated over a distance, appears as a shift in the scattered wavefront.

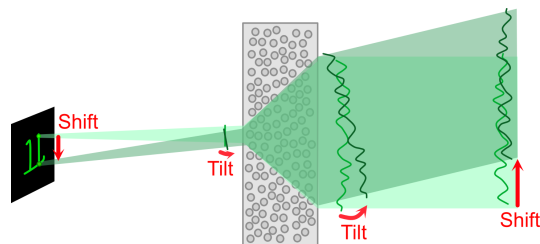


Figure 1.12: **Tilt-tilt correlations in SCI.** Speckle Correlation Imaging leverages the fact that a tilt in the incident beam can, in certain scenarios, result in a tilt in the output scattered wavefront.

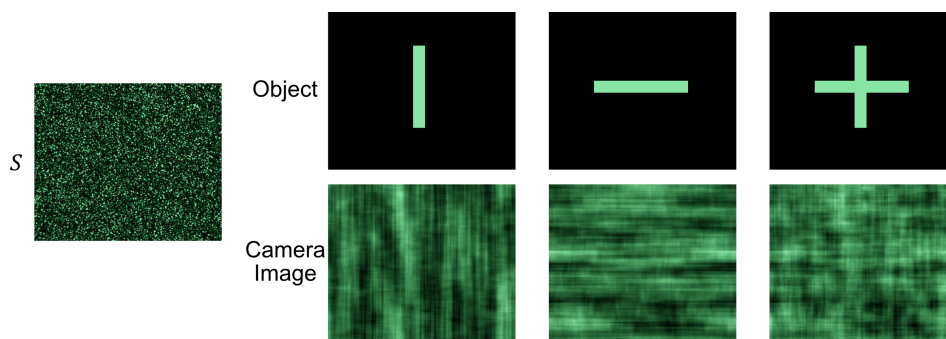


Figure 1.13: **Object information encoding in SCI.** In Speckle Correlation Imaging, the detected camera image contains information about the object.

In Fig. 1.13 is an example of S as well as some objects and the corresponding images that would be detected at the camera. The object can be considered as a sum of shifted point sources. Each of these point sources results in shifted versions of the scattered wavefront, S . Since the detector captures all of the shifted version of S , the camera images appear to be smeared in directions that correspond to the object. In this manner, although the camera images do not resemble the object, they contain information about the object, which can be used to computationally retrieve the original object.

A more detailed treatment of speckle patterns and angular correlations has been presented in Sections 2.4.

1.3 Goals of this Thesis

In this thesis, we will primarily explore methods to overcome or harness scattering in order to push the depths at which we can perform imaging. Since the scattered light does not decay exponentially with depth, unlike the ballistic light, making use

of the scattered light can result in deeper penetration. In this section, we will briefly present the goal of the projects in this thesis.

Imaging Moving Targets through Scattering Media

In Section 1.2, we discussed some of the various imaging methods that have been developed to deal with scattering and saw that ballistic imaging methods that aim to only detect the non-scattered or singly-scattered light have a limited depth of penetration. In contrast, many of the methods that detect and make use of the scattered light can image deeper, but are not able to retain diffraction-limited resolution.

Among the many techniques presented in Section 1.2, Speckle Correlation Imaging (SCI) was capable of performing imaging through scattering media at diffraction-limited resolution by exploiting angular correlations in the scattered process. A crucial component of SCI was that the light from the object was modelled as shifted point sources, and only the light from the object was detected (dark-field scenario). However, in many scenarios, it is not possible to restrict the detected light to only come from the object. For example, in scenarios such as imaging an embryo within an egg shell, or imaging an item embedded in tissue, the detected light also transmits through the background medium (bright-field scenario). In situations such as these, conventional SCI fails to reconstruct the object (Fig. 1.14).

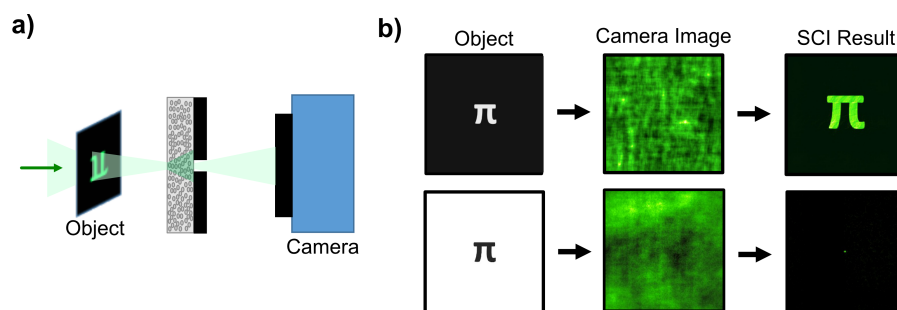


Figure 1.14: **Limitation of SCI.** SCI works well when only the object transmits/emits light, but fails when the background also transmits/emits light.

In Chapter 3 of this thesis, I present a novel technique that extends SCI to imaging objects in bright-field scenarios by using object motion to distinguish and remove light that comes from the background. This project, called ‘Imaging Moving Targets through Scattering Medium,’ provides a method for performing imaging of both dark-field and bright-field objects through scattering medium at diffraction-limited resolution.

Speckle-Resolved Optical Coherence Tomography

In Section 1.2, the various methods such as LOT, DOT, and SCI detected the scattered light indiscriminately and required computational techniques to reconstruct the object information. In contrast, msLCI directly computed the energy from a subset of the scattered photons to enable imaging at deeper depths while retaining moderate resolution. In msLCI, the selective detection of the weakly-scattered ‘snake’ photons was achieved by employing an illumination and detection scheme with a narrow angular range. Even though msLCI also utilized interferometry to sensitively detect the snake photons, incoherent averaging of multiple measurements, up to 10^6 scans, was sometimes required to increase the signal-to-noise ratio in order to detect the weak signal.

In Chapter 4 of this thesis, I present a method for imaging deeper in scattering media by efficiently detecting the back-scattered speckle light from the sample. I first investigate whether spatial, angular, or combined spatio-angular gating might be best at preserving resolution while imaging deep in scattering media. I also develop a novel method, termed speckle-resolved detection, that coherently detects the back-scattered sample light and show that this method can achieve the same signal boost as the incoherent averaging that msLCI performs, but in a single-shot manner. With this system, I demonstrate imaging in scattering media past the ballistic imaging at moderate resolution.

Imaging Syringe Layer Heterogeneity

The final project in my thesis switches gears from scattering media and looks into the development of an imaging system with the goal of improving quality control for pre-filled syringe products. Pre-filled syringes (PFS) are syringes that are pre-loaded with drugs. These pre-filled syringes are increasingly being adopted due to their accurate dosage, ease of usage, and convenience. In PFSs, the inner surface of the glass syringe is often coated with silicone oil, which functions as a lubricant to ensure complete drug dispensation and smooth injection. However, this silicone oil can also contribute to particle formation, by sloughing off the wall or by promoting drug aggregation and adsorption. Understanding and reducing particle formation is important as the number of particles is regulated and cannot exceed a certain threshold.

In this project, we use light to non-destructively image the evenness of the silicone oil layer that coats the inner surface of a syringe. Since the presence of silicone oil is

correlated with particle formation, the hypothesis is that unevenness in the silicone oil layer exposes more surface area for interactions, which can result in particle formation. We then apply our system in a preliminary study on whether the silicone heterogeneity impacts particle formation.

1.4 Thesis Outline

The remainder of this thesis is organized as follows. In Chapter 2, we introduce some background information and relevant concepts which form the foundation for the projects in Chapters 3 to 5. In Chapter 3, we show that we can leverage the temporal and spatial correlations in the scattering process to computationally ‘unscramble’ the detected light information and retrieve an image of a target hidden behind a scattering media. Chapter 4 presents investigations on preferentially detecting the more weakly scattered light in order to push the depth of imaging while preserving some spatial resolution. In this chapter, we also introduce the concept of speckle-resolved detection and show how it helps us coherently detect the multiply scattered light in an effective and sensitive manner. Finally, in Chapter 5, we develop a system that visualizes and characterizes the thin silicone oil layer that covers the inner surface of empty syringes. This is important as the evenness of the silicone oil layer impacts the functionality of the syringe.

BIBLIOGRAPHY

- [1] D. Perevoznik, R. Nazir, R. Kiyam, K. Kurselis, B. Koszarna, D. T. Gryko, and B. N. Chichkov, “High-speed two-photon polymerization 3d printing with a microchip laser at its fundamental wavelength,” *Optics express*, vol. 27, no. 18, pp. 25119–25125, 2019.
- [2] A. Vyatskikh, S. Delalande, A. Kudo, X. Zhang, C. M. Portela, and J. R. Greer, “Additive manufacturing of 3d nano-architected metals,” *Nature communications*, vol. 9, no. 1, pp. 1–8, 2018.
- [3] P. Massey and M. M. Hanson, “Astronomical spectroscopy,” *Planets, Stars and Stellar Systems*, vol. 2, pp. 35–98, 2013.
- [4] A. T. Feldman and D. Wolfe, “Tissue processing and hematoxylin and eosin staining,” in *Histopathology*, pp. 31–43, Springer, 2014.
- [5] K. K. Tremper, “Pulse oximetry,” *Chest*, vol. 95, no. 4, pp. 713–715, 1989.
- [6] K. Deisseroth, “Optogenetics,” *Nature Methods*, vol. 8, no. 1, pp. 26–29, 2011.
- [7] M. W. Jenkins, A. Duke, S. Gu, Y. Doughman, H. Chiel, H. Fujioka, M. Watanabe, E. Jansen, and A. Rollins, “Optical pacing of the embryonic heart,” *Nature Photonics*, vol. 4, no. 9, pp. 623–626, 2010.
- [8] V. V. Tuchin, X. Xu, and R. K. Wang, “Dynamic optical coherence tomography in studies of optical clearing, sedimentation, and aggregation of immersed blood,” *Applied Optics*, vol. 41, no. 1, pp. 258–271, 2002.
- [9] C. G. Rylander, O. F. Stumpp, T. E. Milner, N. J. Kemp, J. M. Mendenhall, K. R. Diller, and A. J. Welch, “Dehydration mechanism of optical clearing in tissue,” *Journal of biomedical optics*, vol. 11, no. 4, p. 041117, 2006.
- [10] K. Chung, J. Wallace, S.-Y. Kim, S. Kalyanasundaram, A. S. Andalman, T. J. Davidson, J. J. Mirzabekov, K. A. Zalocusky, J. Mattis, A. K. Denisin, *et al.*, “Structural and molecular interrogation of intact biological systems,” *Nature*, vol. 497, no. 7449, pp. 332–337, 2013.
- [11] I. Costantini, R. Cicchi, L. Silvestri, F. Vanzi, and F. S. Pavone, “In-vivo and ex-vivo optical clearing methods for biological tissues,” *Biomedical optics express*, vol. 10, no. 10, pp. 5251–5267, 2019.
- [12] A. M. Larson, “Multiphoton microscopy,” *Nature Photonics*, vol. 5, no. 1, pp. 1–1, 2011.
- [13] L. Wang, P. P. Ho, X. Liang, H. Dai, and R. Alfano, “Kerr–fourier imaging of hidden objects in thick turbid media,” *Optics letters*, vol. 18, no. 3, pp. 241–243, 1993.

- [14] G. H. Chapman, M. Trinh, N. Pfeiffer, G. Chu, and D. Lee, "Angular domain imaging of objects within highly scattering media using silicon micromachined collimating arrays," *IEEE Journal of selected topics in quantum electronics*, vol. 9, no. 2, pp. 257–266, 2003.
- [15] L. Wang, P. Ho, C. Liu, G. Zhang, and R. Alfano, "Ballistic 2-d imaging through scattering walls using an ultrafast optical kerr gate," *Science*, vol. 253, no. 5021, pp. 769–771, 1991.
- [16] M. D. Duncan, R. Mahon, L. L. Tankersley, and J. Reintjes, "Time-gated imaging through scattering media using stimulated raman amplification," *Optics letters*, vol. 16, no. 23, pp. 1868–1870, 1991.
- [17] K. Yoo, Q. Xing, and R. Alfano, "Imaging objects hidden in highly scattering media using femtosecond second-harmonic-generation cross-correlation time gating," *Optics letters*, vol. 16, no. 13, pp. 1019–1021, 1991.
- [18] S. Hyde, N. Barry, R. Jones, J. Dainty, P. French, M. Klein, and B. Wechsler, "Depth-resolved holographic imaging through scattering media by photorefraction," *Optics letters*, vol. 20, no. 11, pp. 1331–1333, 1995.
- [19] L. V. Wang and H.-i. Wu, *Biomedical optics: principles and imaging*. John Wiley & Sons, 2012.
- [20] Y. Pan, R. Birngruber, and R. Engelhardt, "Contrast limits of coherence-gated imaging in scattering media," *Applied optics*, vol. 36, no. 13, pp. 2979–2983, 1997.
- [21] G. Indebetouw and P. Klysubun, "Imaging through scattering media with depth resolution by use of low-coherence gating in spatiotemporal digital holography," *Optics Letters*, vol. 25, no. 4, pp. 212–214, 2000.
- [22] D. Huang, E. A. Swanson, C. P. Lin, J. S. Schuman, W. G. Stinson, W. Chang, M. R. Hee, T. Flotte, K. Gregory, C. A. Puliafito, *et al.*, "Optical coherence tomography," *science*, vol. 254, no. 5035, pp. 1178–1181, 1991.
- [23] W. Geitzenauer, C. K. Hitzenberger, and U. M. Schmidt-Erfurth, "Retinal optical coherence tomography: past, present and future perspectives," *British Journal of Ophthalmology*, vol. 95, no. 2, pp. 171–177, 2011.
- [24] E. M. Hillman, D. A. Boas, A. M. Dale, and A. K. Dunn, "Laminar optical tomography: demonstration of millimeter-scale depth-resolved imaging in turbid media," *Optics letters*, vol. 29, no. 14, pp. 1650–1652, 2004.
- [25] E. M. Hillman, O. Bernus, E. Pease, M. B. Bouchard, and A. Pertsov, "Depth-resolved optical imaging of transmural electrical propagation in perfused heart," *Optics express*, vol. 15, no. 26, pp. 17827–17841, 2007.

- [26] Y. Yamada and S. Okawa, "Diffuse optical tomography: Present status and its future," *Optical Review*, vol. 21, no. 3, pp. 185–205, 2014.
- [27] Y. Hoshi and Y. Yamada, "Overview of diffuse optical tomography and its clinical applications," *Journal of biomedical optics*, vol. 21, no. 9, p. 091312, 2016.
- [28] H. Dehghani, S. Srinivasan, B. W. Pogue, and A. Gibson, "Numerical modelling and image reconstruction in diffuse optical tomography," *Philosophical Transactions of the Royal Society A: Mathematical, Physical and Engineering Sciences*, vol. 367, no. 1900, pp. 3073–3093, 2009.
- [29] I. M. Vellekoop, "Feedback-based wavefront shaping," *Optics express*, vol. 23, no. 9, pp. 12189–12206, 2015.
- [30] R. Horstmeyer, H. Ruan, and C. Yang, "Guidestar-assisted wavefront-shaping methods for focusing light into biological tissue," *Nature photonics*, vol. 9, no. 9, pp. 563–571, 2015.
- [31] M. Jang, Y. Horie, A. Shibukawa, J. Brake, Y. Liu, S. M. Kamali, A. Arbabi, H. Ruan, A. Faraon, and C. Yang, "Wavefront shaping with disorder-engineered metasurfaces," *Nature photonics*, vol. 12, no. 2, pp. 84–90, 2018.
- [32] S. Popoff, G. Lerosey, M. Fink, A. C. Boccara, and S. Gigan, "Controlling light through optical disordered media: transmission matrix approach," *New Journal of Physics*, vol. 13, no. 12, p. 123021, 2011.
- [33] M. Kim, W. Choi, Y. Choi, C. Yoon, and W. Choi, "Transmission matrix of a scattering medium and its applications in biophotonics," *Optics express*, vol. 23, no. 10, pp. 12648–12668, 2015.
- [34] J. Xu, H. Ruan, Y. Liu, H. Zhou, and C. Yang, "Focusing light through scattering media by transmission matrix inversion," *Optics express*, vol. 25, no. 22, pp. 27234–27246, 2017.
- [35] D. Wang, E. H. Zhou, J. Brake, H. Ruan, M. Jang, and C. Yang, "Focusing through dynamic tissue with millisecond digital optical phase conjugation," *Optica*, vol. 2, no. 8, pp. 728–735, 2015.
- [36] Y. Liu, C. Ma, Y. Shen, J. Shi, and L. V. Wang, "Focusing light inside dynamic scattering media with millisecond digital optical phase conjugation," *Optica*, vol. 4, no. 2, pp. 280–288, 2017.
- [37] Z. Yaqoob, D. Psaltis, M. S. Feld, and C. Yang, "Optical phase conjugation for turbidity suppression in biological samples," *Nature photonics*, vol. 2, no. 2, pp. 110–115, 2008.
- [38] I. M. Vellekoop, M. Cui, and C. Yang, "Digital optical phase conjugation of fluorescence in turbid tissue," *Applied physics letters*, vol. 101, no. 8, p. 081108, 2012.

- [39] D. Wang, E. H. Zhou, J. Brake, H. Ruan, M. Jang, and C. Yang, “Focusing through dynamic tissue with millisecond digital optical phase conjugation,” *Optica*, vol. 2, no. 8, pp. 728–735, 2015.
- [40] Y. M. Wang, B. Judkewitz, C. A. DiMarzio, and C. Yang, “Deep-tissue focal fluorescence imaging with digitally time-reversed ultrasound-encoded light,” *Nature communications*, vol. 3, no. 1, pp. 1–8, 2012.
- [41] M. G. Giacomelli and A. Wax, “Imaging beyond the ballistic limit in coherence imaging using multiply scattered light,” *Optics express*, vol. 19, no. 5, pp. 4268–4279, 2011.
- [42] T. E. Matthews, M. G. Giacomelli, W. J. Brown, and A. Wax, “Fourier domain multispectral multiple scattering low coherence interferometry,” *Applied optics*, vol. 52, no. 34, pp. 8220–8228, 2013.
- [43] Y. Zhao, J. R. Maher, M. M. Ibrahim, J. S. Chien, H. Levinson, and A. Wax, “Deep imaging of absorption and scattering features by multispectral multiple scattering low coherence interferometry,” *Biomedical optics express*, vol. 7, no. 10, pp. 3916–3926, 2016.
- [44] O. Katz, P. Heidmann, M. Fink, and S. Gigan, “Non-invasive single-shot imaging through scattering layers and around corners via speckle correlations,” *Nature photonics*, vol. 8, no. 10, pp. 784–790, 2014.
- [45] S. Feng, C. Kane, P. A. Lee, and A. D. Stone, “Correlations and fluctuations of coherent wave transmission through disordered media,” *Physical review letters*, vol. 61, no. 7, p. 834, 1988.
- [46] I. Freund, M. Rosenbluh, and S. Feng, “Memory effects in propagation of optical waves through disordered media,” *Physical review letters*, vol. 61, no. 20, p. 2328, 1988.
- [47] B. Judkewitz, R. Horstmeyer, I. M. Vellekoop, I. N. Papadopoulos, and C. Yang, “Translation correlations in anisotropically scattering media,” *Nature physics*, vol. 11, no. 8, pp. 684–689, 2015.

*Chapter 2***BACKGROUND INFORMATION**

In this chapter, we present some background information regarding light-tissue interactions, light coherence, and interferometry. The first section deals with light-tissue interactions, with a focus on the physics and origin of scattering and the speckle pattern that is formed by the scattered light. This speckle pattern exhibits useful statistical properties and correlations which allows us to manipulate or ‘unscramble’ the scattered information. In the second half of this chapter, we present concepts relating to light coherence and interference and show how interferometry can be used to detect weak signal with high sensitivity.

These concepts provide the foundation for understanding the projects presented in Chapters 3-5. In Chapter 3, the correlations within the speckle pattern are exploited to ‘unscramble’ the scattered light and retrieve the object hidden behind the scattering layer. Controlling the temporal and spatial coherence of light is also critical for this project. In Chapter 4, we make use of the fact that, in certain media, the light scatters more preferentially in the forward direction. In such media, the preferential detection of the more forward scattered light provides imaging at deeper depths with moderate resolution. Interference is used to efficiently and coherently detect the intensity of the back-scattered speckle field from the sample. Lastly, in Chapter 5, interference is used to image the heterogeneity of the otherwise-transparent silicone oil that lines the inner surface of syringes.

2.1 Light-Tissue Interactions

When light interacts with matter, it may be absorbed, scattered, and/or reflected. These various processes give rise to the various sources of contrast in optical imaging. The many sources of contrast stem, in part, from the fact that photons at visible and near-infrared wavelengths have energies that are able to interact with molecules. Atoms and molecules have discrete energy levels. When the energy of the photon matches the energy difference between two energy levels of the molecule, the photon may interact and get absorbed. Contrast mechanisms such as absorption and fluorescence, for example, rely on this energy matching.

The Jablonski diagram provides a visual depiction of the various energy states of

the molecule and is convenient when talking about light-matter interactions. An example of a Jablonski diagram, along with some common transitions, is shown in Fig. 2.1. In the Jablonski diagram, the vertical axis depicts energy and the horizontal axis depicts the spin state. The bold lines refer to the electronic states of the molecule whereas the thinner lines refer to vibrational states within each electronic state. For this particular Jablonski diagram, radiative transitions have been shown in solid arrows and non-radiative transitions have been shown in dashed arrows.

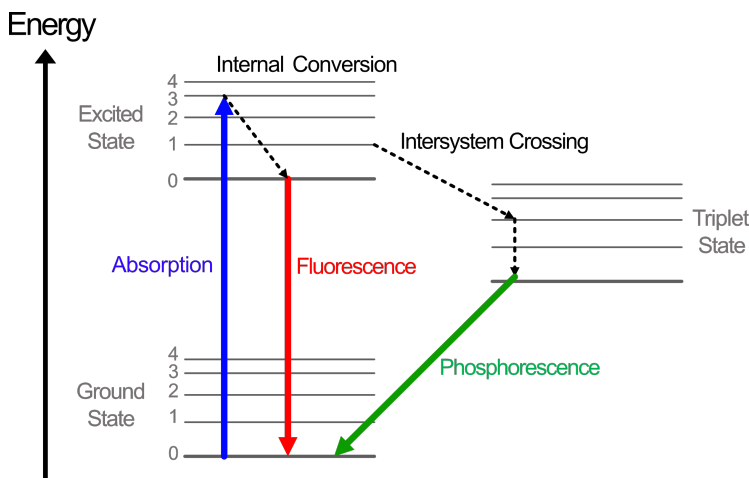


Figure 2.1: A Jablonski diagram showing the energy states of a molecule along with some common interactions.

Radiative transitions include the absorption and emission of photons. An incident photon may be absorbed if its energy matches the difference in the energy states of the molecule, ΔE . The energy of a photon is given by

$$E = \frac{hc}{\lambda} = h\nu \quad (2.1)$$

where h is Planck's constant, $c = 2.998 \times 10^8$ m/s is the speed of light, λ is the wavelength of light, and ν is the frequency of light. An excited molecule may also radiatively emit a photon as fluorescence. The emitted fluorescence will have a wavelength that corresponds to the energy released; that is $\lambda_{\text{fluorescence}} = \frac{\Delta E}{hc}$. The molecule can also relax and dissipate the energy as heat. Other radiative transitions, such as phosphorescence, and non-radiative transitions, such as internal conversion and intersystem crossing, have been included in the Jablonski diagram.

2.2 Absorption

The processes shown above in the Jablonski diagram all start with the absorption of a photon. In this section, we describe some mathematical equations and variables used to describe the absorption of light by a single particle and a collection of particles.

For a single absorbing particle, or absorber, with geometrical cross-sectional area σ_g , the strength of its absorption is captured by the absorption cross-section $\sigma_a = Q_a \sigma_g$, where Q_a is the absorption efficiency.

The absorption coefficient μ_a describes the collective absorptive strength of a medium with multiple absorbers and is defined as

$$\mu_a = N_a \sigma_a. \quad (2.2)$$

Here N_a is the number density, or number of absorbers per unit volume of the material.

When light with intensity I_0 is incident upon a medium that only contains absorbers, its intensity is attenuated as it propagates. This attenuation can be described with Beer's law, which states that

$$I = I_0 e^{-\mu_a x}, \quad (2.3)$$

where x is the distance travelled in the absorptive medium.

2.3 Scattering

Another common light-matter interaction is scattering. Scattering occurs due to the presence of refractive index inhomogeneities in the media. For example, in the case of fog, small water particles suspended in air cause light to scatter. In tissue, biological components such as cells, mitochondria, and collagen fibrils cause light to scatter. Unlike absorption, elastic scattering does not cause a loss in energy; instead, the photon is merely deflected from its original path. Here, we first describe light scattering by a single particle and then expand to a collection of particles. We also describe the collective behavior of the scattered light that propagates through the scattering material.

Scattering by a Single Particle

Similar to the case of absorption, for a single scattering particle, or scatterer, we can define a scattering cross-section $\sigma_s = Q_s \sigma_g$ which provides a measure of the

strength of scattering. Here, Q_S is the scattering efficiency and σ_g is the geometrical cross-sectional area.

The scattering efficiency and intensity distribution of the light scattered off of a single particle depends on two factors: (1) the size of the scattering particle relative to the light wavelength, and (2) the relative amount of refractive index mismatch between the particle and its surrounding medium. In general, we can consider the following three regimes of scattering particle size: (1) $d \ll \lambda$, (2) $d \approx \lambda$, and (3) $d \gg \lambda$. Here, d refers to the diameter of the scatterer. When $d \ll \lambda$, light scattering can be described by Rayleigh theory. When $d \approx \lambda$, light scattering can be described with Mie theory. Finally, when $d \gg \lambda$, geometrical optics can be used to determine light behavior. We provide a short description of the Mie and Rayleigh regimes below; for a more thorough treatment of these theories, please refer to refs. [1, 2].

In the Rayleigh regime, the intensity distribution of the scattered light I_s follows:

$$I_s(r, \theta) = I_0 8\pi^4 n_m^4 \left(\frac{n_s^2 - n_m^2}{n_s^2 + 2n_m^2} \right) \frac{a^6}{r^2 \lambda^4} (1 - \cos^2 \theta) \propto \frac{1}{\lambda^4} \quad (2.4)$$

where I_0 is the intensity of the incident light, $a = 0.5d$ is the particle radius, and r, θ are polar coordinates. From the above equation, we see that Rayleigh scattering has an inverse dependency on λ^4 . Thus, shorter wavelengths will be scattered much more strongly. In the atmosphere, Rayleigh scattering is the reason behind the sky appearing blue.

In the Mie regime, the intensity distribution can be found by solving the exact solution to Maxwell's equations. Of note, Mie theory can be applied to find the intensity distribution to any size of scattering particle, provided that the particle is spherical. The scattering efficiency and intensity distribution of the particle depends on the relative size of the scatterer to the wavelength as well as the refractive index mismatch between the scatterer and its surrounding medium. The former factor is captured by the size parameter $x = \frac{2\pi n_s a}{\lambda} = ka$ where a is the particle radius. Particles with larger size parameters tend to scatter light more in the forward direction.

Scattering by a collection of particles

In Section 2.3, we considered the intensity distribution of light that is scattered off of a single particle. Here, we consider scattering by a collection of particles and provide some useful parameters that can be used to characterize the scattering media.

The scattering strength of a medium is encapsulated by the scattering coefficient μ_s , which is defined as

$$\mu_s = N_s \sigma_s, \quad (2.5)$$

where N_s is the number of scattering particles per unit volume in the media and σ_s is the scattering cross-section of each scatterer. The scattering coefficient can be thought of as the average number of scattering events per unit distance. For example, a common value in biological tissue is $\mu_s = 10 \text{ mm}^{-1}$; this may be loosely interpreted as the photons will experience 10 scattering events on average per mm of travel distance.

The scattering coefficient also provides a measure of how the non-scattered light intensity will decay. The intensity of the non-scattered, ballistic light component can be described by Beer's law using:

$$I = I_0 e^{-\mu_s x} \quad (2.6)$$

where x is the thickness of the scattering medium.

Another important consideration is the directionality of scattering. While the Rayleigh and Mie theories do provide the scattering intensity distribution as a function of angle, it is helpful to have a single metric with which to compare the properties of various scattering media. The scattering anisotropy $g \in [-1, 1]$ is a single, dimensionless metric that describes the forward-directedness of the scattering process and is defined as

$$g = \langle \cos(\theta) \rangle = \int_0^\pi p(\theta) \cos(\theta) 2\pi \sin(\theta) d\theta, \quad (2.7)$$

where θ is the polar angle, $p(\theta)$ is the scattering pattern, and $\cos(\theta)$ is the component of scattering in the forward direction. $g < 0$ represents predominantly backward-directed scattering, $g \approx 0$ represents equal probability of scattering in the backward and forward directions, and $g > 0$ represents predominantly forward-directed scattering. In biological tissue, g is typically around 0.9.

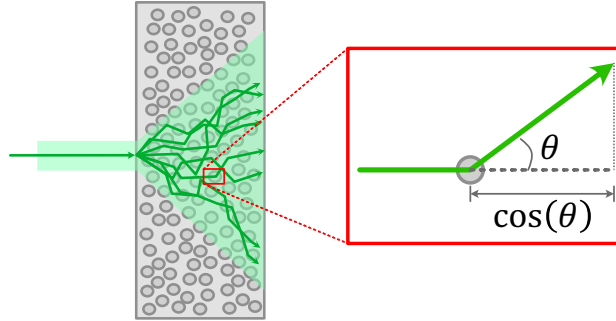


Figure 2.2: Polar angle θ for light scattering.

From μ_s and g , other important parameters that are used to characterize scattering media include the scattering mean free path and the transport mean free path. The scattering mean free path, denoted l_s or MFP, can be thought of as the average distance a particle travels before getting scattered and is defined as:

$$l_s = \frac{1}{\mu_s}. \quad (2.8)$$

In biological tissue, a common value is 0.1 mm, which can be loosely translated to mean that a photon will, on average, experience a scattering event every 0.1 mm.

For two media with the same scattering coefficient, a photon can experience more scattering events in a media with higher scattering anisotropy before its orientation becomes fully randomized. Since the scattering is directed, the orientation will not be fully random after one scattering event. This property is encapsulated by the reduced scattering coefficient μ'_s and the transport mean free path, which is denoted l_t , l^* , or TMFP. Loosely speaking, the transport mean free path can be thought of as the average distance a photon has to travel before its orientation is fully randomized. These parameters are related to the scattering coefficient and anisotropy through:

$$\mu'_s = \mu_s(1 - g) \quad (2.9)$$

$$l_t = \frac{1}{\mu'_s} = \frac{1}{\mu_s(1 - g)}. \quad (2.10)$$

In biological tissue, a good rule of thumb is that the TMFP is 1 mm.

Imaging Depth Regimes

When we consider light propagation in scattering-dominant media ($\mu_s \gg \mu_a$), we can consider 4 different regimes which provide a good rule-of-thumb about the

imaging depths that various optical imaging methods can operate in. These regimes are defined relative to the number of MFPs and TMFPs and are: the ballistic regime, the quasi-ballistic regime, the quasi-diffusive regime, and the diffusive regime [2]. As a reminder, the MFP (l_s) can be thought of as the average distance a photon travels before it encounters a scattering event, whereas the TMFP (l_t) is the average distance a photon has to travel before its direction is fully randomized and not correlated with the incident direction. Let d be the distance travelled. This distance d could correspond to imaging a target located within a depth of $0.5d$, or imaging through a scattering media with thickness $t = d$.

Distances within 1 MFP are called the ballistic regime. In this regime, light has a 37% probability of not being scattered, and the proportion of ballistic photons is dominant. The quasi-ballistic regime covers distances $d \in (l_s, l_t]$. Within this distance, the probability of photons not having scattered decreases, and the photons have experienced a few scattering events. However, the photons still retain a strong memory of the original incident direction. This also approximately corresponds to the depth limitation for Optical Coherence Tomography (OCT), which relies on the detection of ballistic photons.

Distances past 1 TMFP correspond to the quasi-diffusive and diffusive regime. For $d \in (l_t, 10l_t]$, which is the quasi-diffusive regime, photons have been scattered multiple times and their directions are partially randomized. Photons only have a weak memory of their original incidence direction; that is, their orientations are only weakly correlated with the incident direction. Lastly, for distances beyond 10 TMFPs, photons have lost memory of their original incidence direction and their directions are fully randomized. This is the diffusive regime.

For the project described in Chapter 4, we are interested in utilizing the scattered light to enable imaging within the quasi-diffusive regime.

Quantification of Imaging Depth

In this section, we consider how we can quantify imaging depth. To do this, let us consider imaging a target within scattering media at a depth z_{target} from the surface of the scattering media. Although the physical depth z_{target} may be used to quantify imaging depth, this metric does not take into account the scattering strength or scattering directionality. Therefore, to take these factors into account, one can instead quantify the imaging depth based on the number of mean free paths #MFPs or transport-mean-free-paths #TMFPs. These parameters provide a convenient way

for non-dimensionalizing the imaging depth and taking into account the scattering strength of a sample.

The parameter that is most suitable depends on the type of imaging. As a reminder, in scattering media, one can loosely consider three types of photon categories: (1) ballistic photons, which are non-scattered (in transmission mode) or singly-backscattered (in reflection mode) and provide the most direct information about the target; (2) snake photons, that are weakly scattered predominantly in the forward direction and still provide some direct information about the target; and (3) diffuse photons, which are strongly scattered (Fig. 2.3).

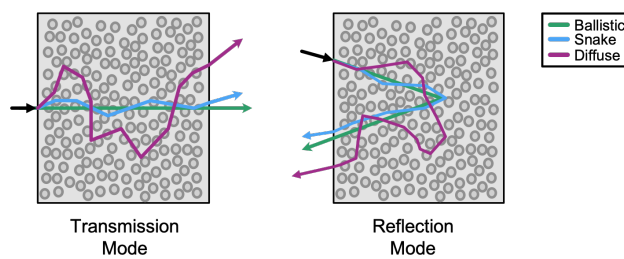


Figure 2.3: Types of photons that propagate in scattering media.

One can also consider three classes of methods for imaging in scattering media (Fig. 2.4):

- (1) ballistic imaging methods, which aim to predominantly detect only the ballistic light component and are able to image at diffraction-limited resolution;
- (2) snake imaging methods, which detect the ballistic and snake photons to enable imaging deeper in scattering media at moderate resolution;
- (3) diffuse imaging methods, which detect all three types of light and use computational methods to reconstruct information about the object.

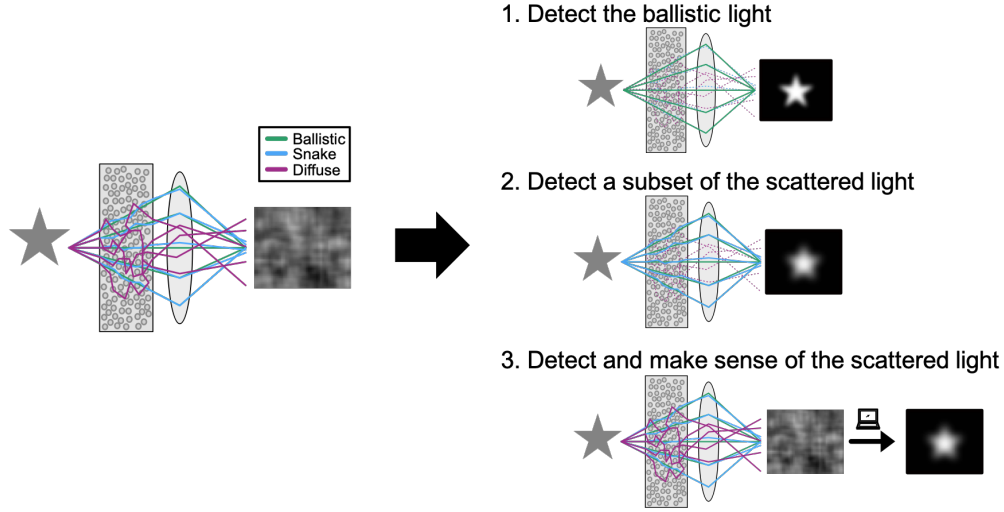


Figure 2.4: Strategies to image in scattering media.

For ballistic imaging methods, a natural parameter choice is the number of mean free paths #MFPs. This represents the number of mean free paths that the detected, ballistic light would have travelled; that is, $\text{\#MFPs} = \mu_s z$ where z is the distance that ballistic light travels. In transmission imaging geometries, $z = z_{\text{target}}$, whereas in reflection imaging geometries, $z = 2z_{\text{target}}$. #MFPs is a natural choice as the mean free path represents the average distance between scattering events, and a photon that encounters at least one scattering event, irrespective of scattering angle, is no longer ballistic.

For diffuse imaging methods, a natural parameter choice is the number of transport mean free paths #TMFPs. In diffuse imaging methods, multiply scattered light is predominantly detected to enable imaging in the diffusive regime. A natural length scale is the transport mean free path, which encapsulates the scattering strength as well as the scattering directionality and can be considered as the distance within which the photon propagation becomes randomized. For diffuse optical imaging methods, the effective attenuation coefficient μ_{eff} and effective penetration depth δ are

$$\mu_{\text{eff}} = \sqrt{\mu_a/D} = \sqrt{3\mu_a(\mu_a + \mu'_s)} \quad (2.11)$$

$$\delta = \frac{1}{\mu_{\text{eff}}} \quad (2.12)$$

where $D = \frac{1}{3(\mu_a + \mu'_s)}$ is the diffusion coefficient [2]. These depend, not on the scattering coefficient $\mu_s = \frac{1}{\text{MFP}}$ but the reduced scattering coefficient $\mu'_s = \frac{1}{\text{TMFP}}$.

Thus, the round-trip number of transport mean free paths, defined as $\#TMFPs = \mu'_s z$, is a more suitable parameter for imaging depth.

For snake imaging methods, it is not clear whether TMFP or MFP might provide a more appropriate length scale. Snake imaging methods aim to detect the predominantly forward-scattered light to enable imaging in the quasi-diffusive regime. In highly forward scattering media, one would expect a larger population of snake photons. Thus, both the scattering strength and scattering orientation are important. Many of the existing methods that make use of snake photons operate in the quasi-diffusive regime, at length scales that are on the order of less than a few transport mean free paths. The papers that are related to multiple-scattering low-coherence interferometry all use the mean free path as the length scale [3–5]. In this thesis, Chapter 4 describes the development of an imaging technology that aims to preferentially detect these snake photons to allow for imaging deeper in scattering media. For this work, we choose to use both $\#MFPs$ and $\#TMFPs$.

2.4 Speckle

In Sections 2.3, we considered the scattering of light due to a single particle and a collection of particles and provided some useful parameters to characterize scattering media. Here, we turn our attention to describing the pattern that the scattered light forms: a speckle pattern. The nature of speckle patterns is important for our project in Chapters 3 and 4: in Chapter 3, speckle correlations are exploited to unscramble the scattered information, and in Chapter 4, the nature of speckle is used to boost the detected signal. Our notation follows closely to that of ref.[6]; readers are encouraged to refer to this reference for more detail.

When light transmits through disordered media or is reflected off a rough surface, it gives rise to a scattered wavefront. Through Huygen’s principle, each scattered light can be modelled as a wavelet. Due to the complex nature of the scattering process, each point in the scattered wavefront can be considered to be the contribution of multiple wavelets, each of which has travelled a different pathlength in tissue and therefore has a random phase and amplitude. The coherent summation of these contributing wavelets forms what is known as a speckle grain.

Fig. 2.5a provides an example of a speckle pattern. A speckle pattern consists of speckle grains of varying intensities. Bright speckles correspond to largely constructive interference whereas dark speckles correspond to largely destructive interference (Fig. 2.5b). Put another way, a speckle pattern has a randomly varying

intensity profile that is a result of constructive and destructive interference from the scattered light. Since speckle patterns rely on interference, they only occur when light is coherent.

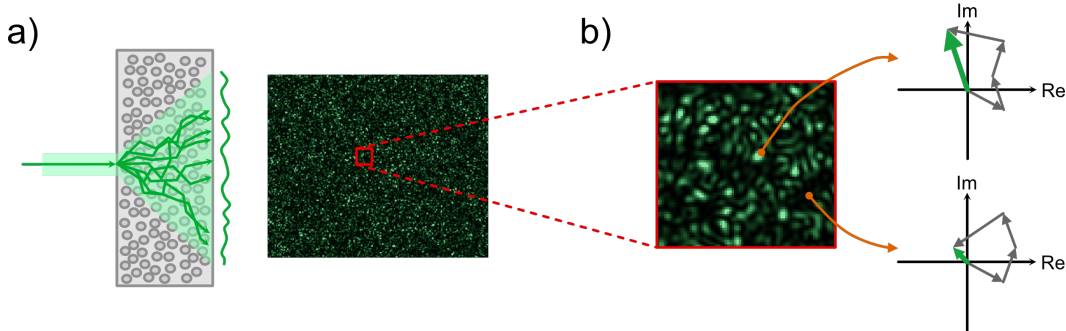


Figure 2.5: Scattered light forms a speckle pattern. a) When light propagates through scattering media, the scattered light forms what is known as a speckle field. The speckle field consists of speckle grains of varying intensity. b) Each speckle grain can be considered the sum of a set of random phasors. Bright speckles correspond to largely constructive interference whereas dark speckles correspond to largely destructive interference.

Mathematically, each contributing wavelet can be modelled as a complex number $\mathbf{a} = ae^{j\theta}$ with randomized amplitude a and phase θ . This complex number is also referred to as a phasor. Each speckle grain can be considered the sum of a set of random phasors. The resultant speckle grain can be represented as a complex phasor \mathbf{A} using

$$\mathbf{A} = Ae^{j\theta} = \frac{1}{\sqrt{N}} \sum_{i=1}^N \mathbf{a}_n = \frac{1}{\sqrt{N}} \sum_{i=1}^N a_n e^{j\theta_n}, \quad (2.13)$$

where $\frac{1}{\sqrt{N}}$ is added as a scaling factor such that the second moment is finite as $N \rightarrow \infty$. Here, boldface letters refer to vectors whereas regular fonts refer to scalars.

For this section, we make the following assumptions:

1. The amplitudes and phases of the different component phasors are statistically independent of each other. That is, a_n, a_m and θ_n, θ_m are statistically independent for $n \neq m$.
2. For a given phasor, the amplitude a_n and phase θ_n are statistically independent.
3. The phases θ_n are uniformly distributed between $(-\pi, \pi)$.

Speckle fields that match these assumptions are called ‘fully developed’ [6]. In the case where light is transmitted through scattering media that is sufficiently thick, such that the output field contains photons whose directions are fully randomized, these assumptions hold true.

In the case where $N \rightarrow \infty$, the central limit theory applies, and the real \mathcal{R} and imaginary \mathcal{I} parts of the resultant phasor A can be modelled as a circular complex Gaussian random variable:

$$p_{\mathcal{R},\mathcal{I}}(\mathcal{R}, \mathcal{I}) = \frac{1}{2\pi\sigma^2} \exp\left(-\frac{\mathcal{R}^2 + \mathcal{I}^2}{2\sigma^2}\right). \quad (2.14)$$

The probability distribution of the amplitude $p_A(A)$, phase $p_\theta(\theta)$, and intensity $p_I(I)$ can be described as follows:

$$p_A(A) = \frac{A}{\sigma^2} \exp\left(-\frac{A^2}{2\sigma^2}\right) \quad (2.15)$$

$$p_\theta(\theta) = \frac{1}{2\pi} \quad (2.16)$$

$$p_I(I) = \frac{1}{2\sigma^2} \exp\left(-\frac{I}{2\sigma^2}\right) = \frac{1}{\bar{I}} \exp\left(-\frac{I}{\bar{I}}\right) \quad (2.17)$$

where $\bar{I} = 2\sigma^2$ is the mean speckle intensity. The variance of the speckle intensity is $\sigma_I^2 = \bar{I}^2$. Thus, the contrast of the speckle, defined as the ratio of the standard deviation to the mean intensity, is

$$C = \frac{\sigma_I}{\bar{I}} = 1. \quad (2.18)$$

Of note, the speckle intensity is exponentially distributed. Therefore, speckle intensity fields contain many speckle grains of low intensity, and only few speckle grains of very high intensity.

Transmission Matrix

One way to model the scattering process is by using a transmission matrix formulation, which provides a linear, complex mapping between the electric fields at two planes (Fig. 2.6) [7, 8]. This is possible since scattering is a linear and deterministic process – as long as the scattering media is static, the input and output relationship is preserved. If we are able to measure or otherwise acquire information about the transmission matrix T , we have complete control over the outgoing electric field.

Transmission matrix formulation was used in the discovery of the spatial and angular correlations in the speckle field [9]. The angular correlations are exploited in Chapter 3 to enable imaging through scattering media at diffraction-limited resolution.

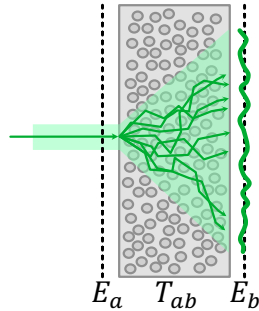


Figure 2.6: Transmission Matrix formulation for scattering.

First, we discuss the concept of optical modes, which allows us to discretize electric fields. Modes can be considered to be independent degrees of freedom. In transmission matrix formulation, a 2D $N \times N$ complex field is discretized using optical modes and linearized into a vector containing N^2 elements. Here, we only discuss spatial and k-space modes.

In the spatial domain, an optical mode is a point source located at a given position $\mathbf{x} = (x, y)$. That is, $\delta(\mathbf{x})$ is a point source located at \mathbf{x} . When the field is a speckle pattern, each speckle grain is an optical mode.

The Fourier dual of the spatial domain is the spatial frequency domain, or k-space $\mathbf{k} = (k_x, k_y)$. Here, $k_x = k_0 \sin(\theta_x)$, $k_y = k_0 \sin(\theta_y)$ and $k_0 = \frac{2\pi}{\lambda}$. Therefore the k-space domain also provides information about the direction of wave propagation. An optical mode in k-space $\delta(\mathbf{k})$ is a plane wave travelling in a single direction. Readers are directed to ref. [10] for more details about the spatial Fourier domain.

A transmission matrix T_{ab} that is $M \times N$ provides a mapping between an input plane E_a with N modes, and an output plane E_b with M modes; that is

$$E_b = T_{ab}E_a. \quad (2.19)$$

Knowledge of the transmission matrix of the scattering medium provides control over the output field. To see this, in the case where the entire scattering process can be characterized, the transmission matrix T is modelled as a random unitary matrix; that is,

$$T_{ab}T_{ab}^\dagger = I_M, \quad (2.20)$$

where $[\cdot]^\dagger$ denotes the conjugate transpose.

In order to control light through scattering medium, we are also interested in T_{ba} and how T_{ba} relates to T_{ab} . Due to optical reciprocity, we have that

$$T_{ab} = T_{ba}^T. \quad (2.21)$$

Combining Eqs. 2.20 and 2.21 results in

$$T_{ab}T_{ba}^* = I. \quad (2.22)$$

This result is remarkable. This result also forms the basis for using optical phase conjugation to manipulate light. To see this, let us consider a desired complex field $E_a = \delta(\mathbf{x})$. We start by sending light with complex field E_a through the scattering medium to yield E_b . For optical phase conjugation, we send the field E_b^* incident on the scattering medium to yield E_a^* . Mathematically,

$$\begin{aligned} T_{ba}E_b^* &= T_{ba}(T_{ab}E_a)^* \\ &= T_{ba}(T_{ba}^T E_a)^* \\ &= E_a^*. \end{aligned} \quad (2.23)$$

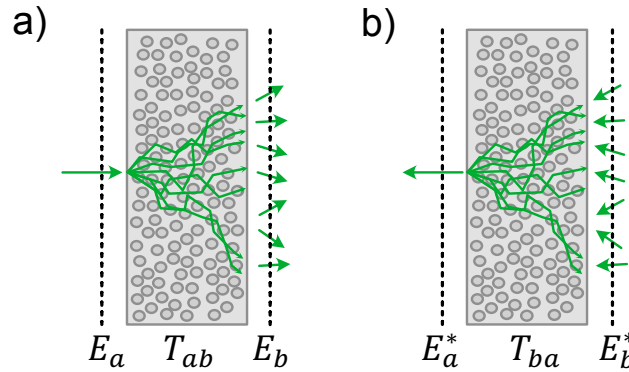


Figure 2.7: The transmission matrix formulation can be used to understand optical phase conjugation.

With information from the transmission matrix T_{ab} , it is also possible to control the output wavefront by shaping the input wavefront. In this case, to get the output $E_{b,target}$, the input wavefront must be set to:

$$E_{a,in} = T^\dagger E_{b,target}. \quad (2.24)$$

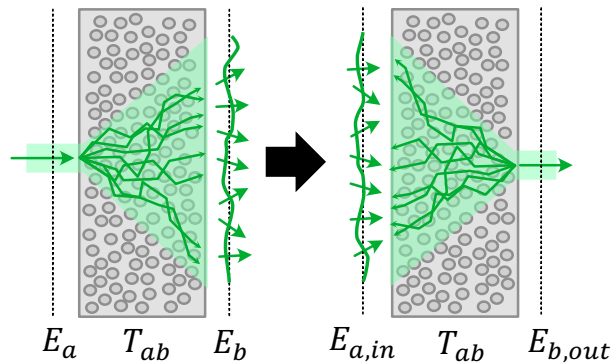


Figure 2.8: Transmission matrices can be used to control the output scattered wavefront.

In practice, we only have access to a subset of all the available modes, and can only measure a subset of the transmission matrix. In this case, the transmission matrix T_{ab} consists of elements t_{ba} whose elements are drawn from a circular Gaussian distribution. We can see this by considering the propagation of an input field consisting of only a single mode. The output field, which is equivalent to a column of T_{ab} , forms a speckle field whose real and imaginary components are drawn from a circular distribution. This is true for any column of T_{ab} . Therefore, the real and imaginary components of t_{ab} are drawn from a circular Gaussian distribution.

In this case, T is not unitary. However, since the elements t_{ab} are drawn from a circular Gaussian distribution, we have for some constant $\alpha > 0$ that [7]

$$T_{ba}^* T_{ab} = \alpha I_N. \quad (2.25)$$

Speckle Correlations

Another useful property of speckle fields is their angular and translational correlations, as shown in Fig. 2.9. Angular correlations are exploited to ‘unscramble’ the scattered light for the project in Chapter 3.

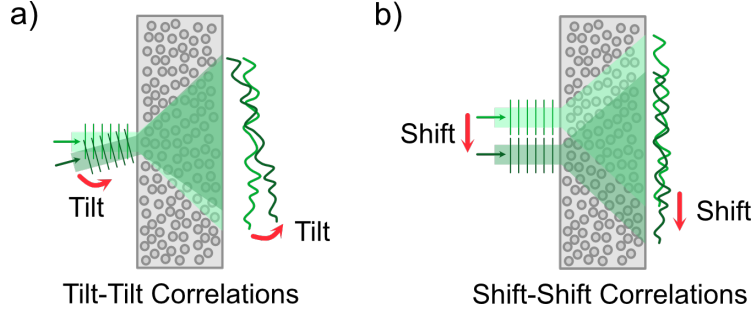


Figure 2.9: **Correlations in the scattered light pattern.** In certain cases, the speckle pattern can exhibit tilt-tilt correlations (a) and shift-shift correlations (b).

The tilt-tilt, or angular, correlation describes the scenario wherein a tilt in the incident beam can cause a corresponding tilt in the output speckle field. This correlation was first characterized using intensity-intensity correlations in the 1980s [11, 12]. For scattering media with thickness of $L \gg l_t$, where l_t is the transport mean free path, the intensity-intensity correlation was found to be:

$$C_I(\Delta k) \propto \frac{(\Delta k L)^2}{\sinh^2(\Delta k L)} \quad (2.26)$$

where $\Delta k \approx k_0|\Delta\phi|$ and $\Delta\phi$ is the tilt angle.

From this correlation, the range in which the correlation $C_I(\Delta k) \geq \frac{1}{2}$ is defined as the memory effect region $\Delta\phi_{ME} = \frac{\lambda}{\pi L}$ [12, 13]. Thus, the angular range in which the speckle field remains correlated is inversely related to the thickness of the scattering media L , and the tilt-tilt correlation is more evident in thin, highly-scattering materials. Interestingly, in the case where the scattering media reflects the light, such as a white wall, the medium thickness L is replaced by the transport mean free path of the media l_t . Therefore, $\Delta\phi_{ME} \propto \frac{1}{l_t}$, and more highly scattering surfaces exhibit larger tilt-tilt correlations.

The tilt-tilt correlations, and associated traditional memory effect, are more predominant in thin scattering media where $L \gg l_t$. In 2015, it was discovered that, in highly anisotropic media, there exists a complementary shift-shift correlation that describes how a shift in an input beam can result in a shift in the output beam [9]. To derive this, the authors defined the field-field correlation $C_E(\Delta k)$, which is related to the intensity-intensity correlation $C_I(\Delta k)$ via $C_I = |C_E|^2$. We will only present results here. For this section, plane a is the input plane and plane b is the output plane. We consider both spatial coordinates and spatial frequency coordinates.

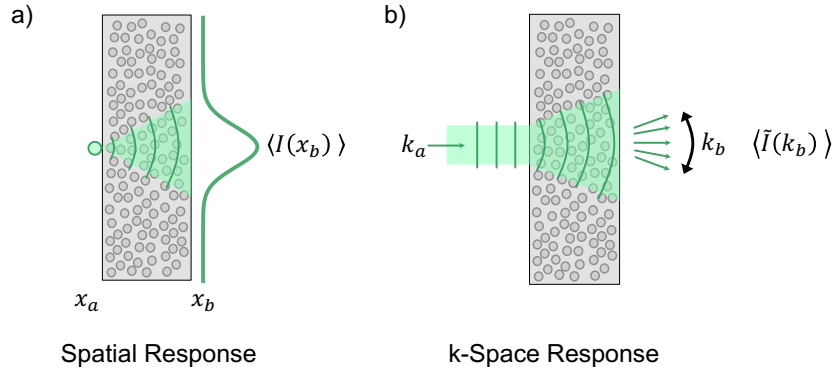


Figure 2.10: Spatial and k-Space intensity propagators.

Both tilt-tilt and shift-shift correlations manifest as structures in the transmission matrix. We define T_x as the transmission matrix in spatial domain, and \tilde{T}_k as the transmission matrix in k-space, such that for propagation from plane a to plane b,

$$E_b(x_b) = T_x E_a(x_a), \quad (2.27)$$

$$\tilde{E}_b(k_b) = \tilde{T}_k \tilde{E}_a(k_a). \quad (2.28)$$

For this section, variables with a $\tilde{(\cdot)}$ refer to variables in k-space.

When a point source is incident on a scattering media, light is scattered, and the output field forms a speckle pattern with some spatial extent depending on the scattering properties and thickness of the scattering media. The ensemble average of the output intensity field $\langle I(x_b) \rangle$ forms an envelope. Since a point source is mathematically represented as $E_a(x_a) = \delta(x_a)$, the average intensity propagator $\langle I(x_b) \rangle$ can be mathematically described as:

$$\langle I(x_b) \rangle = \langle |T_x(x_a, x_b)|^2 \rangle. \quad (2.29)$$

This intensity propagator is related to the field-field correlation via a Fourier transform.

$$\mathcal{F} [\langle |T_x(x_a, x_b)|^2 \rangle] \propto C_E(\Delta k) \quad (2.30)$$

The width of the intensity propagator is inversely related to the magnitude of the angular correlation and traditional memory effect. Therefore, thinner scattering media will have a larger memory effect range.

In a similar fashion, when a plane-wave is shone on a scattering media (corresponding to $\delta(k_a)$), the output field can have photons that travel in a wide range of

directions due to scattering. The ensemble average of the output intensity in k-space $\langle \tilde{I}(k_b) \rangle$ is limited in extent and depends on the scattering properties of the media: for the same thickness and scattering coefficient, there will be a smaller range in output angles, or k_b , for media with higher anisotropy. In the limit where $g = 1$, and all light is forward scattered, we have that $k_a \approx k_b$. This ‘k-space intensity propagator’ $\langle \tilde{I}(k_b) \rangle = \langle |\tilde{T}_k(k_a, k_b)|^2 \rangle$ is related to the shift-shift correlation via a Fourier transform.

$$\mathcal{F} [\langle |\tilde{T}_k(k_a, k_b)|^2 \rangle] \propto C_E(\Delta x) \quad (2.31)$$

Therefore, the range in output k-vectors is inversely related to the magnitude of the shift-shift correlation, and the translational memory effect is larger in more forward scattering materials.

These two correlations, the shift-shift and tilt-tilt, were combined in a generalized theorem that describes how a shift and tilt in the incident beam can result in a shift and tilt in the output speckle field [14]. Interested readers are encouraged to refer to [9, 11, 12, 14] for a more detailed treatment and description of speckle correlations and memory effect.

2.5 Coherence

In this section, we describe two types of coherence: spatial coherence and temporal coherence. Coherence is crucial in the formation of speckles and is related to all of the projects described in this thesis.

Temporal Coherence

Temporal coherence can be related to the degree with which a light wave or field is correlated with a time-delayed version of itself. The temporal coherence of a light source can be mathematically described as:

$$G(\tau) = \langle E(t)E^*(t + \tau) \rangle \quad (2.32)$$

where $\langle \cdot \rangle$ refers to time average and τ is the delay time. The above quantity can be normalized to yield the degree of coherence, $g(\tau) \in [0, 1]$, defined as

$$g(\tau) = \frac{\langle E(t)E^*(t + \tau) \rangle}{\langle E^*(t)E(t) \rangle}. \quad (2.33)$$

An important parameter for temporal coherence is the coherence time τ_c , which is the time it takes for the coherence to fall below a specified value such as $1/e$. A

related measure is the coherence length l_c , which is related to the coherence time as $l_c = c\tau_c$.

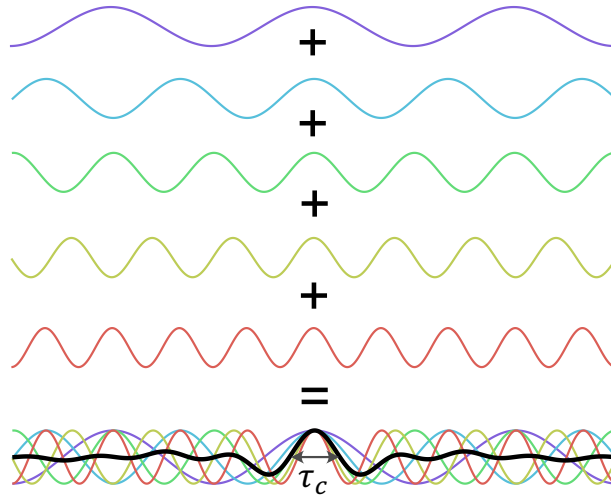


Figure 2.11: **Impact of spectral bandwidth on temporal coherence.** A wider spectral bandwidth is related to a shorter coherence time.

The temporal coherence of a light source is inversely related to the range of frequencies, or wavelengths, within a source. For a monochromatic source, which consists of a single wavelength, the temporal coherence can be infinitely long. In contrast, if the source consists of multiple wavelengths, then the wave is only correlated with itself for a short period of time (Fig. 2.11).

Spatial Coherence

Spatial coherence refers to the degree with which a wavefront is correlated with a spatially shifted version of itself. Stated another way, spatial coherence is related to a wave at two positions $\mathbf{r}_1, \mathbf{r}_2$ being able to interfere, when averaged over time.

Given a wavefront with complex field $E(\mathbf{r}, t)$, the spatial coherence is defined as

$$G(\mathbf{r}_1, \mathbf{r}_2) = \langle E(\mathbf{r}_1, t)E^*(\mathbf{r}_2, t) \rangle \quad (2.34)$$

where $\mathbf{r}_1, \mathbf{r}_2$ are two different positions and $\langle \cdot \rangle$ refers to time average. $\mathbf{r} = (x, y)$. The degree of spatial coherence can be computed as

$$g(\mathbf{r}_1, \mathbf{r}_2) = \frac{G(\mathbf{r}_1, \mathbf{r}_2)}{\sqrt{\langle E(\mathbf{r}_1, t)E^*(\mathbf{r}_1, t) \rangle \langle E(\mathbf{r}_2, t)E^*(\mathbf{r}_2, t) \rangle}}. \quad (2.35)$$

A plane wave has infinitely long spatial coherence. In contrast, a scattered wavefront has a very short spatial coherence. In fact, a speckle field is only spatially correlated to the extent of one speckle grain.

2.6 Interferometry

We end this chapter with a discussion on interferometry, which uses light interference to perform measurements. Interferometry has several advantages. Due to the high frequency of optical wavelengths, which is on the order of THz (10^{12} Hz), detectors are able to only measure the time-averaged intensity of light and not the complex field or phase. Interferometry provides the ability to indirectly measure the phase of light. This phase can provide valuable information, such as extremely precise measurement of refractive index changes or displacement, up to fractions of a wavelength. Such measurements of minute displacements are otherwise difficult due to the speed of light. Interferometry is also used to test the quality of surfaces and even prove the existence of gravitational waves! Another benefit, as we soon shall see, is that interferometry provides a method to perform sensitive detection of very weak signals.

In this section, we will discuss some basics of interferometry and common interferometer topologies. We will also present some common holographic systems and then end with the signal-to-noise advantage of interferometry.

Interferometry is based on the coherent addition of two or more beams. In this section, we will limit our discussion to two-beam interferometry. For two beams with complex fields $\mathbf{E}_1 = E_1 e^{j\theta_1}$ and $\mathbf{E}_2 = E_2 e^{j\theta_2}$, the detected intensity at the camera is

$$I = |\mathbf{E}_1 + \mathbf{E}_2|^2 = I_1 + I_2 + \mathbf{E}_1 \mathbf{E}_2^* + \mathbf{E}_1^* \mathbf{E}_2 = I_1 + I_2 + 2\sqrt{I_1 I_2} \cos(\theta_2 - \theta_1), \quad (2.36)$$

where $I = |\mathbf{E}|^2 = \mathbf{E} \mathbf{E}^*$ is the intensity. The terms $I_1 + I_2$ are called the ‘DC’ terms whereas the terms $\mathbf{E}_1 \mathbf{E}_2^*$, $\mathbf{E}_1^* \mathbf{E}_2$ are referred to as the ‘cross-terms’ or ‘AC’ terms. The amplitude of the cross-term depends on the relative phase shift $\Delta\theta = \theta_2 - \theta_1$. When $\Delta\theta = 0$, we have constructive interference, and the cross-term amplitude is maximum. When $\Delta\theta = \pi$, we have destructive interference, and the cross-term amplitude is minimal (Fig. 2.12).

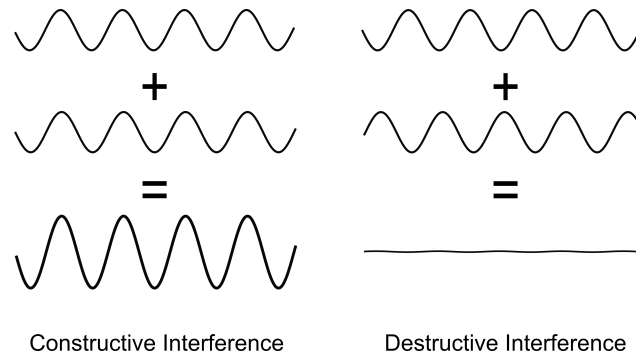


Figure 2.12: **Constructive and Destructive Interference.** A relative phase shift between two beams results in constructive or destructive interference.

Fig. 2.13 presents two common topologies for interferometry, namely Michelson interferometer (MI) and Mach-Zender interferometer (MZI). A basic MI consists of a single beamsplitter BS and two mirrors M . The incident light beam is split into two beams by BS . The two beams reflect off of mirrors and then are recombined by the same beamsplitter BS to interfere at the detector. In contrast, the basic MZI uses two separate beamsplitters – $BS1, BS2$ – to split the incident light beam into two paths and then recombine them.

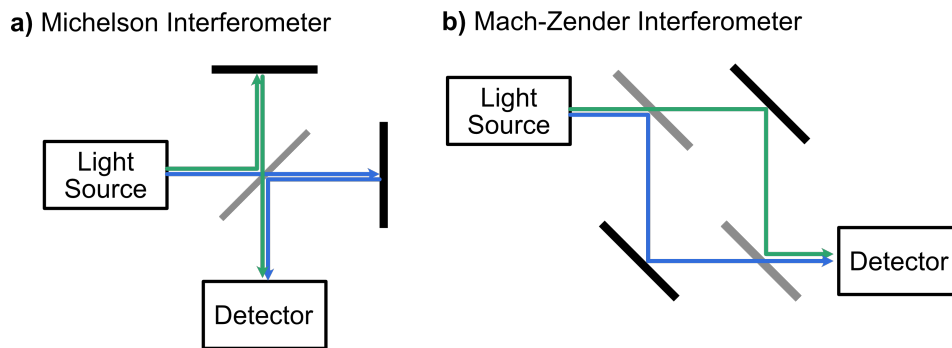


Figure 2.13: Two common interferometers include Michelson interferometers and Mach-Zender interferometers.

In both cases, light from a temporally coherent source is split into two beams (in blue and green, respectively) and then recombined to interfere at a camera. Let E_1, E_2 be the magnitude of the two beams and d_1, d_2 the distance they travel. The phase of the beam is related to $\theta = nk_0d = \frac{2\pi}{\lambda_0}nd$ where n is the refractive index of the surrounding medium. Since light travels slower in media with higher refractive indices, a related concept is optical pathlength, which is the equivalent distance the light would travel if in air. The optical pathlength $l = nd$. Let both beams travel in

the same medium. Then Eq. 2.36 simplifies to

$$I = I_1 + I_2 + 2\sqrt{I_1 I_2} \cos(nk_0(d_2 - d_1)). \quad (2.37)$$

The above provides the expression in the case of a monochromatic light source. When a broadband source is used, the temporal coherence is shorter.

$$I = I_1 + I_2 + 2\sqrt{I_1 I_2} \gamma(d_2 - d_1) \cos(nk_0(d_2 - d_1)) \quad (2.38)$$

where $\gamma(\Delta d) \in [0, 1]$ is related to the temporal coherence of the light source.

From the above equations, we can see two benefits of interferometry. Firstly, the detected signal contains a term $\cos(nk_0\Delta d)$ and converts a difference in distance to a phase or intensity difference. In this way, interferometry can be used to measure minute displacements. Secondly, the detected interference signal contains the term $\sqrt{I_1 I_2}$. In the case where the signal from the sample is weak, interference can be used to amplify the weak signal to detectable range.

Thin-Film Interference

One type of interference that is commonly seen in our day-to-day life is thin-film interference (Fig. 2.14). Thin-film interference can be observed through the colorful reflections that are seen off of soap bubbles or the anti-reflective coatings placed on eye glasses. An interesting application of thin-film interference is in using lasers to paint – the laser beam causes oxidation of the material, which creates a thin film that will make the metal appear colored due to thin-film interference [15]!

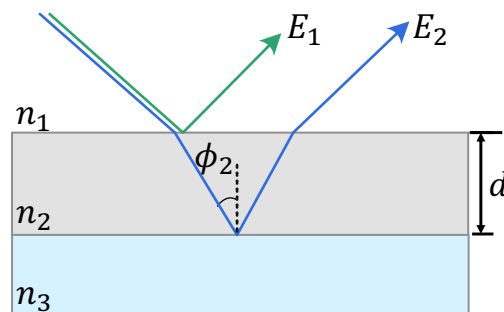


Figure 2.14: **Thin-film interference.** When light is incident upon a thin-film, the back-reflections of the light off the thin-film can interfere.

Let us consider a light beam travelling through medium n_1 that is transmitted through a thin film with thickness d and refractive index n_2 before exiting in a third medium

with refractive index n_3 (Fig. 2.14). In this case, the difference in optical pathlength between the two beams is:

$$\Delta l = 2n_2d \cos(\phi_2). \quad (2.39)$$

There can be a phase change that occurs upon reflection. When light reflects off of a medium with a higher refractive index, the reflected light has a phase shift of 180 deg or π radians. This occurs, for example, when light that is travelling in air ($n_{air} = 1$) reflects off the surface of water. In contrast, when light reflects off a medium with a lower refractive index, the reflective light does not exhibit a phase shift.

Put together, we have the following results:

1. Case $n_1 < n_2 < n_3$:

In this case, both of the reflected beams exhibit a π phase shift. Therefore, the phase difference between the two beams is

$$\Delta\theta = 2n_2d \cos(\phi_2) \frac{2\pi}{\lambda}. \quad (2.40)$$

$\Delta\theta = m(2\pi)$ for constructive interference and $\Delta\theta = m(2\pi) + \pi$ for destructive interference for $m \in \mathbb{Z}$. Therefore,

$$\cdot \text{constructive interference: } 2n_2d \cos(\phi_2) = m\lambda \quad (2.41)$$

$$\cdot \text{destructive interference: } 2n_2d \cos(\phi_2) = \left(m - \frac{1}{2}\right)\lambda. \quad (2.42)$$

2. Case $n_1 < n_2$ and $n_2 > n_3$

In this case, only the reflection off the top surface has a π phase shift, and the phase difference is

$$\Delta\theta = 2n_2d \cos(\phi_2) \frac{2\pi}{\lambda} - \pi. \quad (2.43)$$

Therefore,

$$\cdot \text{constructive interference: } 2n_2d \cos(\phi_2) = \left(m - \frac{1}{2}\right)\lambda \quad (2.44)$$

$$\cdot \text{destructive interference: } 2n_2d \cos(\phi_2) = m\lambda. \quad (2.45)$$

The interference equation depends on the wavelength λ as well as the thickness of the material d . This explains why soap bubbles appear to be colorful when shone

with white light. A white light source consists of multiple different wavelengths. The thickness of a soap bubble at a particular point as well as the angle will impact which wavelengths constructively interfere, and will therefore impact the color that is seen.

Holography

Holography is a method that utilizes interference to record the complex field of a desired wavefront. In holography, a light source is split into two beams: a sample beam and a reference beam. The sample beam interacts with the sample, whereas the reference beam is used to interfere with the sample beam. This interference provides a signal which encodes information about the sample.

In this section, we will discuss two common setups for measuring the complex field, namely phase-shifting holography and off-axis holography, as presented in Fig. 2.15. Here, $\mathbf{E}_S = E_S e^{j\theta_S}$ will refer to the complex field of the sample beam and $\mathbf{E}_R = E_R e^{j\theta_R}$ refers to the complex field of the reference beam. In many cases, the reference beam is a plane wave such that E_R is constant.

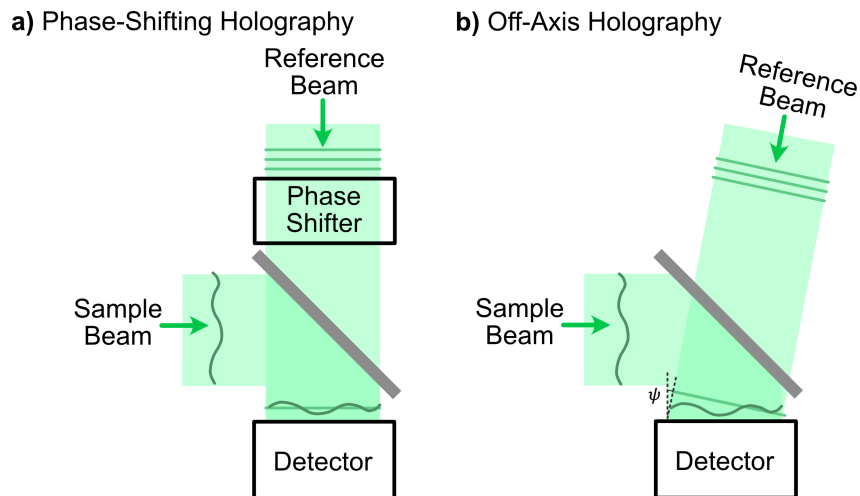


Figure 2.15: Schematic of phase-shifting and off-axis holography systems.

Phase-Shifting Holography

In phase-shifting holography, a component called a phase shifter is placed in either the sample arm or the reference arm and allows us to provide a relative phase shift of known amount between the sample and reference beam. Multiple images with different phase shifts are acquired and combined to reconstruct the complex field of the sample.

Mathematically, let the n^{th} image be

$$I_n = I_R + I_S + 2\sqrt{I_R I_S} \cos(\theta_S - \theta_R + \phi_n) \quad (2.46)$$

where $n = 0, 1, 2, 3$ and $\phi_n = \frac{2n}{N}\pi$. A minimum of $N = 3$ images is acquired to reconstruct the sample complex field. In the case where $N = 4$, the 4 images can be mathematically described as

$$\begin{aligned} I_0 &= I_R + I_S + 2\sqrt{I_R I_S} \cos(\theta_S - \theta_R + 0), \\ I_1 &= I_R + I_S + 2\sqrt{I_R I_S} \cos(\theta_S - \theta_R + \frac{\pi}{2}), \\ I_2 &= I_R + I_S + 2\sqrt{I_R I_S} \cos(\theta_S - \theta_R + \pi), \text{ and} \\ I_3 &= I_R + I_S + 2\sqrt{I_R I_S} \cos(\theta_S - \theta_R + \frac{3\pi}{2}). \end{aligned} \quad (2.47)$$

To reconstruct the sample field, we can combine these 4 images as follows:

$$\begin{aligned} (I_0 - I_2) + i(I_3 - I_1) &= 4\sqrt{I_R I_S} [\cos(\theta_S - \theta_R) + j \sin(\theta_S - \theta_R)] \\ &= 4\sqrt{I_R I_S} e^{j(\theta_S - \theta_R)}. \end{aligned} \quad (2.48)$$

Off-Axis Holography

In off-axis holography, the reference beam is tilted relative to the sample beam. Mathematically, the complex field of the reference beam can be denoted as

$$\mathbf{E}_R = E_R e^{j\theta_R} e^{jk_0(\sin(\psi_x)x + \sin(\psi_y)y)} \quad (2.49)$$

where ψ_x, ψ_y are the tilts in the x - and y - directions of the reference beam.

The interference image on the camera is

$$I = I_R + I_S + E_S E_R \left[e^{jk_0(\theta_R - \theta_S)} e^{jk_0[\sin(\psi_x)x + \sin(\psi_y)y]} + e^{-jk_0(\theta_R - \theta_S)} e^{-jk_0[\sin(\psi_x)x + \sin(\psi_y)y]} \right] \quad (2.50)$$

For notational simplicity, we will refer to the position vector as $\mathbf{r} = (x, y)$, k -space vector as $\mathbf{k} = (k_x, k_y)$, and tilt angle vector as $\boldsymbol{\psi} = (\psi_x, \psi_y)$. Let $\sin(\boldsymbol{\psi}) = (\sin(\psi_x), \sin(\psi_y))$. Then,

$$\sin(\psi_x)x + \sin(\psi_y)y = \sin(\boldsymbol{\psi}) \cdot \mathbf{r} \quad (2.51)$$

and the above interference equation can be simplified as

$$I = I_R + I_S + E_S E_R \left[e^{jk_0(\theta_R - \theta_S)} e^{jk_0 \sin(\boldsymbol{\psi}) \cdot \mathbf{r}} + e^{-jk_0(\theta_R - \theta_S)} e^{-jk_0 \sin(\boldsymbol{\psi}) \cdot \mathbf{r}} \right]. \quad (2.52)$$

For off-axis holography, the DC terms I_R and I_S are separated from the cross-terms that contain information about the complex field in the spatial Fourier domain. To determine the complex field of the sample, we can first isolate it by computing the spatial Fourier transform. This yields

$$\begin{aligned} \mathcal{F}[I] = & \mathcal{F}[I_R + I_S](\mathbf{k}) \\ & + \mathcal{F}\left[E_R E_S e^{j(\theta_R - \theta_S)}\right](\mathbf{k} + k_0 \sin(\psi)) \\ & + \mathcal{F}\left[E_R E_S e^{j(\theta_S - \theta_R)}\right](\mathbf{k} - k_0 \sin(\psi)) \end{aligned} \quad (2.53)$$

where $\mathcal{F}[\cdot]$ is the 2D spatial Fourier transform that converts from space-domain to k-space domain. The phase ramp $e^{\pm j k_0 \sin(\psi) \cdot \mathbf{r}}$ results in a shift in the k-space domain by $k_{\text{shift}} = k_0 \sin(\psi)$.

As seen from above, the spatial Fourier transform of the interference pattern contains 3 lobes: one centered at $(k_x, k_y) = (0, 0)$ that is $\mathcal{F}[I_R + I_S]$, and two side lobes centered at $\pm k_{\text{shift}}$. To reconstruct the sample field, we can crop one of the side lobes and compute the inverse Fourier transform, which will yield

$$I_{\text{result}} = E_R E_S e^{j(\theta_S - \theta_R)}. \quad (2.54)$$

Shot-Noise-Limited Detection

We wrap up this section with a discussion on shot-noise-limited detection and the advantage it provides. Interferometry enables shot-noise-limited detection which allows us to detect weak signals with high sensitivity.

There are many types of noises present in an imaging system. Some commonly considered sources of noise include detector noise, excess intensity noise, and shot noise. Let the variances of these noise sources be σ_{det}^2 , σ_{shot}^2 , and σ_{excess}^2 . Since these noise sources are independent, the total noise is:

$$\sigma_{\text{noise}}^2 = \sigma_{\text{det}}^2 + \sigma_{\text{shot}}^2 + \sigma_{\text{excess}}^2. \quad (2.55)$$

Sources of detector noise include temperature-induced fluctuations, read noise, and dark noise. Excess intensity noise arises due to fluctuations in the laser intensity and is proportional to intensity squared. Shot noise is a fundamental type of noise that is always present and arises due to the quantized nature of photons and photo-electrons. Let us consider the case where the average rate of photons impinging the detector is constant. Despite the constant rate, due to the discrete number of photons that are getting collected, the exact number of detected photo-electrons for

a given period of time T can vary. The number of detected photo-electrons follows Poisson statistics and has the property that the variance in the number detected is equal to the mean. Let the average number of photo-electrons be N . Then, in the ideal scenario, the SNR of the measurement is:

$$\text{SNR}_{\text{ideal}} = \frac{\text{signal}^2}{\text{noise variance}} = \frac{N^2}{N} = N. \quad (2.56)$$

Now we turn to the SNR of interferometry. As a reminder, the interference equation is

$$I = I_R + I_S + 2\sqrt{I_R I_S} \cos(\theta). \quad (2.57)$$

The signal term in holographic systems relates to the amplitude of the cross term and is

$$\text{signal} \propto \eta\sqrt{I_R I_S T A}, \quad (2.58)$$

where $\eta = \frac{\epsilon}{h\nu}$ is the photo-electron conversion efficiency.

To find the noise terms, we consider when $I_R \gg I_S$ and shot noise is dominated by contributions from the reference arm, such that

$$\sigma_{\text{shot}}^2 \approx \eta I_R T A. \quad (2.59)$$

Therefore, the SNR of interferometry is

$$\text{SNR}_{\text{interferometry}} \propto \frac{\eta\sqrt{I_R I_S T A}}{\sigma_{\text{det}}^2 + \sigma_{\text{shot}}^2 + \sigma_{\text{excess}}^2}. \quad (2.60)$$

In the shot-noise-limited case, I_R is adjusted such that $\sigma_{\text{shot}}^2 > \sigma_{\text{det}}^2$ and $\sigma_{\text{shot}}^2 > \sigma_{\text{excess}}^2$. In this case, $\sigma_{\text{noise}}^2 \approx \sigma_{\text{shot}}^2$, and

$$\text{SNR}_{\text{shot-noise-limited interferometry}} \propto \frac{(\eta\sqrt{I_R I_S T A})^2}{\eta I_R T A} = \eta I_S T A = N_S. \quad (2.61)$$

Therefore, shot-noise-detection allows us to perform measurements with an SNR that is comparable to the ideal, noiseless case.

BIBLIOGRAPHY

- [1] H. C. Hulst and H. C. van de Hulst, *Light scattering by small particles*. Courier Corporation, 1981.
- [2] L. V. Wang and H.-i. Wu, *Biomedical optics: principles and imaging*. John Wiley & Sons, 2012.
- [3] M. G. Giacomelli and A. Wax, “Imaging beyond the ballistic limit in coherence imaging using multiply scattered light,” *Optics express*, vol. 19, no. 5, pp. 4268–4279, 2011.
- [4] T. E. Matthews, M. G. Giacomelli, W. J. Brown, and A. Wax, “Fourier domain multispectral multiple scattering low coherence interferometry,” *Applied optics*, vol. 52, no. 34, pp. 8220–8228, 2013.
- [5] Y. Zhao, J. R. Maher, M. M. Ibrahim, J. S. Chien, H. Levinson, and A. Wax, “Deep imaging of absorption and scattering features by multispectral multiple scattering low coherence interferometry,” *Biomedical optics express*, vol. 7, no. 10, pp. 3916–3926, 2016.
- [6] J. W. Goodman, *Speckle phenomena in optics: theory and applications*. Roberts and Company Publishers, 2007.
- [7] S. Popoff, G. Lerosey, R. Carminati, M. Fink, A. Boccaro, and S. Gigan, “Measuring the transmission matrix in optics: an approach to the study and control of light propagation in disordered media,” *Physical review letters*, vol. 104, no. 10, p. 100601, 2010.
- [8] M. Mounaix, D. Andreoli, H. Defienne, G. Volpe, O. Katz, S. Grésillon, and S. Gigan, “Spatiotemporal coherent control of light through a multiple scattering medium with the multispectral transmission matrix,” *Physical review letters*, vol. 116, no. 25, p. 253901, 2016.
- [9] B. Judkewitz, R. Horstmeyer, I. M. Vellekoop, I. N. Papadopoulos, and C. Yang, “Translation correlations in anisotropically scattering media,” *Nature physics*, vol. 11, no. 8, pp. 684–689, 2015.
- [10] J. W. Goodman, *Introduction to Fourier optics*. Roberts and Company Publishers, 2005.
- [11] S. Feng, C. Kane, P. A. Lee, and A. D. Stone, “Correlations and fluctuations of coherent wave transmission through disordered media,” *Physical review letters*, vol. 61, no. 7, p. 834, 1988.

- [12] I. Freund, M. Rosenbluh, and S. Feng, “Memory effects in propagation of optical waves through disordered media,” *Physical review letters*, vol. 61, no. 20, p. 2328, 1988.
- [13] O. Katz, P. Heidmann, M. Fink, and S. Gigan, “Non-invasive single-shot imaging through scattering layers and around corners via speckle correlations,” *Nature photonics*, vol. 8, no. 10, pp. 784–790, 2014.
- [14] G. Osnabrugge, R. Horstmeyer, I. N. Papadopoulos, B. Judkewitz, and I. M. Vellekoop, “Generalized optical memory effect,” *Optica*, vol. 4, no. 8, pp. 886–892, 2017.
- [15] V. P. Veiko, Y. Andreeva, L. Van Cuong, D. Lutoshina, D. Polyakov, D. Sinev, V. Mikhailovskii, Y. R. Kolobov, and G. Odintsova, “Laser paintbrush as a tool for modern art,” *Optica*, vol. 8, no. 5, pp. 577–585, 2021.

IMAGING MOVING TARGETS THROUGH SCATTERING MEDIA

This chapter is adapted from the manuscript M. Cua, E. Zhou, and C. Yang, “Imaging moving targets through scattering media,” Optics Express 25(4): 3935-3945 (2017) DOI: 10.1364/OE.25.003935

This chapter describes a technique for performing diffraction-limited imaging through and within scattering media. Optical microscopy in complex, inhomogeneous media is challenging due to the presence of multiply scattered light, which limits the depth at which diffraction-limited imaging can be achieved. One way to circumvent the degradation in resolution is to use speckle-correlation-based imaging (SCI) techniques, which permit imaging of objects inside scattering media at diffraction-limited resolution. However, SCI methods are currently limited to imaging sparse objects in a dark-field scenario. In this work, we demonstrate the ability to image hidden objects in a bright-field scenario. The contribution of the object and background is separated using object motion. By using a deterministic phase modulator to generate a spatially incoherent light source, the background contribution can be kept constant between acquisitions and subtracted out. In this way, the signal arising from the object can be isolated, and the object can be reconstructed with high fidelity. This work is not limited to imaging bright objects in the dark-field case, but also works in bright-field scenarios, with non-emitting objects.

3.1 Introduction

Optical imaging is challenging in turbid media, where multiple scattering of light causes a degradation of resolution and limits the depths at which we can reliably image ($< 1\text{mm}$ in biological tissue) without having to resort to destructive optical clearing or sectioning techniques [1]. Many approaches currently exist to filter out the multiply scattered light and detect only the unscattered (ballistic) or minimally scattered photons. These include methods such as time and coherence gating, which separate the ballistic photons from the scattered photons based on their transit time to the detector [2, 3]; methods that rely on preserving the initial angular momentum or polarization modulation [4–7]; and methods that rely on spatial confinement, such as confocal and multi-photon microscopy [1, 8]. An issue with methods that rely on

detecting only the minimally scattered photons is the maximum achievable depth of penetration, since the chance of detecting ballistic photons decreases exponentially with increasing depth.

Instead of rejecting the scattered photons, other approaches have aimed to take advantage of the information inherent within the detected speckle field that arises from multiply scattered light. Wavefront shaping (WFS) techniques exploit the principles of time-reversal to undo the effect of scattering and enable the focusing of light in thick, scattering media [9–12]. However, WFS usually requires long acquisition times to measure the transmission matrix, and/or the presence of a guide star. On the other hand, speckle-correlation-based imaging (SCI) approaches exploit the angular correlations inherent within the scattering process to reconstruct the hidden object and do not need long acquisition times or a guide star [13, 14]. However, SCI methods are limited to working in dark-field scenarios, with sparsely-tagged objects [14], since the detected light must consist solely of light arising from the object.

In this work, we demonstrate imaging of hidden moving objects in a bright-field scenario by leveraging the temporal correlations inherent in the scattering process to separate and remove the dominating contribution from the background [15, 16]. To create a spatially incoherent light source, a spatial light modulator (SLM) was used to apply the same set of random phase patterns during different acquisitions. The use of a deterministic phase modulator ensured that the background contribution remained constant across the detected images. By removing the background component, the speckle pattern from the object was isolated, and the object was reconstructed with high fidelity. Using this technique, we experimentally demonstrate successful recovery of moving objects that would otherwise be obscured by scattering media.

3.2 Principle

Fig. 3.1 presents an overview of our system. A moving object, hidden at a distance u behind a scattering media, is illuminated using a spatially incoherent, narrow-band light source. The scattered light is detected by a high-resolution camera that is placed at a distance v from the scattering media.

In the absence of any correlations in the scattering pattern, the detected image is merely a speckle intensity field. However, by exploiting the deterministic nature of scattering, the hidden object can be recovered (Fig. 3.1C). Let us first consider the case where light is confined to emit solely within an isoplanatic range, as

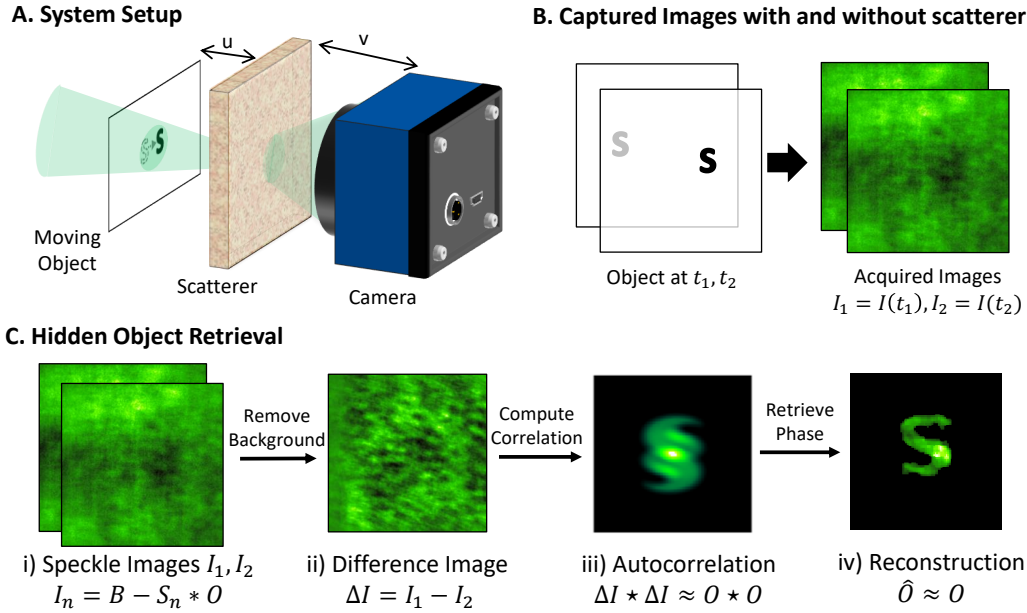


Figure 3.1: **Principle behind non-invasive imaging of obscured moving objects.**

A) A spatially incoherent light source illuminates a moving object hidden behind a visually opaque turbid media. The resultant speckle field is captured by a camera sensor. B) Speckle images are acquired by the camera sensor at different times, with the object moving between the captures. The scattering media prevents us from resolving the object. C) The hidden object can be retrieved from the seemingly random speckle images by taking advantage of inherent angular correlations in the scattering pattern. i) Each captured image I_n consists of a background, B , subtracted by the imaged object, where the imaged object is the convolution of the PSF of the scattering media, S , and the object pattern, O . ii) Although the background signal dominates over the object, it can be subtracted out by taking the difference between the two captured images ΔI . iii) The object autocorrelation $O \star O$ is approximated by autocorrelating the difference image ΔI . iv) The hidden object can be reconstructed from the object autocorrelation by using phase retrieval techniques.

defined by the angular memory effect (ME). In this case, the detected light can be mathematically represented as

$$I = S * O, \quad (3.1)$$

where S is the point spread function (PSF) of the light scattering process, or equivalently the speckle intensity distribution at the camera arising from a single point source at the object plane; and O is the object, defined as the collection of points through which light can be transmitted [14]. For this paper, we use the operator $*$ to denote convolution. The memory effect region can be approximated as $\delta x = \frac{u\lambda}{\pi L}$, where L is the thickness of the scattering media, λ is the wavelength of light, and u

is the distance between the scattering media and the object.

If we now consider the case of an absorptive object in a bright-field scenario, then the majority of the detected light arises from the background. Using superposition, the detected intensity image I can be mathematically described as

$$I = B - S * O, \quad (3.2)$$

where B is the speckle intensity image arising from the scattered light transmitted through the medium, and $S * O$ is the portion that the object would have contributed if it were transmitting, as opposed to blocking, light (Fig. 3.1c,i). Due to the dominating contribution from the background B , we cannot retrieve O from I alone. By acquiring multiple intensity images with the background, but not the object, constant between acquisitions, we can remove the background signal and thereby retrieve the object.

One strategy to achieve this is to use a moving object. If the object dimensions fall within the ME region, the contribution of the object in each image can be represented as the convolution of the object pattern with an acquisition-dependent PSF. As long as the rest of the sample is static, the speckle field arising from the background will remain unchanged and can be subtracted out by taking the difference between captures. That is,

$$I_n = B - S_n * O, n = 1, 2, \dots N \quad (3.3)$$

$$\text{and } \Delta I_n = I_{n+1} - I_n = (S_n - S_{n+1}) * O, \quad (3.4)$$

where I_n denotes the n^{th} captured image. Since the scattering PSF is a delta-correlated process ($S_n(x) \star S_n(x) \approx \delta(x)$), taking the autocorrelation (AC) of the image ΔI yields the object autocorrelation (OAC), plus additional noise terms (Fig. 3.1C,iii). That is,

$$\Delta I_n \star \Delta I_n \approx 2 \times (O \star O) - (S_n \star S_{n+1} + S_{n+1} \star S_n) * O = 2 \times (O \star O) - \text{noise}, \quad (3.5)$$

where \star denotes autocorrelation. We shall refer to $\Delta I_n \star \Delta I_n$ as the speckle autocorrelation (SAC).

The object can be recovered from the SAC by using phase retrieval techniques, such as the Fienup iterative phase retrieval methods, to recover the Fourier phase (Fig. 3.1C,iv) [17]. The resultant object will have an image size dictated by the magnification of the system, $M = -\frac{v}{u}$.

Impact of Object Travel Distance

Depending on the distance traveled by the object, the PSFs $S_n, n = 1, 2, \dots$ may or may not be correlated. Fig. 3.2 illustrates the effect of travel distance, relative to the ME range, on the SAC. The speckle intensity images I_1, I_2 were determined using simulation. For comparison, the autocorrelation of the object/target, $A = O \star O$ has also been provided (Fig. 3.2A, ‘Object AC’). For simplicity, only the case of two image captures ($n = 1, 2$) has been considered.

For a moving object, the associated PSFs S_1, S_2 will have a degree of correlation $C(\Delta \mathbf{x})$ based on the object travel distance $\Delta \mathbf{x}$. For scattering media with thicknesses L greater than the mean free path, the degree of correlation can be approximated using the angular correlation function

$$C(\Delta \mathbf{x}) = \left[\frac{k\Theta L}{\sinh(k\Theta L)} \right]^2 \quad (3.6)$$

where $k = \frac{2\pi}{\lambda}$, L is the thickness of the scattering medium, and $\Theta \approx \frac{\Delta \mathbf{x}}{u}$ [18–20]. When $C(\Delta \mathbf{x}) > 0.5$, the object is considered to have traveled within the ME field of view. The following sections describe three possible cases in more detail: $C(\Delta \mathbf{x}) \approx 1$, $C(\Delta \mathbf{x}) > 0.5$, and $C(\Delta \mathbf{x}) \rightarrow 0$.

Case 1: Object travels distance where $C(\Delta \mathbf{x}) \approx 1$

In the case where the object travels a small distance (such that $C(\Delta \mathbf{x}) \approx 1$), we have

$$S_2(\mathbf{x}_i) \approx S_1(\mathbf{x}_i + \Delta \mathbf{x}_i) \quad (3.7)$$

where $\mathbf{x} = (x, y)$, $\mathbf{x}_i = (x_i, y_i)$ are coordinates in the object plane and image plane, respectively; $\Delta \mathbf{x}$ is the distance the object traveled in the object plane; and $\Delta \mathbf{x}_i = M\Delta \mathbf{x}$. We can equivalently consider the PSF to be the same in both captures and have the object travel between captures. That is,

$$O_2 = O(\mathbf{x}_i + \Delta \mathbf{x}_i), \quad (3.8)$$

$$\Delta I = S * [O(\mathbf{x}_i) - O(\mathbf{x}_i + \Delta \mathbf{x}_i)], \quad (3.9)$$

$$\text{and } \Delta I \star \Delta I = 2A(\mathbf{x}_i) - A(\mathbf{x}_i + \Delta \mathbf{x}_i) - A(\mathbf{x}_i - \Delta \mathbf{x}_i), \quad (3.10)$$

where $A = O \star O$ is the object autocorrelation (OAC). The SAC contains three copies of the OAC: a positive copy centered at $\mathbf{x} = (0, 0)$, and two negative copies shifted by an amount commensurate with the object travel distance (Fig. 3.2B, ‘Speckle AC’).

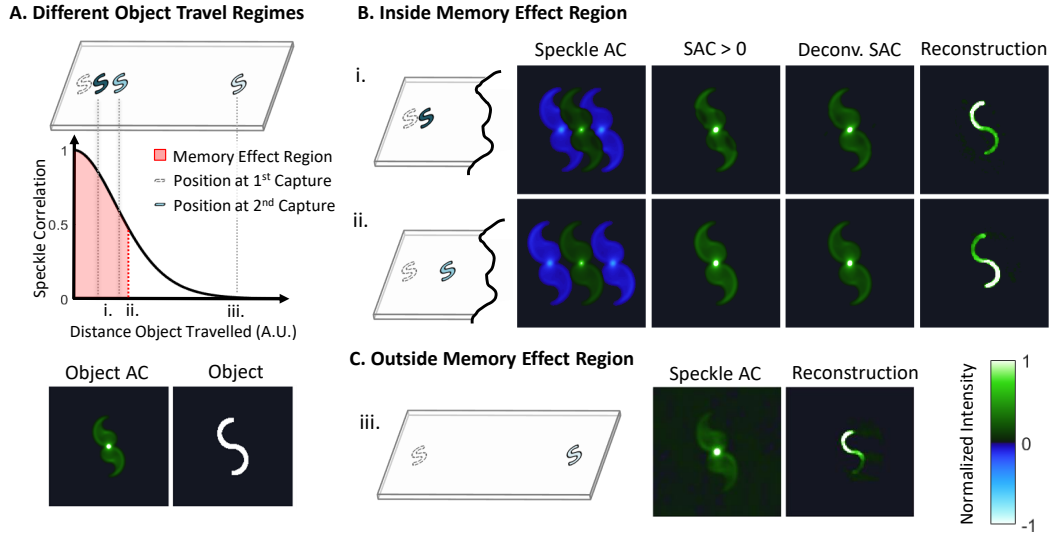


Figure 3.2: Impact of object travel distance on the computed speckle autocorrelation (SAC). A) The scattering PSFs experienced by an object have a degree of correlation $C(\Delta\mathbf{x})$ that depends on the distance the object traveled. When $C(\Delta\mathbf{x}) \geq 0.5$ (shown in red), the object is considered to have traveled within the memory effect (ME) region. For comparison, the object and its autocorrelation (AC) are displayed. B) When the object travels inside the ME region, the SAC contains three copies of the object autocorrelation (OAC): a centered, positive copy and two negative copies shifted by an amount proportional to the object travel distance. The OAC can be determined by either deconvolving the SAC or by thresholding out the negative portions (negative with reference to the mean, background level). The object can be reconstructed from the estimated OAC using phase retrieval techniques. C) When the object travels a distance where $C(\Delta\mathbf{x}) \approx 0$, only a single copy of the OAC is seen, with additional noise from the cross-correlation between uncorrelated PSFs. The normalized colormap used to display the AC and reconstructed object has been provided, with 0 corresponding to the mean background level.

Since $C(\Delta\mathbf{x}) \approx 1$ when $\Delta\mathbf{x} \approx 0$, the object may travel a distance shorter than the extent of its autocorrelation. In this case, the SAC will yield positive and negative copies of the OAC that overlap (Fig. 3.2i). The OAC can be recovered using deconvolution (Fig. 3.2i, ‘Deconv. SAC.’). Using thresholding to remove the negative portions will adversely impact the positive copy and result in an incomplete estimation of the OAC (Fig. 3.2i, ‘SAC>0’). For the results presented in Fig. 3.2, the objects were reconstructed by applying an iterative phase retrieval algorithm on the deconvolved SAC ([13, 14, 17]).

Case 2: Object travels distance where $C(\Delta\mathbf{x}) > 0.5$

In the regime where the object travels within the angular ME range ($C(\Delta\mathbf{x}) > 0.5$), S_1 and S_2 are correlated. To highlight the impact of the degree of correlation $C(\Delta\mathbf{x})$ on the SAC, we can mathematically represent S_2 as:

$$S_2 = C(\Delta\mathbf{x})S_1(\mathbf{x}_i + \Delta\mathbf{x}_i) + \sqrt{1 - [C(\Delta\mathbf{x})]^2}S, \quad (3.11)$$

where S is a speckle intensity pattern that is uncorrelated with S_1 . The scatter PSFs in the equation above are mean-subtracted speckle intensities. Representing S_2 in the form above allows us to preserve speckle intensity statistics (that is, the speckle intensity variance and mean satisfy $\mathbb{V}[S_1] = \mathbb{V}[S_2]$ and $\mathbb{E}[S_1] = \mathbb{E}[S_2]$, respectively.)

Using Eq. (3.11), Eqs. (3.4) and (3.5) become

$$\Delta I = \left(S_1 - C(\Delta\mathbf{x})S_1(\mathbf{x}_i + \Delta\mathbf{x}_i) - \sqrt{1 - [C(\Delta\mathbf{x})]^2}S \right) * O \quad (3.12)$$

$$\text{and } \Delta I \star \Delta I \approx 2A(\mathbf{x}_i) - C(\Delta\mathbf{x})A(\mathbf{x}_i \pm \Delta\mathbf{x}_i) + \sqrt{1 - [C(\Delta\mathbf{x})]^2} \times \text{noise}, \quad (3.13)$$

where the last equation follows from noting that the speckle fields are a delta-correlated process and that the cross-correlation of two uncorrelated speckle intensities yields noise.

The SAC still contains three copies of the OAC. However, the ratio of the intensity of the positive and negative OAC copies is determined by the ME correlation function $C(\Delta\mathbf{x})$. Moreover, since $S_2 \neq S_1$, there is an additional noise term that increases with decreasing $C(\Delta\mathbf{x})$. Since there is no overlap between the positive and negative OAC copies, the OAC can be retrieved by either thresholding out the portions of the SAC that are smaller than the background value (Fig. 3.2ii, ‘SAC>0’), or by deconvolving the image (Fig. 3.2ii, ‘Deconv. SAC.’). Appendix 1 provides more details on the deconvolution algorithm.

Case 3: Object travels distance where $C(\Delta\mathbf{x}) \approx 0$

In the case where the object travels outside the memory effect region between captures, S_1 and S_2 are uncorrelated, and Eq. (3.13) can be simplified to Eq. (3.5). Comparing the SAC in Fig. 3.2iii with those in Fig. 3.2i-ii, we see that the SAC in the case where the object travels farther than the ME region exhibits more noise. This is expected due to the additional noise term caused by $S_1 \star S_2$ that is not present in Case 1.

From above, in all cases (for $C(\Delta\mathbf{x}) \in [0, 1)$), we can successfully retrieve the object autocorrelation from the acquired speckle images, S_1, S_2 . From the estimated OAC, phase retrieval techniques can then be applied to reconstruct the object at diffraction-limited resolution.

Retrieving the Object Autocorrelation through Deconvolution

To deconvolve the computed autocorrelation, Weiner deconvolution was applied to reduce the deconvolution noise. We briefly describe the process here. We can rewrite Eq. 3.13 as

$$g = \Delta I \star \Delta I \approx A * h + n = y + n \quad (3.14)$$

$$\text{where } h(\mathbf{x}_i) = 2\delta(\mathbf{x}_i) - C(\Delta\mathbf{x})\delta(\mathbf{x}_i \pm \Delta\mathbf{x}_i) \quad (3.15)$$

and n is the noise term. In this case, Weiner deconvolution estimates A by applying

$$\mathcal{F}(A) = \mathcal{F}(g) \frac{\mathcal{F}(h)}{|\mathcal{F}(h)|^2 + k} \approx \frac{\mathcal{F}(y)}{\mathcal{F}(h)} \quad (3.16)$$

where \mathcal{F} is the Fourier transform operator, and $k = \frac{\mathcal{F}(n)}{\mathcal{F}(g)} \approx \frac{1}{SNR}$ estimates the SNR level of your signal [21]. Since all object ACs have a peak value of $A(\mathbf{x}_i = (0, 0)) = \sum_{\mathbf{x}} O^2$, to determine h from the computed autocorrelation, we estimated the value of $C(\Delta\mathbf{x}_i)$ by taking the negative/positive peak values in the negative/positive AC copies. The locations of the negative peaks, with respect to the centered, positive peak, provided the value of the shift $\Delta\mathbf{x}_i$.

3.3 Results

For the experimental demonstration, a laser light beam (CrystalLaser CS532-150-S; $\lambda = 532$ nm) was expanded ($1/e^2$ diameter of 20 cm) and reflected off a phase-only spatial light modulator (SLM; Holoeye PLUTO-VIS) to generate a spatially incoherent light source (Fig. 3.3).

An SLM was used in place of a rotating diffuser in order to generate a deterministic, temporally variant set of 50 to 100 random phase patterns. This set of patterns was used for all the acquisitions to ensure that the background light captured remained constant. The object and camera (pco.edge 5.5, PCO-Tech, USA) were placed at a distance $u = 20 - 30$ cm and $v = 10 - 15$ cm from the scattering media (DG10-120 diffuser; Thorlabs, USA) (Fig. 3.3).

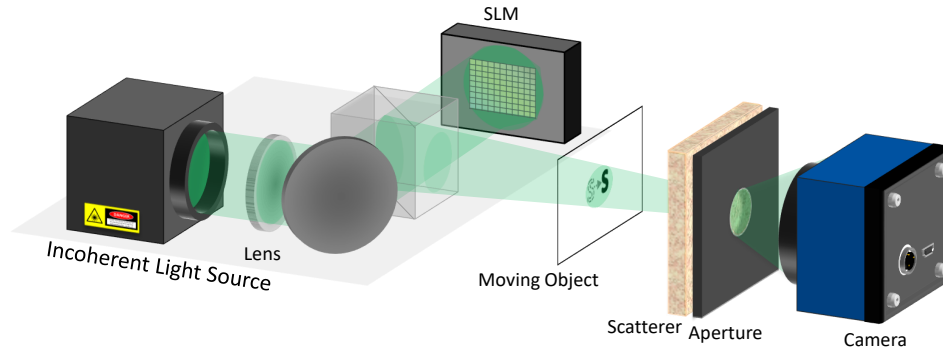


Figure 3.3: **Experimental setup for imaging hidden moving objects.** A spatially incoherent source is generated by reflecting an expanded laser beam ($\lambda = 532$ nm; $1/e^2$ diameter of 20 cm) off a spatial light modulator (SLM), which applies a temporally varying set of random phase patterns. The light source is transmitted through the moving object and scattered by the turbid media. The emitted scattered light is collected by a camera. An aperture controls the final object resolution and the speckle size at the camera. Lens focal length = 400 mm.

To ensure that only the object moved between successive image captures, a transmissive SLM (tSLM; Holoeye LC2002 with polarizer) coupled with a polarizer (Thorlabs, LPVISE200-A) was used for amplitude modulation, and served as the object (Fig. 3.4). For each object, a set of $n=4$ images, I_1, \dots, I_4 were acquired, with the object moving 1.5mm between each acquisition. The raw camera images (Fig. 3.4b) display a seemingly random light pattern that is similar for different objects. This is due to the dominant contribution of the background.

From each successive pair of acquired images, the OAC (Fig. 3.4d) was estimated by deconvolving the SAC. The deconvolved SAC images were then averaged to reduce noise and yield a better estimate of the OAC. A Fienup-type iterative phase retrieval method was applied to reconstruct the hidden object with high fidelity (Fig. 3.4e) [13, 14, 17]. One modification that was made to the algorithm was to add an object support to the object constraints; this object support was determined from the OAC support [22, 23]. In all cases, the obscured object was successfully reconstructed (Fig. 3.4e).

To experimentally demonstrate the effect of object travel distance, we moved an object a distance of 0.5, 1, and 3 mm between image acquisitions, and looked at the corresponding SAC and reconstructed object (Fig. 3.5). As expected, the SAC contained three copies of the OAC. We also compared the effect of processing the SAC using deconvolution (Fig. 3.5b) vs. thresholding (Fig. 3.5c).

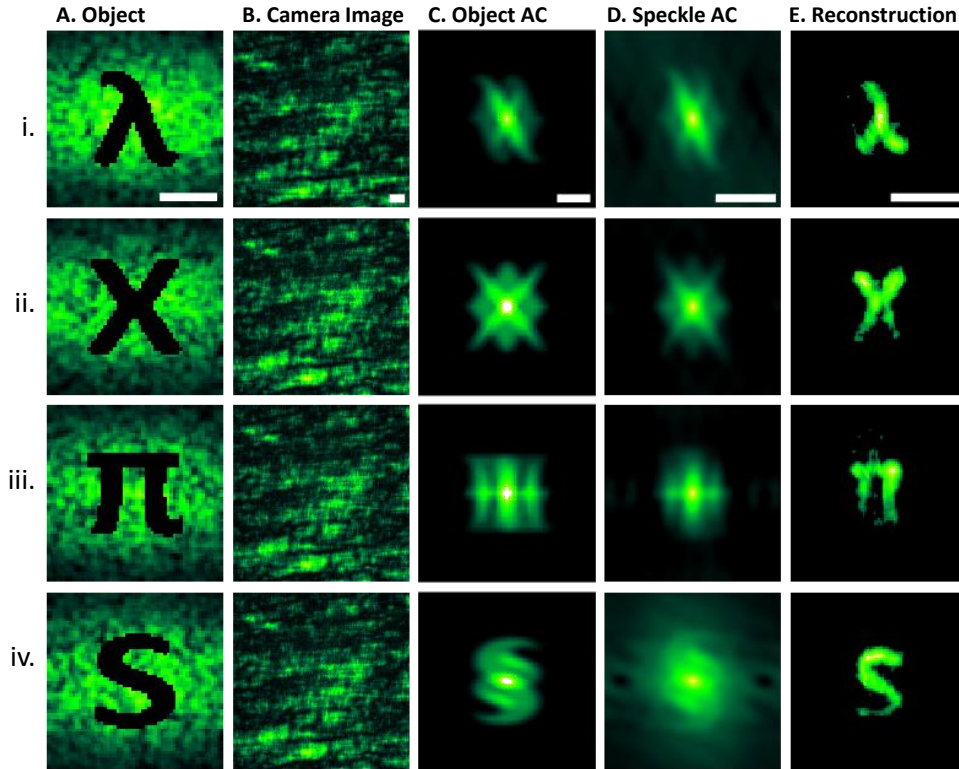


Figure 3.4: **Experimental demonstration of imaging of moving targets hidden behind a diffuser.** A) The ‘object’ is hidden behind a scattering medium and attenuates light transmission. The object was moved 1.5 mm between acquisitions. B) Due to the presence of the scattering medium, the object is obscured, and the camera image I_1 is dominated by the scattered light from the background. C) The ideal object autocorrelation (AC). D) The speckle autocorrelation $\Delta I \star \Delta I \approx O \star O$. E) By applying phase retrieval on the speckle autocorrelation, the hidden object was reconstructed with high fidelity. Scale bar = 500 μm .

For Case i, the object traveled a distance $\Delta \mathbf{x} < \delta \mathbf{x}$, and both the object and SAC overlapped in space between successive acquisitions. In the case of object overlap, only the non-overlapping portion of the object can be retrieved (Fig. 3.5i). Comparing the result of deconvolution vs thresholding, the reconstructed image from the deconvolved SAC more closely resembles the original object [Fig. 3.5i,b). However, in both cases, what we are left with is an incomplete OAC and reconstructed object.

For Case ii, the object traveled a distance $\delta \mathbf{x} < \Delta \mathbf{x} \leq 2\delta \mathbf{x}$. Since the OAC support is approximately twice the object support, the positive and negative copies of the OAC overlapped (Fig. 3.5ii) [22]. Due to the overlap, thresholding resulted in an imperfect object reconstruction (Fig. 3.5ii,c). In contrast, by deconvolving, the signal from the negative copies can be used to gain a better estimate of the OAC, from which

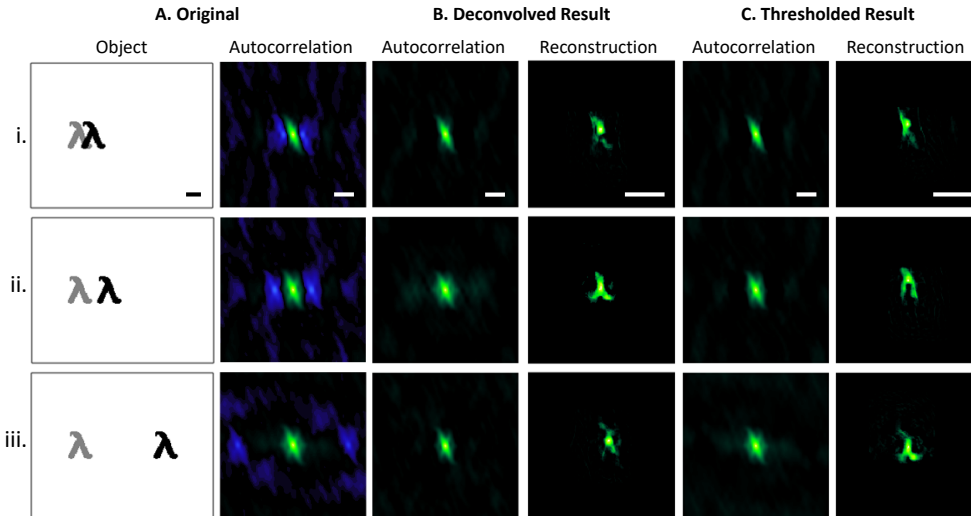


Figure 3.5: **Experimental results showing the impact of object travel distance on the speckle autocorrelation (SAC) and object reconstruction.** A) A diagram showing the position and shape of the object at both time captures, and the SAC, showing three shifted copies of the object autocorrelation (OAC). The effect of applying B) deconvolution and C) thresholding to retain the positive portion (with respect to the mean level) for estimating the OAC from the SAC was compared in three cases (i-iii). The hidden object was reconstructed by applying Fienup phase retrieval on the estimated OAC. Colormap: green is positive, blue is negative (with respect to the mean value, in black). Scale bar: $500 \mu\text{m}$.

the object can be reconstructed (Fig. 3.5ii,b).

For Case iii, the object traveled a distance $\Delta\mathbf{x} \gg 2\delta\mathbf{x}$, and there was no overlap in the SAC. Due to the large $\Delta\mathbf{x}$, $C(\Delta\mathbf{x})$ decreased, and correspondingly, the noise increased. Since the signal-to-noise ratio (SNR) of the negative copies decreased, the entire OAC cannot be seen in the negative copies (Fig. 3.5iii,a); thus, performing a deconvolution results in a noisy, imperfect OAC (Fig. 3.5iii,b), and it is more advisable to use thresholding to retain only the positive portion of the SAC (Fig. 3.5iii,c). If we compare the reconstructed objects in both cases, we see that the object from the thresholded result more closely resembles the original object.

Imaging Moving Objects Hidden Between Scattering Media

To further demonstrate our imaging technique, we placed a moving object between two diffusers (Newport 10° Light Shaping Diffuser, Thorlabs DG10-220-MD) (Fig. 3.6A). A moving object (a bent black wire) was flipped in and out of the light path between image captures, such that $I_2 = B$. We blocked the partially-developed

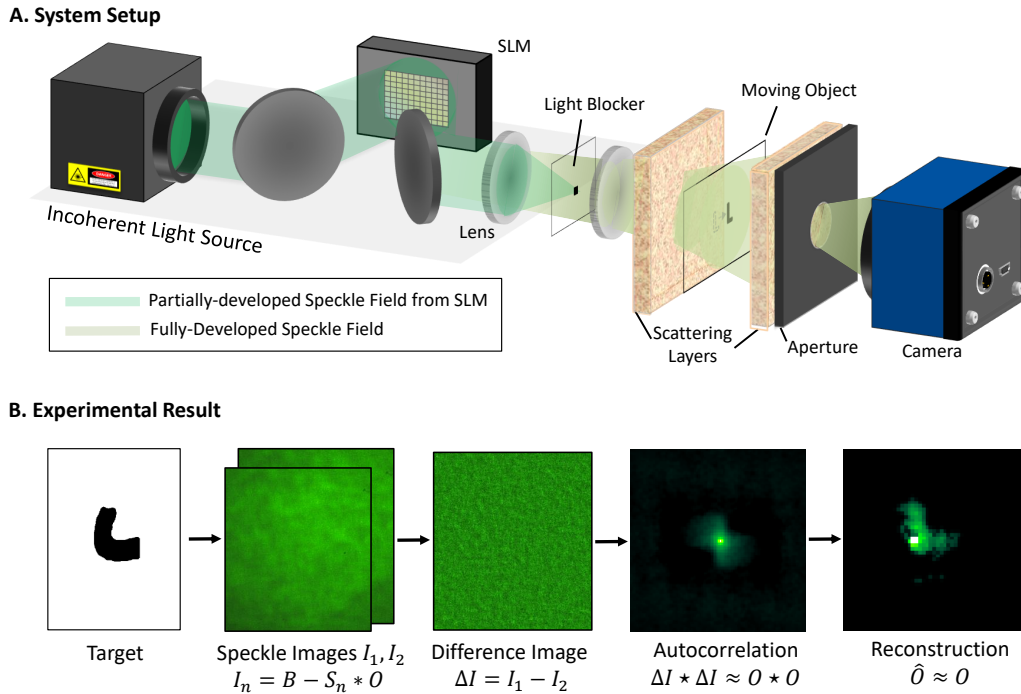


Figure 3.6: Experimental retrieval of moving targets hidden within a scattering object. A) Schematic of the experimental setup. A spatially incoherent light source is generated by reflecting an expanded laser beam off a spatial light modulator (SLM) that applied a temporally variant random phase pattern. The partially developed speckle field component is blocked, and only the fully-developed speckle field transmits through the moving object and two scattering layers. The emitted scattered light is collected by a camera. An aperture controls the resolution and the speckle size at the camera. B) Experimental result of a moving target. Two speckle intensity images , I_1, I_2 , were captured, with the target present for the first capture, and absent for the second. The background halo from I_1 and I_2 were removed prior to computing the difference $\Delta I = I_2 - I_1 \approx S_1 * O$. The speckle autocorrelation yielded an estimate of the object autocorrelation, from which the target was retrieved by applying Fienup phase retrieval. Lens focal length = 400 mm.

speckle field (from the propagation of the SLM phase pattern) and used only the fully-developed speckle pattern [24]. This fully-developed speckled pattern was transmitted through both scattering media and the moving object. The emitted scattered light was detected by a camera.

The background halo from each detected speckle intensity image was estimated and removed by performing Gaussian filtering (500x500 kernel, $\sigma = 100$), and then dividing each image by the background halo [14]. The SAC was then computed to estimate the OAC, from which phase retrieval was applied to reconstruct the hidden

object. Although the object is fully obscured from both sides by scattering media and cannot be resolved from the camera image alone, using our technique, we were able to successfully reconstruct the hidden object with high fidelity (Fig. 3.6B).

3.4 Discussion

In this paper, we demonstrated successful reconstruction of moving targets that were hidden behind an optically turbid media. Although the angular memory effect has already been used to demonstrate imaging of hidden targets, to the best of our knowledge, these prior systems were limited to imaging dark-field, sparsely-tagged objects [13, 14, 25]. We extended this work to imaging in the bright-field scenario by exploiting the temporal correlations inherent in the scattering process to remove the dominating contribution from the background and isolate the signal arising from the object [15, 16]. Although we demonstrated our results on non-emitting objects in the bright-field scenario, our technique works equally well with transmissive or reflective objects. A cursory examination reveals that, when $I_n = B + S_n * O$ and $\Delta I = I_n - I_{n+1}$, the speckle autocorrelation is still given by Eq. (3.5), similar to imaging absorptive objects in the bright-field scenario. In the remainder of this section, we discuss some of the factors that impact system performance.

Firstly, our method depends on the angular correlations inherent in the scattering process. Thus, the object dimension should fall within the angular memory effect field of view (FOV), approximated using the full-width-half-maximum (FWHM) of the correlation function, $\frac{u\lambda}{\pi L}$. The axial extent of the object, δz , should also fall within the axial decorrelation length $\frac{2\lambda}{\pi} \left(\frac{u}{D}\right)^2$ [26]. Since the ME FOV is inversely proportional to L , our technique works best with thin scattering media, or through more anisotropically scattering media, since anisotropy enhances the angular memory effect range [20]. Strongly anisotropic media, such as biological tissue, also exhibit the translational memory effect, which may be exploited to further the fidelity of imaging through scattering layers [27].

Secondly, to maximize SNR and minimize overlap, the object travel distance should be such that $\delta x < \Delta x$ and $C(\Delta \mathbf{x}) \geq 0.5$, since smaller values of $C(\Delta \mathbf{x})$ results in higher levels of noise. However, if the object moves such a large distance as to not fall within the laser light beam, then $I_2 = B$, and $\Delta I = S_1 * O$, and we can also retrieve the object with high fidelity. In all these cases, successful retrieval of the object is dependent on the background light pattern remaining constant between successive image captures. Thus, the illuminated portion of the tissue should remain constant

between image captures, and the time between image captures should fall well within the temporal decorrelation time of the scattering sample. For biological samples, the temporal decorrelation time is related to the motion of scatterers embedded within [28].

Imaging through biological samples can be achieved using a faster system. The imaging speed in our current design was limited by the refresh rate of the SLM (≈ 8 Hz) and by the exposure time required to capture an image (50-200ms). With a more powerful laser, or a faster deterministic random phase modulator, it would be possible to shorten our imaging time, and extend our work to imaging within non-static samples, such as biological tissue.

A third factor in the fidelity of the reconstruction is the complexity of the object and the size of the background relative to the object. The dynamic range of the camera should be large enough to resolve the equivalent speckle signal from the object. Since the signal contrast is inversely related to the object complexity [14], the dynamic range of the camera limits the maximum object complexity. To maximize the SNR, the camera exposure and laser power should be adjusted such that the full well depth of the camera is utilized. A camera with a larger well depth and dynamic range would provide higher SNR and the capability to image more complex objects. The diameter of the aperture in the system can be adjusted to fine-tune the image resolution and control the object complexity.

Lastly, each speckle grain at the camera should satisfy the Nyquist sampling criterion and be easily resolvable. At the same time, the number of speckle grains that are captured in each image should also be maximized in order to maximize SNR. Although the scattering PSFs are ideally a delta-correlated process, in practice, we are only sampling a finite extent of the PSF. Thus, the PSF autocorrelation yields a delta function plus some background noise which can be minimized by increasing the number of captured speckle grains [14]. Due to Nyquist requirements, the maximum number of speckle grains is a function of the camera resolution; thus, a high resolution camera would provide lower noise. Another method to reduce this speckle noise is to take multiple acquisitions and compute the average of the speckle autocorrelation images.

3.5 Conclusion

In conclusion, we demonstrated successful imaging of hidden moving targets through scattering samples. The temporal and angular correlations inherent in the scattered

light pattern allowed us to reconstruct the hidden object in cases where multiply scattered light dominates over ballistic light. This paper presented a first proof of concept. Although we demonstrated imaging of binary-amplitude targets, our system can also be extended to imaging gray-scale targets [29]. Since our imaging technique utilizes the angular memory effect, it is scalable. Moreover, our method does not require access inside the scattering media, and can therefore be used as a black box imaging system. With appropriate optimization, this opens up potential for use in applications involving the tracking of moving object in turbulent atmospheres, such as fog or underwater.

Appendix 1 – Object Complexity and SNR

In this section, we analyze the relation between the object complexity, full well depth, and signal-to-noise ratio. Let us consider the light beam incident upon the object plane. Let the area the light beam covers be denoted $a = N\delta_x$, where δ_x is the area of a resolution cell area (RCA). Let N_o be the number of RCAs the object occupies; then the number of light-emitting RCAs from the background is $N_b = N - N_o$. The detected image intensity, $I = B - S * O$, is composed of N_b speckle patterns and will have a mean and standard deviation $\mu_b \propto N_b$ and $\sigma_b \propto \sqrt{N_b}$, respectively. The signal from the object, $S * O$ is composed of the sum of N_o speckle intensities, and will have a mean and standard deviation of $\mu_o \propto N_o$ and $\sigma_o \propto \sqrt{N_o}$. Since the object signal is carried by the background light, we need $\mu_b > \mu_o \implies N_b > N_o$ (1).

N_b and N_o are also limited by the specifications of the camera. Let F denote the full well depth, η the quantum efficiency of the detector, and b denote the number of quantization bits in the analog-to-digital converter. For ease of discussion, let the mean detected speckle intensity arising from a single RCA be $\eta\mathbb{E}[S] = 1$. Since each image we captured has a mean intensity of $\mu_B = N_b$, we need $N_b \leq F$ in order to prevent saturation. Since the majority of the information about the object comes from the fluctuations in the speckle pattern, we can approximate the magnitude of the signal to be σ_o . Thus, in order to resolve the object signal, we have the requirement that $\frac{\sigma_o}{\mu_o} = \frac{1}{\sqrt{N_o}} > \frac{F}{2^b}$ (2). However, at the same time, increasing image complexity, N_o , decreases signal contrast, since $C \doteq \frac{\sigma_o}{\mu_o} = \frac{1}{\sqrt{N_o}}$.

Let us now consider the effect of shot noise. Each detected image can be mathematically represented as $I_i = B - S_i * O + n_i$ where n is the shot noise. The detected shot noise would have a mean and standard deviation of $\mu_{SN} = \eta\mathbb{E}[I] = N_b$ and

$\sigma_{SN} = \sqrt{\eta \mathbb{E}[I]} = \sqrt{N_b}$. For each detected image, the relative signal magnitude is $C = \frac{1}{\sqrt{N_o}} > \frac{\sigma_{SN}}{\mu_{SN}} = \frac{1}{\sqrt{N_b}}$ which leads to $N_b > N_o$ (3). For each detected image, the limit on the shot noise is when $\mu_{SN} = N_b \approx F$, in which case we would need $\frac{1}{\sqrt{N_o}} > \frac{1}{\sqrt{F}}$, or $F > N_o$. Thus, we have the requirement that $F \geq N_b > N_o$ (2). This, in conjunction with (1), shows that the full well depth and number of quantization bits of the camera are the ultimate limiting factors on the allowable object complexity.

This analysis only includes the effect of shot noise, and not any other sources of noise, such as decorrelation noise. From the above analysis, we have the object signal contrast, $C = \frac{1}{\sqrt{N_o}}$. In order to successfully retrieve more complex objects, we need to decrease other sources of noise as much as possible.

BIBLIOGRAPHY

- [1] V. Ntziachristos, “Going deeper than microscopy: the optical imaging frontier in biology,” *Nature Methods*, vol. 7, no. 8, pp. 603–614, 2010.
- [2] D. Huang, E. A. Swanson, C. P. Lin, J. S. Schuman, W. G. Stinson, W. Chang, M. R. Hee, T. Flotte, K. Gregory, C. A. Puliafito, and J. G. Fujimoto, “Optical coherence tomography,” *Science*, vol. 254, no. 5035, p. 1178, 1991.
- [3] S. Andersson-Engels, O. Jarlman, R. Berg, and S. Svanberg, “Time-resolved transillumination for medical diagnostics,” *Optics Letters*, vol. 15, no. 21, pp. 1179–1181, 1990.
- [4] G. H. Chapman, M. Trinh, N. Pfeiffer, G. Chu, and D. Lee, “Angular domain imaging of objects within highly scattering media using silicon micromachined collimating arrays,” *IEEE Journal of Selected Topics in Quantum Electronics*, vol. 9, no. 2, pp. 257–266, 2003.
- [5] S. Kang, S. Jeong, W. Choi, H. Ko, T. D. Yang, J. H. Joo, J.-S. Lee, Y.-S. Lim, Q.-H. Park, and W. Choi, “Imaging deep within a scattering medium using collective accumulation of single-scattered waves,” *Nature Photonics*, vol. 9, no. 4, pp. 253–258, 2015.
- [6] H. Ramachandran and A. Narayanan, “Two-dimensional imaging through turbid media using a continuous wave light source,” *Optics Communications*, vol. 154, no. 5, pp. 255–260, 1998.
- [7] S. Sudarsanam, J. Mathew, S. Panigrahi, J. Fade, M. Alouini, and H. Ramachandran, “Real-time imaging through strongly scattering media: seeing through turbid media, instantly,” *Scientific Reports*, vol. 6, 2016.
- [8] F. Helmchen and W. Denk, “Deep tissue two-photon microscopy,” *Nature Methods*, vol. 2, no. 12, pp. 932–940, 2005.
- [9] A. P. Mosk, A. Lagendijk, G. Lerosey, and M. Fink, “Controlling waves in space and time for imaging and focusing in complex media,” *Nature Photonics*, vol. 6, no. 5, pp. 283–292, 2012.
- [10] I. M. Vellekoop and A. Mosk, “Focusing coherent light through opaque strongly scattering media,” *Optics Letters*, vol. 32, no. 16, pp. 2309–2311, 2007.
- [11] X. Xu, H. Liu, and L. V. Wang, “Time-reversed ultrasonically encoded optical focusing into scattering media,” *Nature Photonics*, vol. 5, no. 3, pp. 154–157, 2011.

- [12] Y. M. Wang, B. Judkewitz, C. A. DiMarzio, and C. Yang, “Deep-tissue focal fluorescence imaging with digitally time-reversed ultrasound-encoded light,” *Nature Communications*, vol. 3, p. 928, 2012.
- [13] J. Bertolotti, E. G. van Putten, C. Blum, A. Lagendijk, W. L. Vos, and A. P. Mosk, “Non-invasive imaging through opaque scattering layers,” *Nature*, vol. 491, no. 7423, pp. 232–234, 2012.
- [14] O. Katz, P. Heidmann, M. Fink, and S. Gigan, “Non-invasive single-shot imaging through scattering layers and around corners via speckle correlations,” *Nature Photonics*, vol. 8, no. 10, pp. 784–790, 2014.
- [15] E. H. Zhou, H. Ruan, C. Yang, and B. Judkewitz, “Focusing on moving targets through scattering samples,” *Optica*, vol. 1, no. 4, pp. 227–232, 2014.
- [16] C. Ma, X. Xu, Y. Liu, and L. V. Wang, “Time-reversed adapted-perturbation (trap) optical focusing onto dynamic objects inside scattering media,” *Nature Photonics*, vol. 8, no. 12, pp. 931–936, 2014.
- [17] J. R. Fienup, “Phase retrieval algorithms: a comparison,” *Applied Optics*, vol. 21, no. 15, pp. 2758–2769, 1982.
- [18] S. Feng, C. Kane, P. A. Lee, and A. D. Stone, “Correlations and fluctuations of coherent wave transmission through disordered media,” *Physical Review Letters*, vol. 61, no. 7, p. 834, 1988.
- [19] R. Berkovits, M. Kaveh, and S. Feng, “Memory effect of waves in disordered systems: a real-space approach,” *Physical Review B*, vol. 40, no. 1, p. 737, 1989.
- [20] S. Schott, J. Bertolotti, J.-F. Léger, L. Bourdieu, and S. Gigan, “Characterization of the angular memory effect of scattered light in biological tissues,” *Optics Express*, vol. 23, no. 10, pp. 13505–13516, 2015.
- [21] R. C. Gonzalez and R. E. Woods, *Digital Image Processing (3rd Edition)*. Prentice-Hall, Inc., 2006.
- [22] J. R. Fienup, T. Crimmins, and W. Holsztynski, “Reconstruction of the support of an object from the support of its autocorrelation,” *JOSA*, vol. 72, no. 5, pp. 610–624, 1982.
- [23] J. Fienup and C. Wackerman, “Phase-retrieval stagnation problems and solutions,” *JOSA A*, vol. 3, no. 11, pp. 1897–1907, 1986.
- [24] B. Ruffing and J. Fleischer, “Spectral correlation of partially or fully developed speckle patterns generated by rough surfaces,” *JOSA A*, vol. 2, no. 10, pp. 1637–1643, 1985.

- [25] O. Katz, E. Small, and Y. Silberberg, “Looking around corners and through thin turbid layers in real time with scattered incoherent light,” *Nature Photonics*, vol. 6, no. 8, pp. 549–553, 2012.
- [26] I. Freund, “Looking through walls and around corners,” *Physica A: Statistical Mechanics and its Applications*, vol. 168, no. 1, pp. 49–65, 1990.
- [27] B. Judkewitz, R. Horstmeyer, I. M. Vellekoop, I. N. Papadopoulos, and C. Yang, “Translation correlations in anisotropically scattering media,” *Nature Physics*, vol. 11, no. 8, pp. 684–689, 2015.
- [28] J. Brake, M. Jang, and C. Yang, “Analyzing the relationship between decorrelation time and tissue thickness in acute rat brain slices using multispeckle diffusing wave spectroscopy,” *JOSA A*, vol. 33, no. 2, pp. 270–275, 2016.
- [29] H. Li, T. Wu, J. Liu, C. Gong, and X. Shao, “Simulation and experimental verification for imaging of gray-scale objects through scattering layers,” *Applied Optics*, vol. 55, no. 34, pp. 9731–9737, 2016.

*Chapter 4***SPECKLE-RESOLVED OPTICAL COHERENCE
TOMOGRAPHY**

This chapter contains unpublished text from a manuscript in preparation.

The previous chapter described a technique for performing imaging through scattering media with diffraction-limited resolution by exploiting angular and temporal correlations in the scattering process to ‘unscramble’ the scattered light information. However, such a technique required the optical memory effect and is therefore limited to specific scenarios. It also relies on computational techniques to recover the hidden object.

In this chapter, we investigate optical scattering in highly anisotropic media, where the scattering is more forward directed. In this case, the weakly-scattered ‘snake’ photons that are predominantly forward scattered provides information about the sample with moderate resolution. Here, we present a method, termed Speckle-Resolved Optical Coherence Tomography (srOCT), that efficiently detects the back-scattered light from the sample to enable imaging deeper in scattering media. We first investigate whether these snake photons exit the tissue at closer distances and shallower angles in comparison to the more strongly-scattered diffuse photons, and if so, whether spatial filtering, angular filtering, or a combination of both, is best for preferentially detecting these snake photons and improving imaging resolution. We also introduce the concept of speckle-resolved detection and demonstrate that it is an effective method for coherently detecting the multiply back-scattered light from the sample. These two concepts – spatio-angular filtering and speckle-resolved detection – are combined into a proof-of-concept system, called Speckle-Resolved Optical Coherence Tomography (srOCT). Using srOCT, we demonstrate imaging beyond the ballistic limit, up to a depth of 90 MFPs in $g = 0.96$ scattering phantoms and 4.5 mm in a biological tissue. Such a technique can be useful for imaging deeper in scattering media where mesoscopic resolution (on the order of hundreds of micrometers) is satisfactory, such as imaging and locating peripheral veins for phlebotomy and sclerotherapy.

4.1 Introduction

Light scattering poses a challenge for optical imaging through turbid media as it degrades image quality and enforces a trade-off between resolution and penetration depth. Ballistic imaging methods, such as confocal microscopy and Optical Coherence Tomography (OCT), aim to detect the singly-back-scattered, ballistic light through the use of gating methods such as time gating, polarization gating, and confocal gating [1]. These methods provide diffraction-limited resolution but have limited penetration depth, since ballistic light attenuates exponentially with depth. The limit is approximately 1-2 mean free paths for confocal microscopy and 27 round-trip mean free paths (MFPs) for OCT [2, 3].

In contrast, if diffraction-limited resolution is not required, then one can image deeper by utilizing the scattered light. Methods such as laminar optical tomography (LOT) and diffuse optical tomography (DOT) detect the scattered light [4–6]. These methods are feasible since scattering is dominant over absorption at optical wavelengths in biological tissues. LOT achieves resolutions on the order of hundreds of micrometers at depths of a few millimeters in tissue [6]. DOT, on the other hand, works in the diffusive regime and is able to image objects buried centimeters underneath tissue at resolution approaching 20% of the imaging depth [7]. However, these methods require characterization of the scattering properties and/or computational techniques in order to ‘invert’ the scattering process and retrieve information about the object.

Another strategy to image deeper is to acquire only a subset of the scattered light. The scattered light can be loosely categorized into two groups: (1) weakly-scattered ‘snake’ photons that are predominantly forward scattered and (2) more-strongly-scattered ‘diffuse’ photons. In highly anisotropic scattering media such as biological tissue, there exists more ‘snake’ photons. Preferential selection of these ‘snake’ photons over the more-strongly-scattered ‘diffuse’ photons can allow for imaging past the ballistic limit at moderate resolution [8–10]. The multiple-scattering, low-coherence interferometric (ms/LCI) systems coupled together a narrow angular collection aperture with interferometric detection to preferentially detect ‘snake’ photons and surpass the ballistic limit and image deep within scattering media, up to 40 round-trip mean free paths (MFPs) in a $g = 0.95$ sample and 90 MFPs in a $g = 0.988$ sample [10–12]. All of these systems employed a narrow collection aperture as well as offset illumination and detection in order to preferentially detect snake photons. To increase the signal-to-noise ratio, multiple acquisitions, up to

10^6 signal traces, were incoherently averaged [11]. One avenue yet unexplored is whether spatial gating or angular gating is more effective at improving imaging resolution.

In this work, we present a method that efficiently detects the back-scattered photons to directly image deeper in scattering media. We first investigate whether spatial or angular filtering is more effective at improving imaging resolution and also introduce speckle-resolution as an efficient method for coherently detecting multiply scattered light. Using Monte Carlo simulations, we show that spatial gating is more effective than angular gating at maintaining moderate resolution. We then build a speckle-resolved interferometric system, called Speckle-Resolved OCT (srOCT), that combines spatial, angular, and coherence gating to preferentially detect weakly scattered light in an efficient manner. We prove that speckle-resolved detection allows one to perform incoherent averaging in a single-shot manner. Using this system, we demonstrate imaging beyond the ballistic limit, to a depth of 90 MFPs in a $g = 0.96$ scattering phantoms and 4.5 mm in chicken breast tissue at resolutions on the order of a few hundred microns.

4.2 Simulation

Fig. 4.1 depicts one of the concepts behind Speckle-Resolved OCT (srOCT). In highly anisotropic media, the back-scattered light from the sample can be separated into two categories: (1) weakly scattered ‘snake’ photons (in blue) that are predominantly forward scattered and contain information about the target, and (2) strongly scattered ‘diffuse’ photons (in purple) that degrade contrast and resolution [9, 10]. The goal of this project is to preferentially detect the weakly scattered photons in an efficient manner. If snake photons exit the tissue at a closer distance to the incident light position or at narrower angles, then filtering the photons based on their exit position and/or angle may aid in preferentially detecting these snake photons. In this work, we investigate the impact that spatio-angular filtering (Fig. 4.1b) has on the imaging resolution and show that filtering provides an enhancement in lateral and axial resolution (Fig. 4.1c).

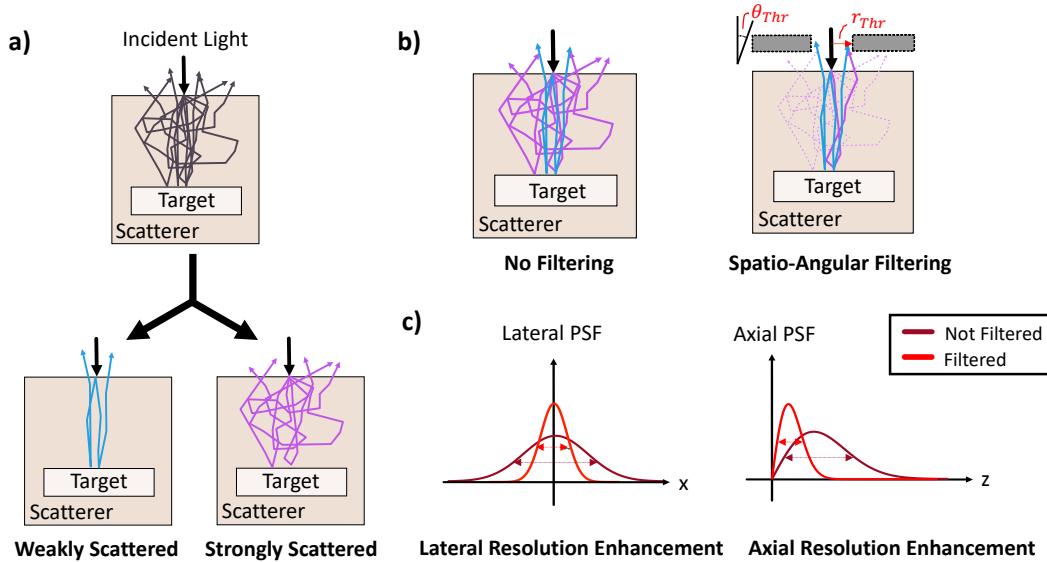


Figure 4.1: **Concept of Speckle-Resolved OCT (srOCT).** a) In highly anisotropic scattering media, there are two types of back-scattered photons: (1) non-scattered and weakly-scattered ‘snake’ photons (in blue) that are predominantly forward scattered and contain information about the structure of the target, and (2) strongly-scattered ‘diffuse’ photons (in purple) that degrade contrast and resolution. b) Filtering the back-scattered photons by their exit position and/or exit angle preferentially rejects diffuse photons. c) Spatio-angular filtering enhances the lateral and axial resolution.

We first investigated whether spatial and/or angular filtering improves resolution using Monte Carlo simulations. Simulations were performed with a pencil beam incident onto the center of a homogeneous scattering slab ($\mu_s = 10/\text{mm}$, $g = 0.90$) that was $500 \times 500 \times 500 \text{ mm}^3$ (MCX [13]). A total of 10^9 photons were simulated. Specular reflections from the tissue and air interface were ignored. Photons that exited the top surface of the slab, up to a distance of 100 mm from the center of the slab, were detected. For each photon, the following parameters were quantified: (1) s , the pathlength travelled in tissue; (2) $x_{max}, y_{max}, z_{max}$, the position of the photon at the maximum depth it travelled; (3) r , the exit position, measured as the distance from the incident light position; and (4) θ , the exit angle, measured relative to the angle for ballistic light detection, which is normal to the surface. For a target located at depth z_{depth} , only a subset of photons that interacted with the target, defined as $z_{max} \in [z_{targ} - \Delta z, z_{targ} + \Delta z]$, were considered detected. Some of these parameters have been shown in Fig. 4.2b.

To measure the impact of spatio-angular filtering on improving lateral and axial

resolution, the detected photons were filtered based on their exit position r and exit angle θ such that only those that satisfied $r \leq r_{thr}, \theta \leq \theta_{thr}$ were included, for some spatial range r_{thr} and angular range θ_{thr} (Fig. 4.2a). From the filtered photons, the lateral and axial resolution were estimated by the distribution in their position at maximum depth x_{max}, y_{max} and apparent depth $z_{depth} = \frac{s}{2n_{med}}$. The lateral resolution was estimated from the variance of x_{max}, y_{max} , which were considered to have the same underlying distribution due to symmetry (Fig. 4.2c). The axial resolution was estimated by measuring the full-width-at-half-maximum (FWHM) of the distribution of apparent depth $z_{depth} = \frac{s}{2n_{med}}$ (Fig. 4.2d).

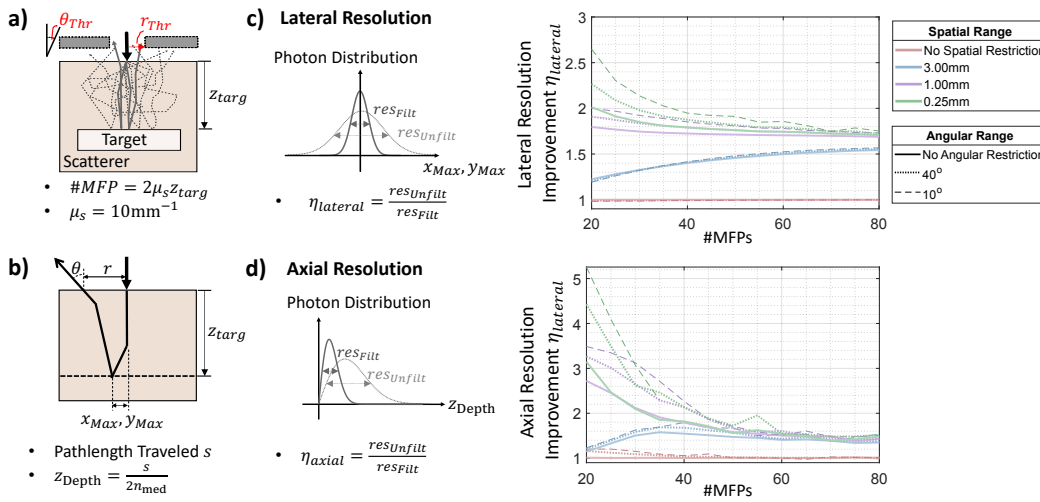


Figure 4.2: Impact of restricting spatial and angular range on improving resolution. a) Spatio-angular filtering restricts the detected photons to those that satisfy $r \leq r_{thr}, \theta \leq \theta_{thr}$, for a given target located at depth z_{targ} , $\#MFPs = \mu_s z_{targ}$. b) Parameters measured include the exit position r , exit angle θ , lateral position at the target x_{max}, y_{max} , and pathlength travelled s . c) Impact of filtering on improving the lateral resolution. The lateral resolution was estimated by computing the variance of the distribution of x_{max}, y_{max} . The enhancement is computed relative to the non-filtered case. d) Impact of filtering on axial resolution. The axial resolution was estimated by computing the FWHM of the distribution of apparent depth. The spatial restrictions are shown in different colors whereas the angular restrictions are shown as different line types. For both axial and lateral resolution, restricting the spatial range improves the resolution. Angular restriction is most effective at improving the resolution at shallower depths, and only improves resolution when combined with spatial filtering.

Fig. 4.2c,d provides plots showing the improvement in lateral and axial resolution with spatio-angular filtering, for spatial and angular restrictions of $r_{thr} \in$

[0.25 mm, 100 mm] and $\theta_{thr} \in [10 \text{ deg}, 90 \text{ deg}]$. The resolution improvement was defined relative to the resolution for the unfiltered case. To normalize the depth of imaging in scattering media with various scattering strengths, the target depth was reported as the number of round-trip mean free paths (#MFPs), which was defined as $\#MFPs = 2\mu_s z_{depth}$ where μ_s is the scattering coefficient.

For both lateral and axial resolution, spatial restriction enhances resolution to about 2 to 3 times for all depths studied. In the absence of any spatial restriction, angular restriction does not seem to improve resolution. However, angular restriction in conjunction with spatial restriction provides a further improvement, with more impact at shallower depths. Therefore, a combination of both spatial and angular filtering should be employed to maintain resolution.

4.3 Experimental Results

Fig. 4.3 depicts the principle behind how spatio-angular filtering is achieved experimentally. Light is weakly focused and illuminates the target. The back-scattered light from the target is detected by the camera. A reference beam, incident at an angle ϕ , interferes with the back-scattered light. The detected interference image contains information about the exit position and angle of the back-scattered light, which can be used to exclude some detected photons from processing (shown in gray).

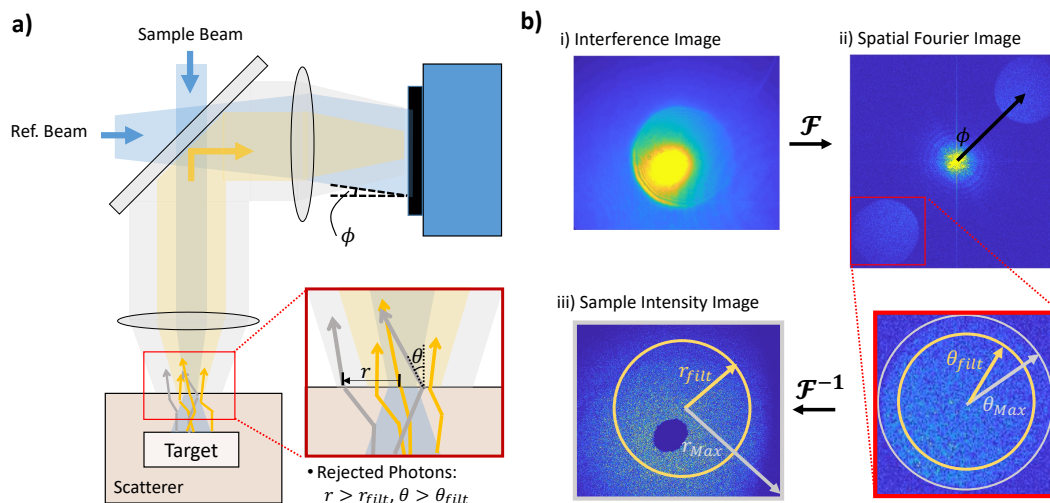


Figure 4.3: **Principle of Speckle-Resolved OCT (srOCT).** a) Light is weakly focused on a target located within a scattering medium. The exit position and angle of the back-scattered photons is used to preferentially reject the more strongly scattered photons (in gray) from the weakly scattered photons (in yellow). b) The filtering of photons based on exit position and angle is accomplished in processing. i) The camera records the interference pattern generated by the reference and back-scattered sample. ii) The spatial Fourier transform of the interference image contains a central peak and two side lobes whose center is shifted due to the reference beam tilt ϕ . The side lobes contain information about the exit angle and can be used to limit the processed photons to those that satisfy $\theta \leq \theta_{filt}$. iii) The inverse Fourier transform of one of the side lobes provides information of the back-scattered light from the sample and can be used to spatially filter the processed photons to those that satisfy $r \leq r_{filt}$.

Although the spatial and angular range is restricted based on the optical setup, further spatio-angular filtering can be performed in post-processing (Fig. 4.3b). Angular filtering is performed in the spatial Fourier domain whereas spatial filtering is performed in the spatial domain. The Spatial Fourier transform of the interference image (Fig. 4.3b,ii) contains a main lobe and two side lobes whose centers are shifted due to the reference angle tilt ϕ . The side lobe contains information about the exit angle of the back-scattered light and can be used to limit the processing only to photons whose exit angles satisfy $\theta \leq \theta_{filt}$. The inverse Fourier transform of one of the side lobes provides information about the exit position of the scattered light and can be used to restrict the processing to only include photons whose exit positions satisfy $r \leq r_{filt}$ (Fig. 4.3b,iii). Summing up the power within r_{filt} provides a measure of the sample intensity at a given x, y, z point.

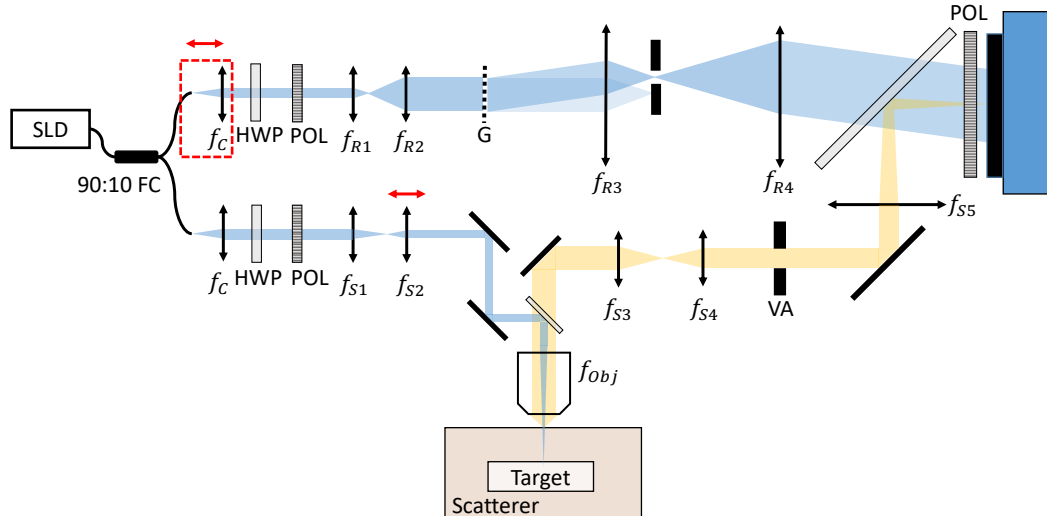


Figure 4.4: **Experimental setup for Speckle-Resolved OCT.** Light from an SLD is split into two arms, with 10% of the light going to the reference arm (top) and 90% to the sample arm (bottom). The reference beam light is collimated and incident upon a transmission grating, which divides the beam into multiple orders. Only the first order, arriving at an angle ϕ , is incident on the camera. The reference arm length is adjusted by moving the components in the red box. In the sample arm, light is incident upon an objective lens, which weakly focuses light on the target. The back-scattered light (in yellow) is transmitted by two 4f imaging systems to the camera, which is conjugated to the surface of the scattering medium. *Abbreviations:* FC, fiber coupler; f , lens; G, grating; HWP, half-wave plate; Obj, objective lens; POL, polarizer; and VA, variable aperture. *Lens focal lengths:* $f_c = 7.5$ mm, $f_{R1} = 10$ mm, $f_{R2} = 35$ mm, $f_{R3} = 75$ mm||100 mm, $f_{R4} = 200$ mm, $f_{S1} = 40$ mm, $f_{S2} = 30$ mm, $f_{Obj} = 12.5$ mm, $f_{S3} = 125$ mm, $f_{S4} = 100$ mm, $f_{S5} = 200$ mm.

The experimental setup for srOCT is shown in Fig. 4.4. Light from an SLD (SLD830S-A20; $\lambda = 830$ nm, $\Delta\lambda = 20$ nm; Thorlabs, NJ) was split by a fiber coupler into two arms, with 90% of the light going to the sample arm and 10% of the light going to the reference arm. In the reference arm, light was first collimated by lens f_c . The fiber coupler input and lens f_c were placed on a translation stage to perform axial (z) scanning. The collimated reference beam was expanded and then directed towards a transmission grating (G; 300 grooves/mm, GTI25-03A; Thorlabs, NJ), which was used to tilt the reference beam without adding pathlength mismatches. Only the first order of the diffracted beam was expanded and detected by the camera (PCOEdge 5.5; PCO, Germany). In the sample arm, light was first collimated and then transmitted to a water-immersion objective lens (N16XLWD-PF; Thorlabs, NJ), which weakly focused the light onto the target. The sample

was placed on an actuated translation stage (LTA-HS; Newport, CA) to scan the sample laterally. The focus was adjusted by translating lens f_{S2} . The back-scattered light from the sample was transmitted by two 4f systems to the camera, which was conjugated to the surface of the sample. A variable-aperture iris (VA) was used to limit the numerical aperture (NA) of the detection system to prevent aliasing.

The incident light power on the sample was 0.7 mW, and the system had an axial resolution of 15 μm in PDMS and agar. The lateral resolution of the system varied depending on the thickness of the sample and ranged from 50 μm to 100 μm . Data was acquired with an exposure time of 1 ms to 4 ms per image, which corresponds to a single voxel in the acquired dataset. The exposure time was limited by large back-reflections from the back-aperture of the objective lens and the sample, which was orders-of-magnitude larger than the back-reflected scattered light from the sample and saturated the camera detector.

The detected interference image at the camera can be mathematically represented as

$$I_{\text{det}}(\mathbf{r}) = |\mathbf{E}_{\mathbf{R}} + \mathbf{E}_{\mathbf{S}}(\mathbf{r})|^2 = I_{\mathbf{R}} + I_{\mathbf{S}}(\mathbf{r}) + 2E_{\mathbf{R}}E_{\mathbf{S}}(\mathbf{r}) \cos(k_0 \sin(\boldsymbol{\phi}) \cdot \mathbf{r} + \theta_{\mathbf{R}} - \theta_{\mathbf{S}}(\mathbf{r})) \quad (4.1)$$

where $\mathbf{E}_{\mathbf{R}}$, $\mathbf{E}_{\mathbf{S}}$ are the complex fields of the reference and sample beam, respectively; $I_{\mathbf{R}} = |\mathbf{E}_{\mathbf{R}}|^2$, $I_{\mathbf{S}} = |\mathbf{E}_{\mathbf{S}}|^2$ are the reference and sample intensities; $k_0 = \frac{2\pi}{\lambda}$ is the wavenumber; $\mathbf{r} = (x, y)$ is the lateral position; $\boldsymbol{\phi} = (\phi_x, \phi_y)$ is the reference beam tilt angle; and $\sin(\boldsymbol{\phi}) = (\sin(\phi_x), \sin(\phi_y))$. The reference beam is modelled as a plane wave with $\mathbf{E}_{\mathbf{R}} = E_{\mathbf{R}}e^{j\theta_{\mathbf{R}}}$ where $E_{\mathbf{R}}$, $\theta_{\mathbf{R}}$ are constants. The complex speckle field of the sample beam is denoted as $\mathbf{E}_{\mathbf{S}}(\mathbf{r}) = E_{\mathbf{S}}(\mathbf{r})e^{j\theta_{\mathbf{S}}(\mathbf{r})}$.

In the spatial Fourier domain, this equation becomes:

$$\tilde{I}_{\text{det}}(\mathbf{k}) = \mathcal{F} [I_{\mathbf{R}} + I_{\mathbf{S}}] (\mathbf{k}) + \mathcal{F} \left[E_{\mathbf{R}}E_{\mathbf{S}}e^{\pm j(\theta_{\mathbf{R}} - \theta_{\mathbf{S}})} \right] (\mathbf{k} \pm k_0 \sin(\boldsymbol{\phi})) \quad (4.2)$$

where $\mathcal{F} [\cdot]$ denotes the 2D Fourier transform, $\tilde{I}_{\text{det}}(\mathbf{k}) = \mathcal{F} [I_{\text{det}}(\mathbf{r})]$, and $\mathbf{k} = (k_x, k_y)$. The two side lobes centered at $\mathbf{k}_{\text{shift}} = \pm k_0 \sin(\boldsymbol{\phi})$ contain information about the sample beam $\mathcal{F} [E_{\mathbf{R}}E_{\mathbf{S}}e^{\pm j(\theta_{\mathbf{R}} - \theta_{\mathbf{S}})}]$. Computing the inverse Fourier transform of one of the side lobes yields $E_{\mathbf{R}}E_{\mathbf{S}}e^{\pm j(\theta_{\mathbf{R}} - \theta_{\mathbf{S}})}$. A reference-only image provides an estimate of $E_{\mathbf{R}}$. Summing the power within $r < r_{\text{filt}}$, $\theta < \theta_{\text{filt}}$ provides an estimate of the total back-scattered power from the sample at a given x, y, z point. A depth scan, or a-scan, was acquired by imaging the sample at a given lateral position while scanning axially in z . A cross-sectional b-scan, which provides an

image of depth vs lateral dimension, was acquired by scanning z as well as either x or y .

The back-scattered sample light \mathbf{E}_S forms a speckle field with speckle grain size determined by the detection system optics. For speckle-resolved detection, the speckle grain size is constrained to prevent aliasing in the Fourier domain and ensure that each speckle grain is resolved by at least one detector element. The smallest speckle size at the camera is $d_{\text{speckle}} = \frac{\lambda}{2} \frac{M}{NA}$ where M is the magnification and NA is the numerical aperture of the detection path [14]. In order to avoid aliasing in the spatial Fourier domain, the speckle grain size must satisfy $d_{\text{speckle}} \geq 3.12d_{\text{pixel}}$. In our case, $M = 20$ and $NA \leq 0.4$, which resulted in a speckle size of $d_{\text{speckle}} \geq 21 \mu\text{m}$. Due to the physical dimensions of the camera along with the detection optics, the maximum spatial and angular range of the setup was $r_{\text{thr}} = 0.35 \text{ mm}$ and $\theta_{\text{thr}} = 17.4 \text{ deg}$ and the maximum number of speckles detectable by our system was 4.2×10^4 . The maximum spatial and angular range are close to the smallest that was used during simulation.

Imaging Scattering Phantoms

Scattering phantoms were constructed to determine the srOCT system response. These scattering phantoms were fabricated by dispersing polystyrene microspheres (Polysciences, Inc., PA) in polydimethylsiloxane (PDMS; MilliporeSigma, MO). $1 \mu\text{m}$ and $3 \mu\text{m}$ beads were used to construct two different phantoms with the following scattering properties: (1) $g = 0.91$, $\mu_S = 11/\text{mm}$ and (2) $g = 0.96$, $\mu_S = 16/\text{mm}$ (as determined by Mie theory). A thickness-matched layer of PDMS was also included to aid in alignment.

The scattering phantom was placed on top of a USAF resolution target (Thorlabs, NJ) in order to measure the lateral and axial resolution (Fig. 4.5a). The edges of the square target were used to measure lateral resolution whereas the axial response to the chrome reflector was used to measure axial resolution. Fig. 4.5b,c show cross-sectional b-scans of the edge through various thicknesses of scattering media for both types of samples. The SNR degrades with thicker scattering media; however, the signal from the edge is still clearly seen, even below a 2.77 mm -thick phantom, corresponding to 89 round-trip MFPs.

Fig. 4.5d depicts how the lateral and axial resolution was experimentally measured. An a-scan was acquired at the approximate location shown by the dashed line, with the chrome target; this a-scan provided the axial response. For the lateral

response, the rows of the b-scan were averaged to compute the edge response. The integral of a Gaussian curve was fitted to denoise the edge response, and the derivative of this fitted edge response yielded the lateral response. The lateral and axial resolution were estimated by computing the FWHM of the lateral and axial responses, respectively.

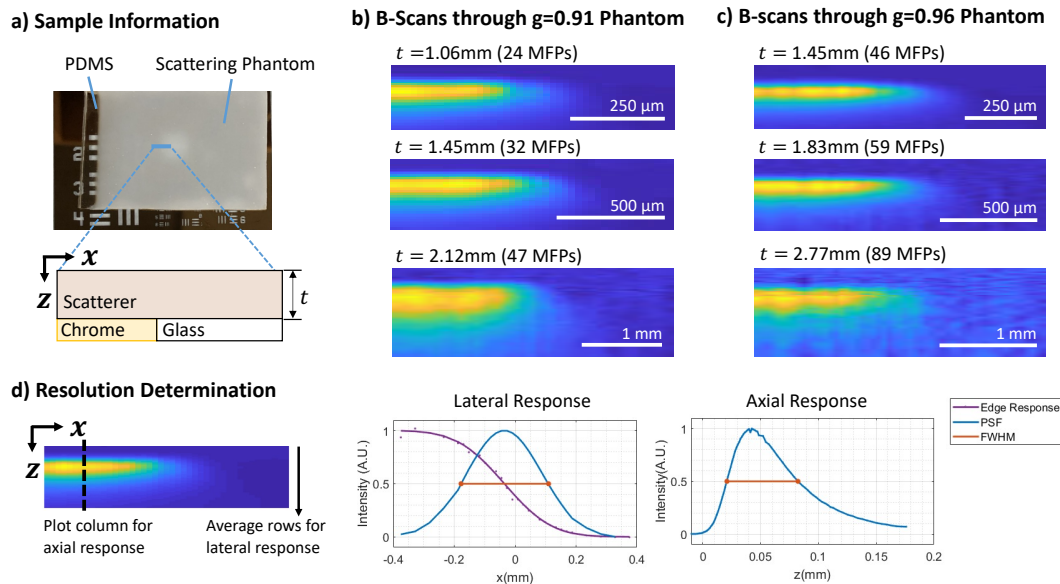


Figure 4.5: **srOCT imaging through a scattering phantom.** a) The sample, consisting of a scattering phantom (polystyrene microspheres embedded in PDMS) and a thickness-matched transparent PDMS layer, is placed upon a USAF resolution target. B-scans of the target are acquired through the scattering media and are used to measure the edge response and estimate the lateral resolution (approximate location shown in blue). b), c) B-scans of the target, acquired through various thicknesses of scattering media t , for phantoms with scattering anisotropy of $g = 0.91$ and $g = 0.96$, respectively. d) From the b-scan, the lateral edge response is computed by averaging the rows. This edge response is fitted and differentiated to measure the lateral resolution. The axial resolution is measured by looking at the signal from the chrome target.

Fig. 4.6 shows the lateral and axial resolution as a function of both the number of round-trip MFPs and TMFPs. The resolution has been normalized to the target depth. Both the lateral resolution (Fig. 4.6a) and axial resolution (Fig. 4.6c) degrade as you image deeper in scattering media. However, the resolution degrades more slowly for scattering media with higher anisotropy. When plotted as a function of TMFPs (Fig. 4.6b,d), the lateral and axial resolutions appear to degrade at a similar rate for both types of scattering phantom.

We also investigated the impact of performing further spatio-angular filtering on the acquired data sets (Fig. 4.6); the filtered points have been shown as circles. Experimentally, $r_{thr} \in [10 \mu\text{m}, 350 \mu\text{m}]$, $\theta_{thr} \in [1 \text{ deg}, 17.4 \text{ deg}]$. The results for no further filtering ($r_{thr} = 350 \mu\text{m}$, $\theta_{thr} = 17.4 \text{ deg}$) have been shown alongside the best results we could measure with further filtering. Although filtering did improve the resolution, the magnitude was modest.

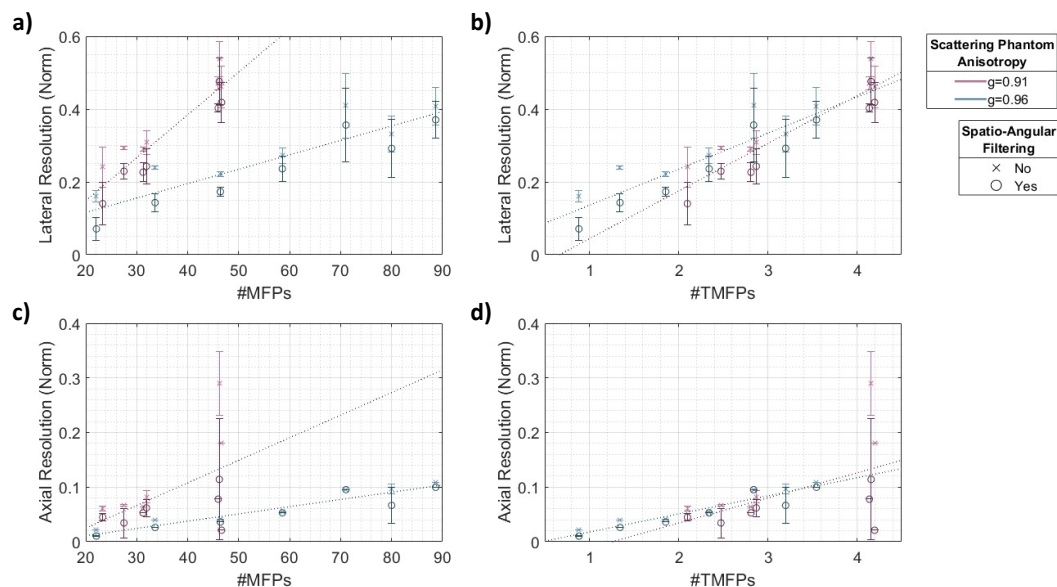


Figure 4.6: Lateral and axial resolution of srOCT. The lateral and axial resolution of the imaging system for a chrome target placed behind various thicknesses of scattering media was determined. The resolution is normalized to the target depth. a) and c) show the lateral and axial resolution as a function of number of round-trip mean free paths, whereas b) and d) show the lateral and axial resolution as a function of round-trip transport mean free paths (TMFPs). Both lateral and axial resolution degrade with increasing #MFPs. The rate of degradation is slower when imaging through scattering media with higher anisotropy. However, when normalized to #TMFPs, the resolution degradation appears to be comparable.

SNR

Two of the aims of the paper were: (1) to investigate whether spatial or angular filtering impacted imaging resolution, and (2) to introduce speckle-resolved detection as an efficient method for detecting multiply scattered photons. Through simulation, we showed that spatial filtering improves imaging resolution, and angular filtering provides an enhancement only in conjunction with spatial filtering. We now turn our attention to the benefit of speckle-resolved detection.

When imaging in scattering media, the back-scattered sample light \mathbf{E}_S forms a

speckle field. In this section, we will consider the case where there are N_{speckle} speckles incident on the detector, each with area A_{speckle} . In the case of speckle-resolved detection, each speckle is detected by at least one detector element. As we shall see, this allows us to incoherently combine the information from each speckle and provides an SNR advantage N_{speckle} ; that is,

$$\text{SNR}_{\text{speckle-resolved}} \propto N_{\text{speckle}} \times \text{SNR}_{\text{non-speckle-resolved}}. \quad (4.3)$$

In interferometric techniques, the detected signal can be generally written as

$$I_{\text{det}} = |\mathbf{E}_R + \mathbf{E}_S|^2 = I_R + I_S + \mathbf{E}_R \mathbf{E}_S^* + \mathbf{E}_R^* \mathbf{E}_S \quad (4.4)$$

where $I_R \gg I_S$ and the reference beam is a plane wave.

In the scenario where the sample light is a speckle field, the signal from a single speckle grain is of the form

$$I_{\text{sig},i} = E_R \mathbf{E}_{S,i} = E_R E_{S,i} e^{j\theta_{s,i}} \quad (4.5)$$

where $E_{s,i}$ and $\theta_{s,i}$ are the amplitude and phase of the i^{th} speckle grain, respectively. We consider the case where there are N_{speckle} speckle grains incident on the detector, each with area A_{speckle} . For this section, we also consider the case of shot-noise-limited detection, $\sigma_{\text{noise}}^2 \approx \sigma_{\text{shot}}^2$. Since $I_R \gg I_S$, shot noise is dominated by contributions from the reference arm.

Speckle-Resolved Detection

In the case of speckle-resolved detection, each speckle is detected by at least one detector element, and the total signal can be found by summing the magnitude of each speckle. This results in the following expected signal:

$$\mathbb{E} \left[\sum_{i=1}^{N_{\text{speckle}}} A_{\text{speckle}} E_R E_{S,i} \right] = A_{\text{speckle}} E_R N_{\text{speckle}} \mathbb{E}[E_S]. \quad (4.6)$$

The shot noise of each speckle is $\sigma_{\text{shot},i}^2 = I_R A_{\text{speckle}} \eta T$. Since the shot noise of each speckle is uncorrelated, the shot noise of the summed signal is $\sigma_{\text{shot}}^2 = N_{\text{speckle}} \sigma_{\text{shot},i}^2 = I_R A_{\text{speckle}} N_{\text{speckle}} \eta T$.

The SNR is

$$\text{SNR}_{\text{speckle-resolved}} \propto \frac{(\eta T A_{\text{speckle}} N_{\text{speckle}} E_R \mathbb{E}[E_S])^2}{\eta T A_{\text{speckle}} I_R N_{\text{speckle}}} = \eta T N_{\text{speckle}} P_{\text{speckle}}, \quad (4.7)$$

where $I_S = \mathbb{E}[E_S]^2$ and $P_{\text{speckle}} = I_S A_{\text{speckle}}$. The SNR scales linearly with N_{speckle} and is directly proportional to the total number of photo-electrons detected from the sample.

Non-Speckle-Resolved Detection

In the case of non-speckle-resolved detection, all of the speckles are incident on a single detector, which integrates the signal. Therefore, the detected intensity and signal follow:

$$I_{\text{det}} = \sum_{i=1}^{N_{\text{speckle}}} |\mathbf{E}_R + \mathbf{E}_{S,i}|^2 = \sum_{i=1}^{N_{\text{speckle}}} [I_R + I_{S,i} + \mathbf{E}_R \mathbf{E}_{S,i}^* + \mathbf{E}_R^* \mathbf{E}_{S,i}] \quad (4.8)$$

$$I_{\text{sig}} = E_R \sum_{i=1}^{N_{\text{speckle}}} E_{S,i} e^{j\theta_{s,i}}. \quad (4.9)$$

The expected value of the signal is

$$\mathbb{E} \left[\left| E_R \sum_{i=1}^{N_{\text{speckle}}} E_{S,i} e^{j\theta_{s,i}} \right| \right] = E_R \sqrt{N_{\text{speckle}}} \mathbb{E}[E_S]. \quad (4.10)$$

The shot noise is still dominated by contributions from the reference beam and is $\sigma_{\text{shot}}^2 = A_{\text{speckle}} N_{\text{speckle}} I_R \eta T$. Therefore, the SNR is:

$$\text{SNR}_{\text{non-speckle-resolved}} \propto \frac{\left(A_{\text{speckle}} E_R \sqrt{N_{\text{speckle}}} \mathbb{E}[E_S] \eta T \right)^2}{A_{\text{speckle}} N_{\text{speckle}} \eta T I_R} = \eta T P_{\text{speckle}}. \quad (4.11)$$

Unlike the case of speckle-resolved detection, the SNR is proportional to the average number of photo-electrons detected in a single speckle.

Impact of Averaging Multiple Acquired Signals

In order to boost the SNR, one can acquire and incoherently average multiple signal traces. In this case, the signal term remains the same, but the noise term decreases by a factor of N_{ave} . Thus, the SNR becomes $\text{SNR}_{N_{\text{ave}}} = N_{\text{ave}} \text{SNR}_{\text{single}}$.

SNR Comparison

Speckle resolution provides an SNR advantage of N_{speckle} as it allows us to incoherently combine the power from each speckle and measure the total back-scattered power from the sample. In contrast, in the non-speckle-resolved scenario, the measured signal is proportional to the photons contained within a single speckle. In essence, speckle resolution allows us to incoherently average the information from multiple speckles in a single-shot manner.

To highlight the impact of speckle-resolved detection, we compared it to non-speckle-resolved detection and conventional OCT. B-scans were acquired with the detection and illumination focused on the target in order to simulate conventional OCT acquisition. 4 different thicknesses of the $g = 0.91$ phantom were imaged: $t = 1.06, 1.25, 1.45, \text{ and } 2.12\text{mm}$. After detecting the interference image, spatio-angular filtering was applied to the conventional OCT case to mimic confocal detection. The same data set was also processed in a non-speckle-resolved manner. For a chrome target placed 1.25 mm behind a $g = 0.91$ scattering phantom, the chrome signal is clearly resolved in the speckle-resolved case, in contrast to conventional OCT processing and non-speckle-resolved detection (Fig. 4.7a). Similar results were seen for the $t = 1.45, 2.12\text{mm}$ phantoms.

We measured the SNR of srOCT a-scans acquired of the chrome target through the scattering phantoms. We also imaged the $1\ \mu\text{m}$ -bead phantoms with a commercial OCT system (Ganymede 611C1 Spectral-Domain OCT; Thorlabs, NJ). According to Mie theory, the scattering properties of the phantom was $\mu_s = 9/\text{mm}$ and $g = 0.89$ at $\lambda = 930\ \text{nm}$. The SNR of the commercial OCT, OCT processing, and srOCT has been provided in Fig. 4.7. Both the conventional OCT processing and commercial OCT systems appear to have similar SNR. The data from the srOCT system has approximately 40 dB improvement in SNR over conventional OCT processing.

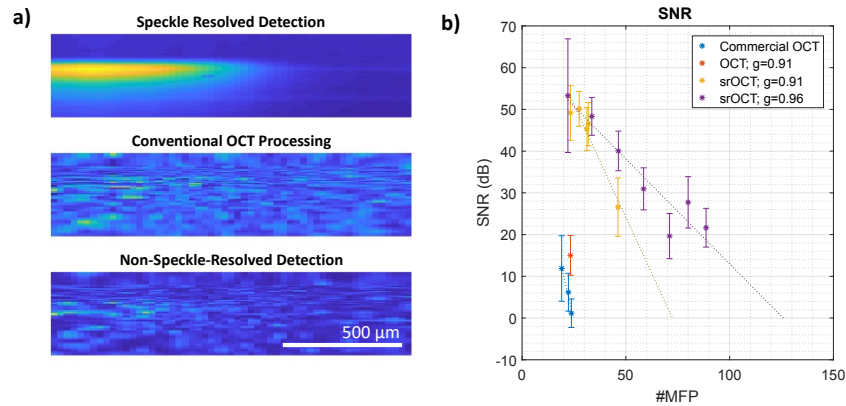


Figure 4.7: **SNR advantage speckle resolution** a) B-scans of data processed using speckle-resolved detection, conventional OCT processing, and non-speckle-resolved detection highlight the SNR advantage to speckle-resolved detection. A chrome target was placed behind 1.25mm of $g=0.91$ scattering phantom. b) SNR for Speckle-Resolved, Non-Speckle-Resolved, and Conventional OCT for different scattering media thicknesses. The results from using a commercial OCT system are also presented.

Biological Results

We lastly demonstrated srOCT on a biological sample. We first measured the resolution through chicken breast tissue (Fig. 4.8). A piece of chicken breast tissue was sandwiched in between a coverglass and either a USAF resolution target (Fig. 4.8a,c) or a glass slide (Fig. 4.8 b). iSpacers (Sunjin Lab, Taiwan) were used to control the sample thickness. Similar to the scattering phantom case, the square target (approximate location shown in green) was used to estimate the resolution and SNR (Fig. 4.8a). Cross-sectional b-scans of the target acquired through two thicknesses of chicken tissue have been shown in fig.4.8a,ii. The resolution and SNR through chicken breast tissue has also been provided, for tissue thicknesses of up to 4.4 mm (Fig. 4.8a,iii,iv). When imaging underneath chicken breast tissue, the axial and lateral resolution steadily degraded; however, even at a depth of 4.4 mm, resolution of approximately 400 μm was achieved.

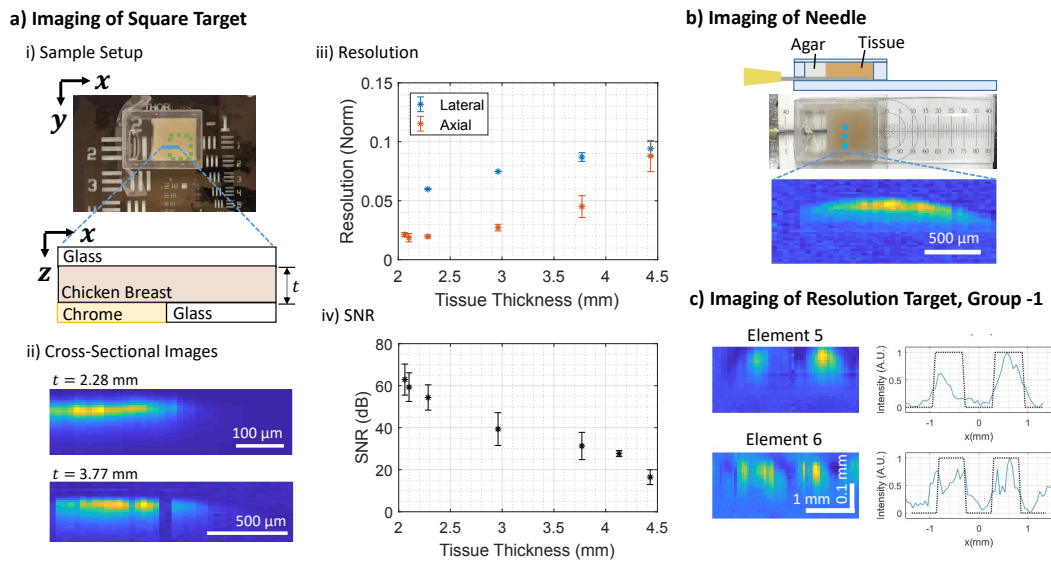


Figure 4.8: **srOCT imaging through biological sample.** a) The square pattern on a USAF resolution target was used to determine the resolution and SNR of imaging through chicken breast tissue. i) A piece of chicken breast tissue was sandwiched between a coverslip and the resolution target and covers a clear square pattern (approximate location shown in green). ii) Cross-sectional images of the target, acquired underneath chicken tissue thicknesses of $t = 2.28, 3.77$ mm. iii) The lateral and axial resolution of srOCT through various chicken tissue thicknesses. Both the lateral and axial resolution degrade with depth, reaching to $\sim 0.1t$ for $t = 4.5$ mm. iv) The experimentally measured SNR for a chrome target through various chicken tissue thicknesses. e) A 20G needle was placed underneath chicken tissue, with the top of the needle located 4.1 mm below the tissue surface. Pictorial schematic and photo of setup is provided along with a cross-sectional image acquired using srOCT. The blue dashed line shows the approximate location of where the cross-sectional image in was acquired. f) Cross-sectional images of Group -1, Elements 4 – 6 of a USAF target located underneath 3.8 mm of tissue, along with their corresponding line plot. srOCT is able to isolate the target both in depth as well as resolve the bars. The dashed lines show the approximate location of the bars.

After measuring the resolution, we turned to imaging a needle and a resolution target through chicken breast tissue. Fig. 4.8b provides images of a needle buried under 4.1 mm of chicken breast tissue. Although not visible by eye, using srOCT, we can clearly resolve the top of the needle through the chicken breast tissue. In the case of the USAF target located underneath 3.8 mm of tissue, the depth and lateral position of the bars are clearly distinguished (Fig. 4.8c). The plots on the right show the srOCT response (in blue) along with the theoretical location of the bars (in dashed lines).

4.4 Discussion

In summary, we present a new method, termed Speckle-Resolved OCT (srOCT), that preferentially detects weakly scattered photons in a speckle-resolved manner to enable imaging past the ballistic limit with moderate resolution. Spatio-angular filtering was employed to preferentially reject the diffusely scattered photons. The speckles from the back-scattered sample light were resolved on the detector, which allowed us to detect the total back-scattered power. Using this method, we were able to image up to 47 MFPs in $g = 0.91$ scattering media, 89 MFPs in $g = 0.96$ scattering media, and 4.4 mm in chicken breast tissue. In the remainder of this section, we discuss the results of our investigations as well as some factors that impact system performance.

We demonstrate that speckle-resolved detection is an efficient method to detect the back-scattered light from the sample as $\text{SNR}_{\text{speckle-resolved}} \propto N_{\text{speckle}} P_{\text{speckle}}$. In contrast, $\text{SNR}_{\text{non-speckle-resolved}} \propto P_{\text{speckle}}$. This difference is due to the fact that speckle-resolved schemes allow for incoherent summation of the information from each speckle. A similar SNR advantage can be achieved by acquiring and incoherently averaging multiple acquisitions; in this case, $\text{SNR}_{N_{\text{ave}}} \propto N_{\text{ave}} P_{\text{speckle}}$. Speckle-resolved detection allows us to gain the same advantage with a single acquisition. N_{speckle} is limited by the number of detector elements. Since many cameras have pixel counts on the order of $10^5 \sim 10^6$, speckle-resolved detection can provide a large boost in SNR in a single-shot manner and might be more suitable for imaging dynamic samples.

We also investigated the impact of spatio-angular filtering on imaging resolution and found that spatio-angular filtering improved resolution in simulation, but the improvement was modest in experiments. One reason is that the ranges of spatial and angular restrictions tested were much wider in simulation than experimentally. The ranges used in simulation were $r_{thr} \in [0.25 \text{ mm}, 100 \text{ mm}]$ and $\theta_{thr} \in [10 \text{ deg}, 90 \text{ deg}]$ whereas the experimental ranges were $r_{thr} \in [1 \mu\text{m}, 350 \mu\text{m}]$ and $\theta_{thr} \in [1 \text{ deg}, 17.4 \text{ deg}]$. In simulation, we saw that changing r_{thr} from 100 mm to 1 mm provided a large improvement in resolution; however, further restriction from 1 mm down to 0.25 mm provided a more modest amount. Since experimentally $r_{thr} \leq 350 \mu\text{m}$, we expect a smaller enhancement in resolution. The impact of smaller r_{thr} and θ_{thr} were not tested in simulation due to the limited number of photons simulated, but is an interesting avenue to explore in future work.

A second reason why we did not see as large a resolution improvement experimen-

tally is because spatio-angular filtering degraded the signal SNR. Angular filtering increases the speckle size whereas spatial filtering decreases the field-of-view. The net effect is that both spatial filtering and angular filtering will cause a decrease in the number of speckles $N_{speckles}$, which will directly impact the SNR since $\text{SNR}_{\text{speckle-resolved}} \propto N_{\text{speckle}}$. The degradation of SNR limited the amount of restriction that could be applied post-processing and still yield a signal with sufficient SNR to measure the resolution.

Experimentally, the lateral and axial resolution were quantified using data acquired from scattering phantoms with 2 different scattering anisotropies: $g = 0.91$ and $g = 0.96$. We found that, when plotted as a function of MFP, resolution degraded more slowly in the case of imaging through media with higher anisotropy. This makes sense as photons would be more forward scattered in higher anisotropy media, and therefore provide better resolution. Surprisingly, when plotted as a function of TMFPs, both the axial and lateral resolutions for both types of scattering phantoms seem to have the same trend. This suggests that the resolution might be comparable for scattering media with different scattering anisotropies, when the resolution is compared to TMFPs. Further studies are needed to conclusively determine how scattering anisotropy and scattering strength (μ_S) impacts resolution.

Overall, we found that spatial filtering was effective in improving resolution and that angular filtering was only effective when applied in conjunction with spatial filtering. Since the speckle field that is backscattered from the sample also has a limited spatial extent ($r_{\text{speckle-field}}$), one should design the imaging system with $r_{thr} \leq r_{\text{speckle-field}}$. As spatial filtering has more of an impact on resolution, one should set r_{thr} first and then set θ_{thr} correspondingly in order to maximize the number of speckles captured by the detection system.

Lastly, our system was designed as a proof-of-concept system to investigate the impact of spatio-angular filtering on imaging resolution and introduce speckle-resolved detection as an efficient means of coherently detecting multiply scattered light. To this end, we designed the detection path to be (1) parallel to the incident light beam and (2) conjugated to the surface of the scattering media. However, srOCT can also be applied to other imaging geometries. Offset illumination and detection can allow for more sensitivity to snake photons by reducing the contribution of sub-surface-scattered photons and surface reflections [10, 12, 15]. Distinct illumination and detection pathways would also remove issues stemming from reflections off the surface of the sample, other optical components, or objective lens. In our proof-of-

concept system, these reflections hampered our ability to detect the light from the sample, as the reflections were orders-of-magnitude larger than the desired sample light. We conjugated the camera to the surface of the scattering media in order to investigate the impact of spatio-angular filtering. If further filtering based on exit position or angle is not necessary, then one can also conjugate the detection to the focus plane of the illumination beam.

4.5 Conclusion

In conclusion, we demonstrated imaging past the ballistic regime at moderate resolution by preferentially detecting snake photons in a coherent and speckle-resolved manner. The back-scattered light from the sample was filtered by the exit position and the exit angle to preferentially detect the weakly-scattered snake photons that provide more imaging resolution. Speckle-resolved detection also allowed for coherent detection of the back-scattered light with high sensitivity. The focus of this paper was to investigate the impact of spatio-angular filtering and introduce the advantage of speckle-resolved detection. To this end, we built a proof-of-concept device, with which we demonstrated imaging through scattering phantoms at a depth that was approximately 3x thicker than the OCT limit. With appropriate optimizations, this project opens up potential for use in applications involving imaging targets deep within scattering media where moderate resolution on the order of 100s of microns is satisfactory, such as imaging and locating subcutaneous veins for phlebotomy and sclerotherapy [16].

Appendix 1 – Investigation of Exit Position and Exit Angle Distribution of Snake Photons

In this appendix, we present the results of investigations using Monte Carlo simulations on whether snake photons exit the tissue with narrower angular and spatial ranges in comparison to the diffuse photons. This provides the basis for why spatio-angular filtering can provide an improvement in resolution.

To compare the exit information of the scattered photons, the back-scattered light was separated into 3 classes of photons, based on the amount of scattering and whether they interacted with the target layer (Fig. 4.9a). Photons were considered to interact with the target layer depth if $z_{max} \in [z_{Targ} - \Delta z, z_{Targ} + \Delta z]$. Class I consists of minimally scattered ballistic and snake photons that reach the target layer in the medium. These photons provide the most information about the local structure of the tissue and provide better spatial and axial resolution. In contrast,

Class II consists of multiply-scattered photons that do not reach the target but travel the same pathlength as Class I photons; these photons serve to decrease imaging contrast and sensitivity. Class III photons are multiply-scattered photons that reach the target layer but travel a longer pathlength than Class I photons; collection of these photons serve to broaden the axial and lateral response and decrease imaging resolution. The remainder of the photons travel a different distance from Class I photons and do not interact with the target layer. These photons are rejected by the coherence gate and were thus not considered. Our goal is to preferentially detect Class I photons by using a combination of spatial and angular filtering to reduce the contribution of Class II and Class III photons.

The strength of scattering was quantified based on the pathlength travelled in tissue, relative to the maximum penetration depth. Ballistic photons have relative pathlength $s_{rel} = \frac{s}{2n_{med}z_{max}} = 1$. Class I photons had $s_{rel} \leq s_{thr}$, and Class II and III photons had $s_{rel} > s_{thr}$. s_{thr} was defined relative to the mean pathlength travelled. That is, for a given z_{Targ} , the pathlength distribution of all the detected photons satisfying $z_{max} \in [z_{Targ} - \Delta z, z_{Targ} + \Delta z]$ can be computed. From this, s_{thr} was determined related to the mean of this pathlength distribution, s_{mean} , and was defined as

$$s_{thr} = \frac{1}{15} \left[\frac{s_{mean}}{2n_{med}z_{Targ}} - 1 \right] + 1.$$

Fig. 4.9b,c shows the probability distribution in exit position and exit angle for Class I, II, and III photons for a target layer depth of $z_{targ} = 1$ mm, corresponding to 20 MFPs. In comparison to Class II and III photons, Class I photons exit the tissue with a smaller position and angle distribution. Class III photons exit the tissue with the broadest distribution in position.

To establish whether Class I photons exit closer or at narrower angles, we computed the spatial and angular spread of the photons, which was defined as the position or angle within which 75% of a given class of photons was detected (Fig. 4.9d,e). At all depths, Class I photons have the narrowest spatial and angular spread in comparison to Class II and III photons. Class II photons have the largest spatial spread. This suggests that both angular and spatial filtering should be effective in rejecting Class II and III photons and improving imaging resolution.

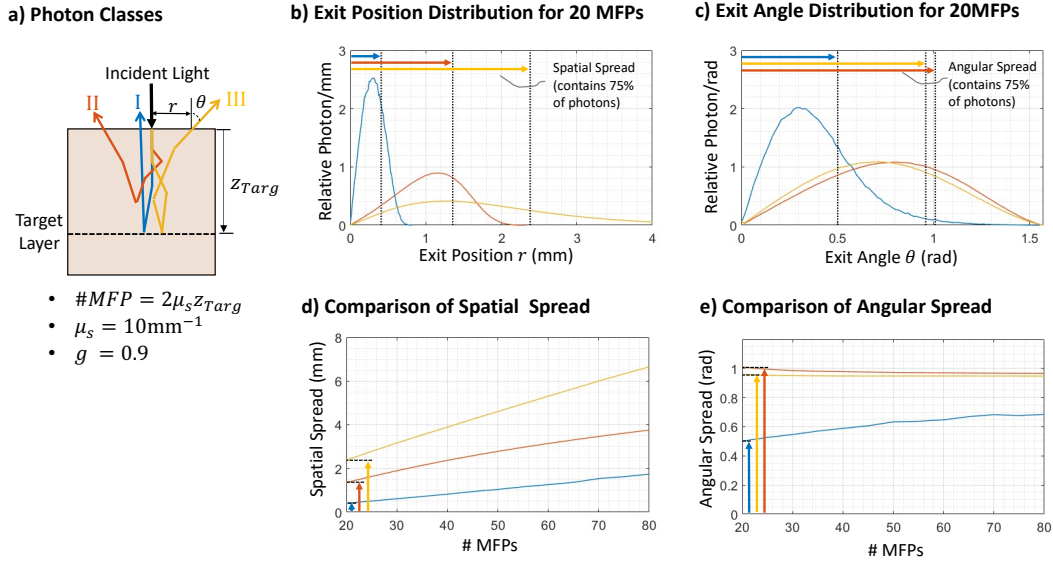


Figure 4.9: **Comparison of the exit position and the exit angle for different classes of photons.** a) 3 classes of photons were considered: I – non-scattered and weakly-scattered ‘snake’ photons; II – strongly-scattered ‘diffuse’ photons that do not interact with the target and decrease contrast; and III – strongly-scattered photons that interact with the target and degrade resolution. b,c) Histograms of the exit position r and exit angle θ for the 3 classes of photons for $z_{Targ} = 1$ mm. Class I photons have smaller exit positions and angles compared to Class II and III photons. d,e) Comparison spatial spread and angular spread of Class I, II, and III photons. The spatial and angular spread were computed as the range of position or angle that contained 75% of the photons from a given class. For the range of round-trip MFPs studied, Class I photons exhibit much smaller spatial and angular spreads than Class II and Class III photons.

Appendix 2 – Derivation of the Speckle Size Constraint

This section presents the derivation for the speckle size limitations of $d_{\text{speckle}} = 3.12d_{\text{pixel}}$ where d_{pixel} is the pixel size of the camera and d_{speckle} is the size of the speckle intensity grain.

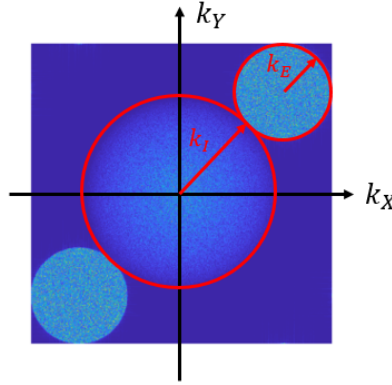


Figure 4.10: Determination of speckle size constraint to prevent aliasing in off-axis holography

The Fourier domain image of the interference image (Fig. 4.10) contains a main lobe (with radius k_I) and two side lobes (with radius k_E) and can be mathematically described as:

$$\tilde{I}_{det}(\mathbf{k}) = \mathcal{F}[I_R + I_S](\mathbf{k}) + \mathcal{F}[E_R E_S](\mathbf{k} \pm k_0 \sin(\phi) \cdot \mathbf{r}).$$

Here, we assume a flat, plane-wave reference beam such that E_R is a constant. The remaining variables have been defined in the main text.

Since the main lobe is the Fourier transform of the speckle intensity $I_S = |\mathbf{E}_S|^2$ whereas the side lobes is the Fourier transform of E_S , we have that $k_I = 2k_E$.

The maximum k of the image is determined by the pixel size and is $k_{max} = \frac{\pi}{d_{\text{pixel}}}$ due to Nyquist theory. To avoid aliasing, we have the limit that

$$\begin{aligned} \frac{1}{\sqrt{2}}(k_I + k_E) + k_E &\leq k_{max} \\ \frac{3 + \sqrt{2}}{2\sqrt{2}}k_I &\leq k_{max} \\ d_I &\geq \frac{3 + \sqrt{2}}{\sqrt{2}}d_{\text{pixel}} \approx 3.12d_{\text{pixel}} \end{aligned}$$

where $k_I = \frac{2\pi}{d_I}$ and $d_I = d_{\text{speckle}}$ is the speckle intensity grain size.

Appendix 3 – Signal-to-Noise Considerations

For this section, we consider the SNR of interferometric detection. Let i be the detected photo-current, n be the detected number of photo-electrons, and I be the intensity. Furthermore, let the subscripts R, S denote the reference and sample, respectively. We have that the detected interference image is

$$I = I_R + I_S + \mathbf{E}_R \mathbf{E}_S^* + \mathbf{E}_R^* \mathbf{E}_S$$

where $I_R \gg I_S$. We also have that

$$n = \frac{\eta}{h\nu} I T A = \epsilon I T A$$

$$i = \frac{nq}{T}$$

where $h\nu$ is the energy of a single photon, T is the exposure time, A is the area of each pixel, and η is the photo-electron conversion efficiency.

In the SNR comparison provided in this chapter, we only considered shot-noise-limited detection. In general, as shown in Chapter 2 Section 2.6, the noise in an interferometric system can be considered to contains contributions from 3 sources:

$$\sigma_{\text{noise}}^2 = \sigma_{\text{det}}^2 + \sigma_{\text{shot}}^2 + \sigma_{\text{ex}}^2. \quad (4.12)$$

Here, σ_{det}^2 is detector noise, σ_{shot}^2 is shot noise, and σ_{ex}^2 is excess intensity noise.

To be in the shot-noise-limited regime, we need that $\sigma_{\text{shot}}^2 \gg \sigma_{\text{ex}}^2$ and $\sigma_{\text{shot}}^2 \gg \sigma_{\text{det}}^2$. Since $I_R \gg I_S$, both shot noise and excess intensity noise are dominated by contribution from the reference arm. We have that detector noise is independent of the reference arm intensity, $\sigma_{\text{shot}}^2 \propto I_R$ and $\sigma_{\text{ex}}^2 \propto I_R^2$. Therefore, in order to be shot-noise limited, one can tune the reference arm power to be large enough such that detector noise is negligible but not so large that excess noise dominates [17].

To determine which noise source is dominant, we compute the threshold that the reference arm power must stay within in order to be shot-noise limited. Mathematically, shot noise is a result of the quantized nature of photo-electrons whereas excess noise depends on the light source and degree of polarization. For an SLD, we have that:

$$\sigma_{\text{shot}}^2 = q B i_{\text{ave}}$$

$$\sigma_{\text{ex}}^2 = \frac{(1 + \alpha^2)}{2\Delta\nu} B i_{\text{ave}}^2$$

where α is the degree of polarization, $i_{ave} = \epsilon I_R A q$ is the average current, $\Delta\nu$ is the effective linewidth of the light source, $B = \frac{1}{T}$ is the bandwidth of the detection, and $q = 1.6 \times 10^{-19}$ C/e- is the charge of an electron [18–20].

In units of photo-electrons, the equivalent expressions are:

$$\sigma_{shot}^2 = n_{ave}$$

$$\sigma_{ex}^2 = n_{ave}^2 \frac{(1 + \alpha^2)}{2} \frac{B}{\Delta\nu}.$$

Therefore, for shot-noise-limited detection, we need that

$$\sigma_{shot}^2 \gg \sigma_{ex}^2$$

$$n_{ave} \gg \frac{(1 + \alpha^2)}{2} n_{ave}^2 \frac{B}{\Delta\nu}$$

$$n_{ave} \ll \frac{2}{(1 + \alpha^2)} \frac{\Delta\nu}{B}.$$

For our experiments, the SLD light source (Thorlabs SLD830S-A20) had an effective linewidth of $\Delta\nu = 13$ THz (computed using a Gaussian power spectrum with center wavelength 830 nm and FWHM bandwidth of 20 nm). We filter the SLD light through linear polarizers; for this reason, we use $\alpha = 1$. The interference signal was detected using an exposure time of approximately $T = 4$ ms. The camera we used, PCOEdge5.5, had a dark current noise of 0.8 e-/pixel/second and a readout noise of 1 e- to 3 e- and is therefore negligible. Therefore, we only need to ensure that excess noise does not dominate.

$$n_{ave} \ll 13 \times 10^{12} \times 4 \times 10^{-3} = 5 \times 10^{10} \text{ photo-electrons}$$

Since the full-well-depth of the PCOedge5.5 camera is 30,000 e-, we are well below this limit.

BIBLIOGRAPHY

- [1] D. Huang, E. A. Swanson, C. P. Lin, J. S. Schuman, W. G. Stinson, W. Chang, M. R. Hee, T. Flotte, K. Gregory, C. A. Puliafito, *et al.*, “Optical coherence tomography,” *science*, vol. 254, no. 5035, pp. 1178–1181, 1991.
- [2] M. A. Choma, M. V. Sarunic, C. Yang, and J. A. Izatt, “Sensitivity advantage of swept source and fourier domain optical coherence tomography,” *Optics express*, vol. 11, no. 18, pp. 2183–2189, 2003.
- [3] Z. Yaqoob, J. Wu, and C. Yang, “Spectral domain optical coherence tomography: a better oct imaging strategy,” *Biotechniques*, vol. 39, no. 6, pp. S6–S13, 2005.
- [4] D. A. Boas, D. H. Brooks, E. L. Miller, C. A. DiMarzio, M. Kilmer, R. J. Gaudette, and Q. Zhang, “Imaging the body with diffuse optical tomography,” *IEEE signal processing magazine*, vol. 18, no. 6, pp. 57–75, 2001.
- [5] Y. Hoshi and Y. Yamada, “Overview of diffuse optical tomography and its clinical applications,” *Journal of biomedical optics*, vol. 21, no. 9, p. 091312, 2016.
- [6] E. M. Hillman, D. A. Boas, A. M. Dale, and A. K. Dunn, “Laminar optical tomography: demonstration of millimeter-scale depth-resolved imaging in turbid media,” *Optics letters*, vol. 29, no. 14, pp. 1650–1652, 2004.
- [7] L. V. Wang and H.-i. Wu, *Biomedical optics: principles and imaging*. John Wiley & Sons, 2012.
- [8] A. Wax and J. Thomas, “Measurement of smoothed wigner phase-space distributions for small-angle scattering in a turbid medium,” *JOSA A*, vol. 15, no. 7, pp. 1896–1908, 1998.
- [9] R. K. Wang, “Signal degradation by multiple scattering in optical coherence tomography of dense tissue: a monte carlo study towards optical clearing of biotissues,” *Physics in Medicine & Biology*, vol. 47, no. 13, p. 2281, 2002.
- [10] M. G. Giacomelli and A. Wax, “Imaging beyond the ballistic limit in coherence imaging using multiply scattered light,” *Optics express*, vol. 19, no. 5, pp. 4268–4279, 2011.
- [11] T. E. Matthews, M. G. Giacomelli, W. J. Brown, and A. Wax, “Fourier domain multispectral multiple scattering low coherence interferometry,” *Applied optics*, vol. 52, no. 34, pp. 8220–8228, 2013.

- [12] Y. Zhao, J. R. Maher, M. M. Ibrahim, J. S. Chien, H. Levinson, and A. Wax, "Deep imaging of absorption and scattering features by multispectral multiple scattering low coherence interferometry," *Biomedical optics express*, vol. 7, no. 10, pp. 3916–3926, 2016.
- [13] Q. Fang and D. A. Boas, "Monte carlo simulation of photon migration in 3d turbid media accelerated by graphics processing units," *Optics express*, vol. 17, no. 22, pp. 20178–20190, 2009.
- [14] J. W. Goodman, *Speckle phenomena in optics: theory and applications*. Roberts and Company Publishers, 2007.
- [15] Y. Zhao, K. K. Chu, E. T. Jelly, and A. Wax, "Origin of improved depth penetration in dual-axis optical coherence tomography: a monte carlo study," *Journal of biophotonics*, vol. 12, no. 6, p. e201800383, 2019.
- [16] C.-T. Pan, M. D. Francisco, C.-K. Yen, S.-Y. Wang, and Y.-L. Shiue, "Vein pattern locating technology for cannulation: A review of the low-cost vein finder prototypes utilizing near infrared (nir) light to improve peripheral subcutaneous vein selection for phlebotomy," *Sensors*, vol. 19, no. 16, p. 3573, 2019.
- [17] A. M. Rollins and J. A. Izatt, "Optimal interferometer designs for optical coherence tomography," *Optics letters*, vol. 24, no. 21, pp. 1484–1486, 1999.
- [18] P. Morkel, R. Laming, and D. Payne, "Noise characteristics of high-power doped-fibre superluminescent sources," *Electronics Letters*, vol. 26, no. 2, pp. 96–98, 1990.
- [19] K. Takada, "Noise in optical low-coherence reflectometry," *IEEE Journal of Quantum Electronics*, vol. 34, no. 7, pp. 1098–1108, 1998.
- [20] A. G. Podoleanu and D. A. Jackson, "Noise analysis of a combined optical coherence tomograph and a confocal scanning ophthalmoscope," *Applied Optics*, vol. 38, no. 10, pp. 2116–2127, 1999.

*Chapter 5***METHOD TO DETERMINE SYRINGE SILICONE OIL LAYER HETEROGENEITY AND INVESTIGATION OF ITS IMPACT ON PRODUCT PARTICLE COUNTS**

*This chapter is adapted from the manuscript M. Cua[†], D. Martin[†], P. Meza, G. Toracca, T. Pearson, S. Cao, and C. Yang, “Method to determine syringe layer heterogeneity and investigation of its impact on product particle counts,” *Optics Letters* 109(11):3292-3299 (2020) DOI: 10.1016/j.xphs.2020.07.012*

The previous two chapters dealt with the issue of optical scattering and described methods for imaging through or within scattering media. Here, we present the development of an optical technique that uses interferometry to evaluate the distribution of silicone oil that lines the inner surface of prefilled syringes (PFSs). The distribution of silicone oil is important as it impacts syringe functionality and may play a role in the formation of undesired particles in the drug product. Prior to this work, methods to non-destructively characterize the silicone oil distribution in syringes were limited.

In this chapter, we present a method to visualize and quantify the relative distribution of silicone oil in empty PFSs using a custom-built, multi-color, interferometric imaging system. We then applied the system in a preliminary study to investigate the impact of the silicone oil distribution on the number of particles formed in solution after filling and extrusion for two different types of syringes.

5.1 Introduction

Glass prefilled syringes (PFSs) have been increasingly adopted for parenteral drug storage and delivery of therapeutic protein formulations. In comparison to traditional vials, PFSs offer many advantages for drug delivery, such as decreased risk of contamination, improved ease of handling, and increased dosage consistency [1]. To improve the functionality of glass PFSs, the stopper and inner surface of the barrel are often coated with silicone oil which serves as a lubricant to reduce injection force, ensure smooth injection, and prevent incomplete drug dosage.

Both the amount and distribution of silicone oil can impact PFS functionality. Insufficient siliconization can lead to stalling [2, 3] whereas excessive siliconization

can lead to increased level of particles [4]. Apart from the total amount, the silicone oil distribution also plays an important role for myriad reasons. Mechanically, heterogeneous distributions can result in uneven gliding forces and incomplete drug dispensation [3]. Functionally, the silicone oil distribution may also impact the formation of both sub-visible particles (SbVP) and visible particles. Silicone oil droplets can form from oil sloughed off the coating [2, 5]. The silicone-water interfaces can serve as sites for protein adsorption, which can result in loss of product and increased protein aggregation and particle formation [2, 6, 7]. Uneven oil distributions may thereby impact particle formation by providing a larger interfacial surface area for silicone oil migration and protein interactions [8, 9]. The uneven distribution can also expose areas of glass to the protein formulations, providing yet another interface for protein adsorption and aggregation [10].

Limiting particle formation is important in the design and manufacturing of PFSs for regulatory compliance and product quality reasons. Global pharmacopoeias regulate the number of SbVPs larger than $10\mu\text{m}$ and $25\mu\text{m}$ in injectable therapeutic products [11–13]. Although currently unregulated, SbVPs in the range of $0.1\mu\text{m}$ to $10\mu\text{m}$ are of growing interest due to their potential immunogenicity [14, 15].

Currently, pharmaceutical companies fill a batch of syringes with drug products and test the particle counts of a subset as part of product release and stability programs. If the particle counts exceed regulation, a deviation is opened to systematically investigate root causes, determine product quality impact, and if required, generate corrective actions. Based on the outcome of the investigation, actions up to and potentially including batch rejection will be taken as appropriate. This is a very time- and resource-intensive approach. If a correlation between silicone oil distribution in an unfilled syringe and particle counts exists, it could be beneficial in improving quality and reducing waste. Thus, monitoring the silicone oil distribution is important, not only for mechanical functionality, but also for regulatory compliance and economic reasons. Methods to investigate the distribution of the silicone oil layer in empty, unfilled PFSs are limited. A common method for measuring oil layer thickness is white-light, thin-film interferometry [8]. Existing instruments measure the silicone oil layer thickness at discrete points and interpolate to get the overall thickness [8]. Thus, these methods require a large amount of sampling to adequately map out the oil topology. Other techniques include confocal Raman spectroscopy, 3D laser scanning microscopy, and the powder method. Confocal Raman spectroscopy determines the presence of silicone oil but not the relative evenness in the

distribution [3]. 3D laser scanning microscopy is able to measure the thickness distribution but requires destructive sample preparation [16]. The powder method allows for a rough visualization of the silicone oil layer but is destructive and requires a sufficiently thick silicone oil layer [8]. These methods are challenging to use for routine analysis of the silicone oil layer distribution due to their long time requirements, limited sensitivity, and/or destructive nature.

As an alternative to direct topological measurements, we developed a technology to non-destructively visualize and quantify the heterogeneity in the oil distribution in unfilled syringes. In contrast to the aforementioned methods, our method is not focused on measuring the oil layer thickness or presence of silicone oil, but in quantifying the relative evenness in the distribution. A multi-color interferometric imaging system was designed to visualize the relative distribution of the silicone oil layer. The heterogeneity in the distribution was quantified from the captured interferograms using two developed parameters: the number of spots and the heterogeneity percent. After verifying the system performance, we applied our system in a preliminary study to investigate the impact of the silicone oil distribution on particle formation. As opposed to existing interferometric methods, our method is capable of measuring the relative heterogeneity of the silicone oil layer non-destructively within the full field-of-view of the camera, thereby allowing for greater surface measurement in a shorter time.

5.2 Materials and Methods

Syringe Samples

This study used two types of commercially available, 2.25 mL, siliconized glass syringes (Becton, Dickinson, and Company, NJ, USA). These syringes were siliconized using two different methods: with a fixed nozzle and with a diving nozzle. In this manuscript, these syringes will be referred to as PFS-F (prefilled syringe – fixed nozzle) and PFS-D (prefilled syringe – diving nozzle). The syringes were sealed with a rubber stopper in a clean room and stored needle side up in their original containers.

Multi-Color Interferometric Imaging System

We built a multi-color, interferometric imaging system to visualize the distribution of silicone oil by modifying a commercial, inverted, reflected-light microscope (Olympus IX-81). A simplified schematic showing the main components of the optical setup is provided in Figure 5.1A. For the light source, a white LED (Prior

Scientific LDB100F) was filtered by a three-wavelength bandpass filter (Semrock FF01-457/530/628-25) that was chosen to match the quantum efficiency of the RGB channels of the camera (The Imaging Source DFK 38UX267).

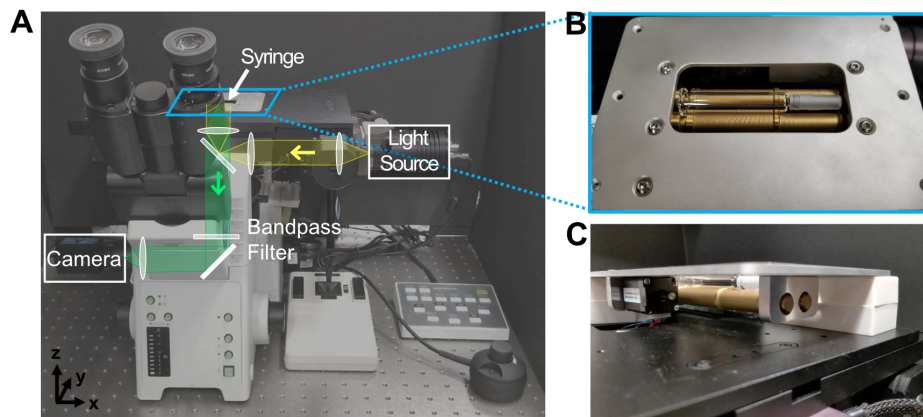


Figure 5.1: **Overview of the Multi-Color Interferometric Imaging System.** (A) A picture of the imaging system, consisting of a modified, inverted, reflected-light microscope, motorized stage, and syringe holder. A simplified 2D schematic of the optical setup has been provided, with the main components of the illumination (in yellow) and detection (in green) light paths overlaid. The coordinate system is shown on the bottom left. (B) Zoomed-in view of the customized holder for 2.25 mL syringes. The syringe rests on two rods that rotate. (C) Side view of the syringe holder.

The light source was transmitted to the syringe by a pair of lens and a beamsplitter. The back-reflected light from the syringe was collected by an objective lens (Olympus LMPLFLN 10x) and relayed to the camera. The detected light contained the interference pattern generated from light back-reflected off the oil/glass and oil/air interfaces on the inner aspect of the syringe and thus provided a visualization of the oil distribution.

The imaging system had a lateral resolution of about $1.10 \mu\text{m}$. To correct for defocus due to the curvature of the syringe, the vertical field of view was reduced; the total area imaged was about 0.6 mm by 1.4 mm (550 x 1024 pixels).

Syringe Holder

A custom holder was designed to hold and rotate the syringes (Fig. 5.1B,C). The syringe rested on two brass rods which were attached to a rectangular annulus via

vertical mounts that extended from the bottom of the plate. The system imaged the inner surface of the syringe through a 4.5 mm gap between the rods.

The rods were connected to each other at one end by a belt system. One of the rods was connected to a motor shaft (Lin Engineering, #208) on the other end. The stepper motor controlled the rotation of the two rods and the syringe.

The syringe holder was designed to sit flush inside a Prior Scientific H117 stage that controlled the lateral position of the syringe. An Olympus UX Hub controlled the vertical height of the objective lens and a separate driver (Lin Engineering R256) controlled the rotation motor. The holder was designed such that each syringe was imaged from the same starting position, which was approximately 7.5 mm from the syringe flange.

Imaging Procedure

A software program was written to control the microscope hardware and perform imaging. The user specified what fraction of the inner surface of the syringe to image. From this user-specified fraction, or percent coverage, the number of angular lines (images at different rotations) and images per line (images along the barrel) were computed to best evenly sample the inner surface of the syringe.

For imaging, the system first translated the syringe laterally, acquiring images along the barrel. After acquiring a line, the system returned to the starting position and then rotated the syringe to acquire another line. The acquired interference images were saved for further processing to quantify the heterogeneity in the oil distribution.

Prior to imaging, the relative height and tilt of the syringe barrel was first determined using an autofocus algorithm. The relative height of the syringe at a specific point was determined by acquiring a series of images with the objective lens positioned at different heights (z-axis position). For each image in the series, a focus metric based on image sharpness [17] was computed to find the most in-focus image.

The relative vertical and horizontal tilt was estimated by performing the autofocus procedure at discrete points along the barrel. To reduce the overall imaging time, three test points, evenly distributed from flange to needle end, were chosen per rotation. This autofocus procedure was repeated between successive rotations to reduce potential errors due to eccentricities in the syringe's profile. The result of the autofocus procedure was a linear estimation of the vertical and horizontal tilt in the syringe. During imaging, this linear model was used to adjust the height of the

objective lens relative to the syringe to keep the detected interference patterns in focus.

Quantification of Oil Distribution Heterogeneity

Two different metrics were developed to quantify the amount of heterogeneity in the silicone oil distribution: the number of spots and the heterogeneity percent.

Number of Spots

The first parameter, the number of spots, quantified the number of dark objects within each interferogram. Objects of low intensity were found at the center of circular fringes (Figure 5.2A). Quantifying the number of spots in an interferogram could provide an estimate for the amount of heterogeneity in the oil distribution.

Prior to detecting the spots, a calibration image was first used to remove spots that were the result of imperfections or dirt in the imaging system. Then, for every point in the image, the standard deviation within a local $74 \mu\text{m}^2$ window was computed. Since dark spots are surrounded by fringes, the standard deviation in these areas would be high. The remaining objects were thresholded by size ($\geq 15 \mu\text{m}^2$), eccentricity (< 0.96), and intensity. Figure 5.2B shows the automatically detected spots in a sample fringe image.

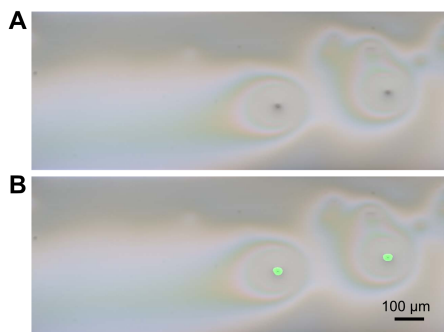


Figure 5.2: **Automatic Detection of Dark Spots in an Interferogram.** (A) An example of an interferogram with dark spots at the center of two circular fringe patterns. (B) Automatic detection of dark spots (highlighted in green) using an image processing method. Finding the number of dark spots at the center of fringes is one method for quantifying the heterogeneity in the oil distribution.

Heterogeneity Percent

The second parameter, the heterogeneity percent, quantified the amount of gray-scale intensity variation in the image. The color and intensity of an interference pattern depends on the local thickness of the interrogated area. Thus, an interferogram of an evenly distributed oil layer has smaller changes in intensity compared to an interferogram of a more heterogeneous oil distribution.

To quantify the heterogeneity, each image was first filtered using a quadrature filter [18] to reduce noise while maintaining the fringe pattern. Next, the image was divided into windows of 75 by 75 pixels, and the standard deviation of the pixel intensities within each windows was computed. The heterogeneity percent was defined as the fraction of windows (in percent) that had a standard deviation above a pre-determined threshold.

Particle Counting

The number of SbVPs in the solution was quantified using a Microflow Imaging™(MFI™) DPA4200 particle analyzer (Protein Simple). After the solution was extruded from the syringe through the needle, it was degassed in a vacuum chamber to remove air bubbles. The MFI™was then loaded with 1 mL of this extruded and degassed solution. From this 1 mL, the particles contained within 0.5-0.6 mL were counted. The MFI™View Analysis Suite software distinguished counts by radii of 1, 2, 5, 10, 25, and 50 μm . Since the MFI™results indicated that the detected particles were predominantly spherical, all measured particles were assumed to be silicone oil droplets for our analyses.

Method Development

We first investigated the repeatability and required percent coverage to accurately quantify the silicone oil distribution. To measure the repeatability, an unfilled syringe was imaged five consecutive times at 100% coverage (46 angular lines, 29 images per line), with the syringe re-loaded to a different starting rotation between acquisitions.

To determine the impact of percent coverage on the error in estimating the heterogeneity in the silicone oil distribution, 10 unfilled syringes (5 each from PFS-F and PFS-D) were imaged at 100% coverage. For each syringe, the acquired dataset was sub-sampled to simulate a smaller percent coverage. 9 unique sub-sampled datasets were used to estimate the percent error for each percent coverage. The percent error

was computed by comparing the average heterogeneity results calculated from the lower percent coverage to the results from the full coverage.

Lastly, we tested the accuracy of the algorithm used to quantify the number of spots in each image by comparing the results of the algorithm to that of manual, visual inspection. A set of 200 images, randomly sampled from the entire data set, was used for this test.

Experimental Details

To investigate the association between the particle counts and silicone oil distribution heterogeneity, we used a sample of 100, 2.25 mL syringes that came from two types of syringes: PFS-F (n=50) and PFS-D (n=50). PFS-D, a newer generation of syringes, was compared to PFS-F. Each syringe was given a unique identifier and imaged at 25% coverage (15 angular lines, 23 images per line). For each acquired image, the two heterogeneity parameters – the number of spots and the heterogeneity percent – were computed, and an average value for each parameter was determined for each syringe.

After imaging, the syringes were filled with a therapeutic protein solution that contained a proprietary antibody formulated with buffer, excipients, and surfactant (polysorbate). The number of particles in the extruded solution was quantified using the MFI™DPA4200 instrument.

5.3 Results

Method Development

To determine the system repeatability, the relative variation in the average parameter value was determined by computing the coefficient of variation for the five data sets. The heterogeneity percent had a smaller coefficient of variation (1.1%) in comparison to the number of spots (3.5%). Both quantifiers varied less than 5% relative to their respective means.

We also investigated the impact of sub-sampling the inner surface of the syringe on measuring the heterogeneity (Fig. 5.3). A larger percent coverage was associated with smaller percent error. The number of spots parameter produced the largest discrepancy from the full coverage value. For the heterogeneity percent, the error from sub-sampling remained below 5%. Overall, the average percent error was below 10% across both parameters when the inner surface was sampled at $\geq 25\%$ coverage. For this reason, the syringes used in subsequent experiments were imaged

at 25% coverage.

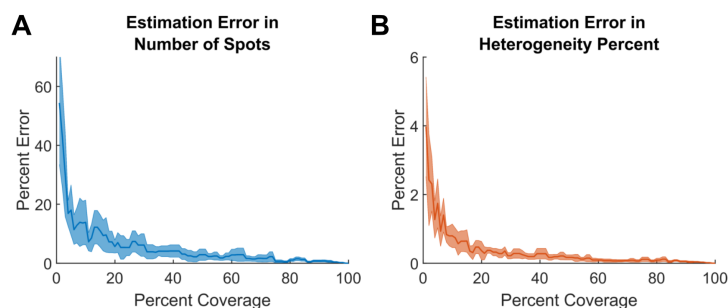


Figure 5.3: **Impact of imaging at a lower percentage coverage.** The percent error in estimating the silicone oil distribution heterogeneity when imaging at lower percent coverage is shown for (A) the number of spots and (B) the heterogeneity percent. The shaded error bar shows twice the standard error of the mean.

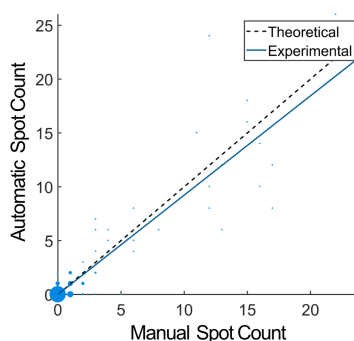


Figure 5.4: **Comparison of manual and automatic spot counting.** The plot compares the number of spots counted automatically versus manually, via visual inspection. The area of each point is proportional to the number of images satisfying that data point. The theoretical fit shows the expected fit for a one-to-one correspondence.

Lastly, we compared the automatic spot counting algorithm to manual counting for 200 randomly sampled images (Fig. 5.4) in order to determine the accuracy of the automatic algorithm. The size of the plotted point is proportional to the number of images with that particular spot count. Most of the images contained only a few spots. The dashed line (theoretical fit) shows the fit for one-to-one correspondence between the algorithm and visual inspection. Comparing the experimental fit to the theoretical fit, we see that the spot counting algorithm had a minor tendency to underestimate the manually determined number of spots. On average, the estimated number of spots deviated from the manually determined number by less than 10%.

Association between Oil Distribution and Particle Counts

Fig. 5.5 shows the average distribution in heterogeneity along the barrel of the syringe. Both parameters had local maxima at roughly 20.3 mm, 33.1 mm, and 40.4 mm from the starting position (dashed lines). There was also a sharp increase in each parameter value for locations beyond 44.0 mm, close to the needle end of the syringe.

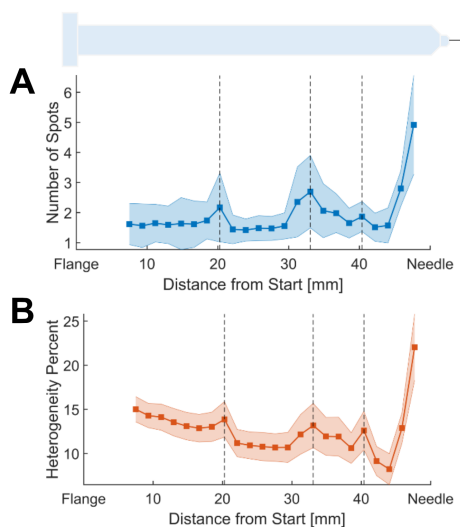


Figure 5.5: **Spatial distribution of heterogeneity.** The average distribution of heterogeneity along the syringe barrel was computed for (A) the number of spots and (B) the heterogeneity percent. The shaded areas are +/- two times the standard error of the mean. The dashed lines highlight the local maxima measured by all the parameters.

Fig. 5.6 provides a comparison of the particle counts in PFS-F and PFS-D syringes. PFS-F syringes contained a high number of particle counts. In comparison to PFS-F syringes, PFS-D syringes exhibited significantly lower particle counts, as determined using the MFI™ instrument ($p < 0.001$, independent t-test). For both types of syringes, there were orders-of-magnitude more particles of smaller diameter.

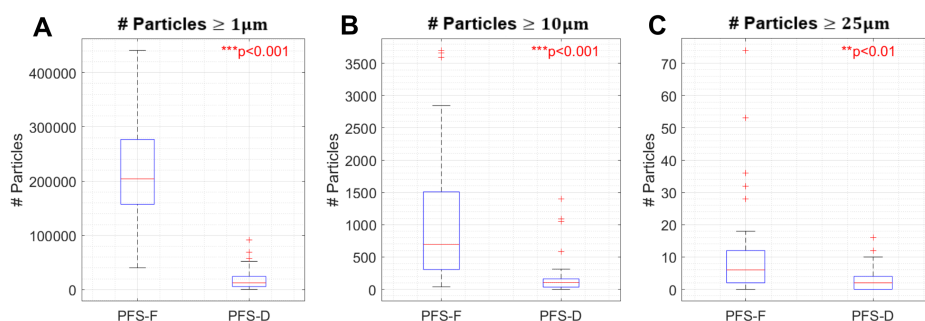


Figure 5.6: **Comparison of particle counts in PFS-F and PFS-D syringes.** PFS-D syringes contain significantly lower particle counts than PFS-F syringes, for particles (A) $\geq 1\mu\text{m}$, (B) $\geq 10\mu\text{m}$, and (C) $\geq 25\mu\text{m}$.

Fig. 5.7 provides sample interference fringes acquired from a PFS-F syringe and a PFS-D syringe. The sample interference image from the PFS-F syringe contains many fringes, indicative of a more uneven oil distribution. In comparison, the images acquired from PFS-D syringes tended to contain fewer fringes, and the fringes are of lower frequency; therefore, the oil distribution tends to be more slowly varying and even.

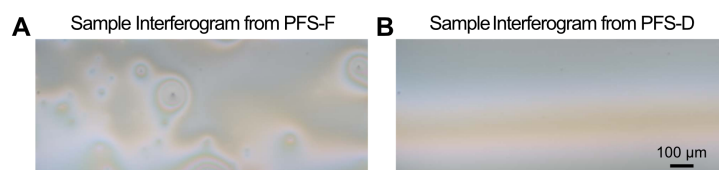


Figure 5.7: **Sample interferograms from a PFS-F and PFS-D syringe.** Representative interference images have been provided for PFS-F syringes (A) and PFS-D syringes (B), showing the difference in silicone oil distribution between the two syringe types. Images acquired from PFS-F syringes tended to contain more fringes, indicative of a more heterogeneous oil distribution. In comparison, images from PFS-D syringes tended to contain fewer fringes, and the fringes were of lower frequency, implying that the oil distribution in PFS-D syringes were more slowly varying and even.

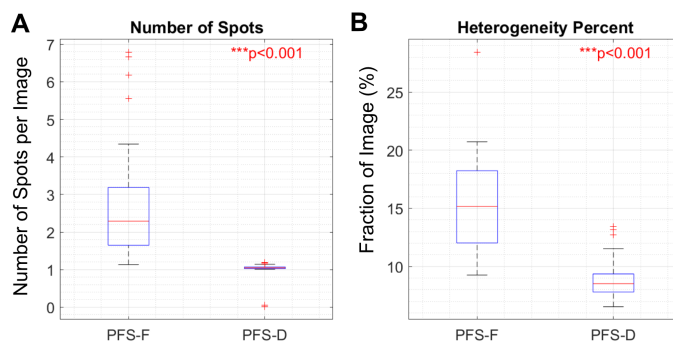


Figure 5.8: Comparison of silicone oil distribution heterogeneity in PFS-F and PFS-D syringes. The heterogeneity in the oil distribution was quantified using (A) number of spots, and (B) heterogeneity percentage. The oil distribution in PFS-D syringes were significantly more homogeneous (had lower number of spots and lower heterogeneity percentage) in comparison to PFS-F syringes.

After quantifying the heterogeneity, the interferograms from PFS-D syringes were found to have significantly less number of spots and lower heterogeneity percent (Fig. 5.8; $p < 0.001$, independent t-test). In comparison to PFS-F, PFS-D syringes exhibited both significantly lower particle counts (Fig. 5.6; $p < 0.001$) as well as significantly more homogeneous silicone oil layer distributions (Fig. 5.8; $p < 0.001$) suggesting that a correlation could exist between silicone oil layer heterogeneity and particle counts.

To further determine whether there was an association between oil distribution and particle counts, Spearman's rank correlation was computed between the average heterogeneity parameters and the particle counts (Table 5.1). The oil distribution was significantly correlated to particle counts, with stronger correlation for smaller particles. A Partial Correlation was also computed to account for possible effects due to syringe type (Table 5.1). After accounting for syringe type, Partial Correlation results show no significant association between oil distribution and particle counts.

Particle Size	Spearman Correlation r_s		Partial Correlation r_s	
	Number of Spots	Het. Percent	Number of Spots	Het. Percent
$\geq 1 \mu\text{m}$	0.74***	0.69***	0.15	0.01
$\geq 2 \mu\text{m}$	0.74***	0.70***	0.07	-0.08
$\geq 5 \mu\text{m}$	0.71***	0.70***	-0.05	-0.08
$\geq 10 \mu\text{m}$	0.54***	0.55***	-0.11	0.07
$\geq 25 \mu\text{m}$	0.34**	0.27**	-0.05	-0.10

Table 5.1: **Correlation results investigating association between cumulative particle counts and heterogeneity measures.** Bi-variate Spearman correlation between particle counts and heterogeneity measures shows significant association. Partial correlation accounting for syringe type shows no significant association. Significant correlations reported as ** $p < 0.01$, *** $p < 0.001$.

5.4 Discussion

In this paper, we developed a technology to visualize and quantify the heterogeneity in the distribution of the silicone oil lining the inner surface of unfilled syringes. A multi-color interferometric imaging system was designed and built to visualize and quantify this silicone oil distribution. After evaluating the system's repeatability and accuracy, the system was used in a preliminary investigation on the link between silicone oil distribution and particle formation. In this section, we will first discuss the system performance, followed by the results of the preliminary investigation.

Two parameters were chosen to quantify the silicone oil distribution heterogeneity from the acquired interference images: the number of spots and the heterogeneity percent. The source of the dark spots are unknown. However, since silicone oil has high wettability [5], the oil distribution heterogeneity can imply the existence of impurities in the glass or other foreign particles that disturb the surrounding oil layer.

The data suggests that the parameters chosen can quantify the level of heterogeneity in the silicone oil distribution. For both parameters, the average parameter values along the barrel exhibited local maxima at the same positions and rose sharply near the needle end. The rise in heterogeneity at the needle end is not surprising – in cases where the silicone oil distribution is not even, the needle end tends to contain less silicone oil [3, 8, 10] and would be expected to be more uneven. Although the cause for the local maxima is unknown and requires further investigation, the agreement in both the number of occurrences and location along the barrel suggests that the parameters are measuring the same phenomenon.

The heterogeneity parameters are also repeatable: the coefficient of variation was less than 5% in both cases. One possible source for the variability is defocus: defocus decreases image contrast which negatively impacts the heterogeneity parameters. Since the coefficient of variation was below 5%, this variability was not considered to be a major issue.

Of the two parameters, the number of spots had a lower repeatability and a higher percent error when imaging at a smaller percent coverage. This is likely due to the discrete nature of the parameter: a spot will not be counted if it is not contained in the acquired images, or if the image is slightly defocused. This is distinct from the heterogeneity percent, which measures a continuous value calculated from the full field of view. Another point of consideration is that most images only contained a few spots, while very few images contained many spots. Images that contain a high number of spots, although uncommon, could heavily influence the average number of spots count for a syringe. The number of spots measured can become sensitive to sampling error when imaging at a lower percent coverage.

The percent error in estimating the heterogeneity when imaging only a small fraction of the inner surface area is high. To get a more accurate measure of the heterogeneity, at least 25% of the inner surface should be sampled. Conventional point-sampling reflectometry methods, which are typically used to measure the oil height at less than 1% of the inner surface, may not have sufficient sampling to accurately extrapolate properties about the oil distribution and its impact on syringe functionality and particle formation.

Overall, the system was able to visualize and quantify the heterogeneity in the silicone oil distribution within unfilled syringes over a large fraction of the inner surface area, up to 100%. As a method to quantify the evenness of the oil distribution, our method is complementary to other methods that focus on measuring other parameters, such as the global height distribution or the presence of silicone oil. Although we applied our system to syringes coated with silicone oil, our system can be used to characterize the distribution of other coatings as well. Our method can be beneficial in studies to investigate the impact of the oil distribution heterogeneity on syringe mechanical functionality or product particle counts, and can be used complementarily to other methods due to its non-destructive nature. Apart from scientific studies, our method can also be helpful in syringe manufacturing in guiding new processes as well as screening supplies. While identifying the factors that contribute to the oil distribution heterogeneity is out of the scope of this study, one

could speculate that contributing factors may include particulates in the silicone oil used, particles from the manufacturing environment, silicone oil droplet size and distribution, and imperfections in the glass surface. Further studies may guide efforts to develop and manufacture better syringes.

We performed a preliminary investigation on the impact of the silicone oil distribution on particle formation. Our preliminary study involved two types of syringes, one of which was known to have higher particle counts. We found that PFS-D syringes contained significantly lower particle counts and homogeneous oil distributions in comparison to PFS-F syringes. However, within syringe types, no significant association was found.

There are many possible reasons for this lack of association that warrant further investigation. First, our study involved two types of syringes: PFS-F syringes and PFS-D syringes. There may be unaccounted differences between these two syringes that contributed to the variance in particle counts. For example, apart from the siliconization method, the syringe types also contain different amounts of silicone oil [19]. Factors such as silicone deposition method, silicone oil amount, and type of glass used for the barrel can impact particle formation [2, 5, 9, 20, 21].

Second, within each syringe type, the spread in the number of particles was not large. This would make finding an association difficult. A third source of variability is the extrusion: the number of particles formed during the extrusion process can vary depending on the extrusion force, the silicone oil layer thickness, and the fit between the barrel and stopper. Although the extrusion was performed using an Instron machine, tolerances in the dimensions of the syringe barrel and stopper could impact the total amount of silicone oil extruded through the needle and the force profile during extrusion, thereby adding variability in the number of particles formed.

Fourth, the measured particle counts can suffer from large sampling variability. The particle counts of larger diameter particles ($\geq 10 \mu\text{m}$) were sometimes small. For example, the average number of particles per mL in PFS-D syringes was 200 and 3 for particles $\geq 10 \mu\text{m}$ and $\geq 25 \mu\text{m}$, respectively. Considering that the sampling volume was about 0.5 mL, the measurement of these low-concentration particles would have large sampling variability [22].

Our preliminary investigation did not show a significant association between oil distribution and particle counts. Further investigations that account for the aforemen-

tioned factors are required to more conclusively determine whether an interaction exists between particle counts and oil distribution.

5.5 Conclusion

In summary, we developed a new technology for visualizing and quantifying the heterogeneity in the distribution of silicone oil lining the inner surface of unfilled syringes and applied our system in a preliminary study investigating the impact of silicone oil distribution on particle formation. Between syringe types, there was a strong association between particles counts and oil distribution. No association between particle counts and oil distribution was found within syringe types; however, there are many sources of variability that bear additional investigation. Since the percent error is large for small percent coverages, studies looking into the oil distribution heterogeneity should involve methods that can cover at least a moderate fraction of the inner surface. Our system will be beneficial in future investigations that study the impact of the distribution of silicone oil, or other lubricants, on particle formation and functionality in pre-filled syringes and can be useful as a feedback mechanism for guiding the development of better syringe manufacturing processes as well as a quality control tool to screen incoming syringe supplies.

BIBLIOGRAPHY

- [1] S. Makwana, B. Basu, Y. Makasana, and A. Dharamsi, "Prefilled syringes: An innovation in parenteral packaging," *International Journal of Pharmaceutical Investigation*, vol. 1, no. 4, pp. 200–206, 2011.
- [2] F. Felsovalyi, S. Janvier, S. Jouffray, H. Soukiassian, and P. Mangiagalli, "Silicone-Oil-Based Subvisible Particles: Their Detection, Interactions, and Regulation in Prefilled Container Closure Systems for Biopharmaceuticals," *Journal of Pharmaceutical Sciences*, vol. 101, no. 12, pp. 4569–4583, 2012.
- [3] Z. Q. Wen, A. Vance, F. Vega, X. Cao, B. Eu, and R. Schulthesis, "Distribution of silicone oil in prefilled glass syringes probed with optical and spectroscopic methods," *PDA Journal of Pharmaceutical Science and Technology*, vol. 63, no. 2, pp. 149–158, 2009.
- [4] L. S. Jones, A. Kaufmann, and C. R. Middaugh, "Silicone oil induced aggregation of proteins," *Journal of Pharmaceutical Sciences*, vol. 94, no. 4, pp. 918–927, 2005.
- [5] A. Gerhardt, B. H. Nguyen, R. Lewus, J. F. Carpenter, and T. W. Randolph, "Effect of the siliconization method on particle generation in a monoclonal antibody formulation in pre-filled syringes," *Journal of Pharmaceutical Sciences*, vol. 104, no. 5, pp. 1601–1609, 2015.
- [6] V. Corvari, L. O. Narhi, T. M. Spitznagel, N. Afonina, S. Cao, P. Cash, I. Cecchini, M. R. DeFelippis, P. Garidel, A. Herre, A. V. Koulov, T. Lubiniecki, H. C. Mahler, P. Mangiagalli, D. Nesta, B. Perez-Ramirez, A. Polozova, M. Rossi, R. Schmidt, R. Simler, S. Singh, A. Weiskopf, and K. Wuchner, "Subvisible (2-100 μm) particle analysis during biotherapeutic drug product development: Part 2, experience with the application of subvisible particle analysis," *Biologics*, vol. 43, no. 6, pp. 457–473, 2015.
- [7] E. Krayukhina, M. Yokoyama, K. K. Hayashihara, T. Maruno, M. Noda, H. Watanabe, T. Uchihashi, and S. Uchiyama, "An assessment of the ability of submicron-and micron-size silicone oil droplets in dropped prefilled syringes to invoke early-and late-stage immune responses," *Journal of Pharmaceutical Sciences*, vol. 108, no. 7, pp. 2278–2287, 2019.
- [8] V. Loosli, O. Germershaus, H. Steinberg, S. Dreher, U. Grauschopf, and S. Funke, "Methods to determine the silicone oil layer thickness in sprayed-on siliconized syringes," *PDA journal of pharmaceutical science and technology*, pp. 278–297, 2018.

- [9] S. Funke, J. Matilainen, H. Nalenz, K. Bechtold-Peters, H. C. Mahler, and W. Friess, "Silicone Migration From Baked-on Silicone Layers. Particle Characterization in Placebo and Protein Solutions," *Journal of Pharmaceutical Sciences*, vol. 105, no. 12, pp. 3520–3531, 2016.
- [10] B. Eu, A. Cairns, G. Ding, X. Cao, and Z.-Q. Wen, "Direct visualization of protein adsorption to primary containers by gold nanoparticles," *Journal of pharmaceutical sciences*, vol. 100, no. 5, pp. 1663–1670, 2011.
- [11] USP, "Particulate Matter in Injections," in *United States Pharmacopeia and National Formulary (USP 41 - NF 36)*, ch. <788>, 2018.
- [12] JP, "Foreign Insoluble Matter Test for Injections," in *The Japanese Pharmacopoeia 17th Ed.*, ch. 6.06, 2016.
- [13] EP, "Particulate contamination: sub-visible particles," in *European Pharmacopoeia*, ch. 2.9.19, 2016.
- [14] J. F. Carpenter, T. W. Randolph, W. Jiskoot, D. J. Crommelin, C. R. Middaugh, G. Winter, F. A. Ying-Xin, S. Kirshner, D. Verthelyi, S. Kozlowski, K. A. Clouse, P. G. Swann, A. M. Rosenberg, and B. Cherney, "Overlooking subvisible particles in therapeutic protein products: Gaps that may compromise product quality," *Journal of Pharmaceutical Sciences*, vol. 98, no. 4, pp. 1201–1205, 2009.
- [15] S. Bukofzer, J. Ayres, A. Chavez, M. Devera, J. Miller, D. Ross, J. Shabushnig, S. Vargo, H. Watson, and R. Watson, "Industry Perspective on the Medical Risk of Visible Particles in Injectable Drug Products," *PDA Journal of Pharmaceutical Science and Technology*, vol. 69, no. 1, pp. 123–139, 2015.
- [16] S. Funke, J. Matilainen, H. Nalenz, K. Bechtold-Peters, H.-C. Mahler, and W. Friess, "Analysis of thin baked-on silicone layers by ftir and 3d-laser scanning microscopy," *European Journal of Pharmaceutics and Biopharmaceutics*, vol. 96, pp. 304–313, 2015.
- [17] A. Santos, C. Ortiz de Solórzano, J. J. Vaquero, J. Pena, N. Malpica, and F. Del Pozo, "Evaluation of autofocus functions in molecular cytogenetic analysis," *Journal of microscopy*, vol. 188, no. 3, pp. 264–272, 1997.
- [18] J. A. Quiroga, M. Servin, and J. L. Marroquin, "Regularized phase tracking technique for demodulation of isochromatics from a single tricolour image," *Measurement Science and Technology*, vol. 13, no. 1, pp. 132–140, 2002.
- [19] J. Wright and H. Soukiassian, "Prefillable Syringe Technology - BD Neopak - Delivering the Next Generation in Glass Prefillable Syringes." <https://drug-dev.com/prefillable-syringe-technology-bd-neopak-delivering-the-next-generation-in-glass-prefillable-syringes/>, 2014. [Online; accessed 22-March-2020].

- [20] R. A. Depaz, T. Chevolleau, S. Jouffray, R. Narwal, and M. N. Dimitrova, "Cross-linked silicone coating: a novel prefilled syringe technology that reduces subvisible particles and maintains compatibility with biologics," *Journal of pharmaceutical sciences*, vol. 103, no. 5, pp. 1384–1393, 2014.
- [21] C. Wang, F. C. Cheong, D. B. Ruffner, X. Zhong, M. D. Ward, and D. G. Grier, "Holographic characterization of colloidal fractal aggregates," *Soft Matter*, vol. 12, no. 42, pp. 8774–8780, 2016.
- [22] A. Ríos Quiroz, J. Lamerz, T. Da Cunha, A. Boillon, M. Adler, C. Finkler, J. Huwyler, R. Schmidt, H. C. Mahler, and A. V. Koulov, "Factors Governing the Precision of Subvisible Particle Measurement Methods - A Case Study with a Low-Concentration Therapeutic Protein Product in a Prefilled Syringe," *Pharmaceutical Research*, vol. 33, no. 2, pp. 450–461, 2016.